AD A060423

DDC FILE COPY

(14) AFML-TR-77-134

(2) LEVEL II

(6) IMPACT BEHAVIOR OF LOW STRENGTH PROJECTILES.

Metals Behavior Branch
Metals and Ceramics Division

(10) James S. Wilbeck

DDC
RECEIVED
OCT 27 1978
B

(11) July 1978

(12) 129 p.

TECHNICAL REPORT AFML-TR-77-134

(9) Final Report, [redacted] 1 Jul [redacted]74 - 31 May 1977,

(16) 2418, 7351 (17) 03, 06

Approved for public release; distribution unlimited.

AIR FORCE MATERIALS LABORATORY
AIR FORCE WRIGHT AERONAUTICAL LABORATORIES
AIR FORCE SYSTEMS COMMAND
WRIGHT-PATTERSON AIR FORCE BASE, OHIC 45433

012 320

78 10 16 027

mt

NOTICE

When Government drawings, specifications, or other data are used for any purpose other than in connection with a definitely related Government procurement operation, the United States Government thereby incurs no responsibility nor any obligation whatsoever; and the fact that the government may have formulated, furnished, or in any other way supplied the said drawings, specifications, or other data, is not to be regarded by implication or otherwise as in any manner licensing the holder or any other person or corporation, or conveying any rights or permission to manufacture, use, or sell any patented invention that may in any way be related thereto.

This report has been reviewed by the Information Office (OI) and is releasable to the National Technical Information Service (NTIS). At NTIS, it will be available to the general public, including foreign nations.

This technical report has been reviewed and is approved for publication.

James S. Wilbeck

JAMES S. WILBECK, Capt., USAF
Project Engineer

FOR THE COMMANDER

Walter H. Reimann

WALTER H. REIMANN, Actg. Chief
Metals Behavior Branch
Metals and Ceramics Division
Air Force Materials Laboratory

"If your address has changed, if you wish to be removed from our mailing list, or if the addressee is no longer employed by your organization please notify AFML/LLN , W-PAFB, OH 45433 to help us maintain a current mailing list".

Copies of this report should not be returned unless return is required by security considerations, contractual obligations, or notice on a specific document.

AIR FORCE/56780/20 September 1978 — 300

UNCLASSIFIED

SECURITY CLASSIFICATION OF THIS PAGE (When Data Entered)

REPORT DOCUMENTATION PAGE		READ INSTRUCTIONS BEFORE COMPLETING FORM
1. REPORT NUMBER AFML-TR-77-134	2. GOVT ACCESSION NO.	3. RECIPIENT'S CATALOG NUMBER
4. TITLE (and Subtitle) IMPACT BEHAVIOR OF LOW STRENGTH PROJECTILES		5. TYPE OF REPORT & PERIOD COVERED Final Report 1 July 1974 - 31 May 1977 6. PERFORMING ORG. REPORT NUMBER
7. AUTHOR(s) James S. Wilbeck		8. CONTRACT OR GRANT NUMBER(s)
9. PERFORMING ORGANIZATION NAME AND ADDRESS Air Force Materials Laboratory Air Force Wright Aeronautical Laboratories Wright-Patterson Air Force Base, Ohio 45433		10. PROGRAM ELEMENT, PROJECT, TASK AREA & WORK UNIT NUMBERS 62102F, 2418, 241803, 24180302
11. CONTROLLING OFFICE NAME AND ADDRESS Air Force Materials Laboratory Air Force Wright Aeronautical Laboratories Wright-Patterson Air Force Base, Ohio 45433		12. REPORT DATE July 1978 13. NUMBER OF PAGES 129
14. MONITORING AGENCY NAME & ADDRESS (if different from Controlling Office)		15. SECURITY CLASS. (of this report) Unclassified 15a. DECLASSIFICATION/DOWNGRADING SCHEDULE

16. DISTRIBUTION STATEMENT (of this Report)

Approved for public release; distribution unlimited.

17. DISTRIBUTION STATEMENT (of the abstract entered in Block 20, if different from Report)

18. SUPPLEMENTARY NOTES

19. KEY WORDS (Continue on reverse side if necessary and identify by block number)

Impact, Foreign Object Damage, Soft Body Impact, Bird Impact, Fluid Impact, Hydrodynamic Theory, Fluid Jet

20. ABSTRACT (Continue on reverse side if necessary and identify by block number)

An unsteady, hydrodynamic model of the impact of a low strength projectile on a rigid or semi-rigid target has been developed. Impact tests of various materials including birds, gelatin, and RTV rubber have been conducted to validate this theory. At velocities above 100 m/s, these materials were seen to flow as a fluid upon impact. The resulting impact pressure histories were very similar to those predicted using the model. The impact process was dominated by an initial shock phase which was quickly followed by a release to a steady flow

DD FORM 1 JAN 73 1473 EDITION OF 1 NOV 65 IS OBSOLETE

UNCLASSIFIED

SECURITY CLASSIFICATION OF THIS PAGE (When Data Entered)

20. Cont'd)

condition. This model should be applicable to the impact of any material for whi h the shock pressures generated during impact are much greater than the strength of the projectile but are less than the strength of the target.

FOREWORD

This report summarizes some of the inhouse research conducted by Captain James Wilbeck, Metals Behavior Branch, Metals and Ceramics Division, Air Force Materials Laboratory. The work was conducted under Project 7351, Task 735106, "Work Unit 735106B3," Dynamic Behavior of Engine Materials." The experimental data was obtained by the University of Dayton Research Institute under Contract F33615-73-C-5027 which was monitored by Capt. Wilbeck and Dr. Alan K. Hopkins.

The research was conducted during the period July 1974 to May 1977. This report was initially submitted to the Graduate College of Texas A&M University as a dissertation in partial fulfillment of the requirements for the degree of Doctor of Philosophy in May 1977. It was subsequently submitted for publication as an AFML report in June 1977.

ACCESSION for
NTIS White Section
DDC Buff Section
UNANNOUNCED
JUSTIFICATION
BY
DISTRIBUTION/AVAILABILITY CODES
Dist. AVAIL. and/or SPECIAL
A

TABLE OF CONTENTS

SECTION		PAGE
I	INTRODUCTION	1
II	LITERATURE SURVEY	4
III	IMPACT THEORY	16
	1. Hydrodynamic Theory	16
	2. Special Considerations	34
	3. Equations of State	45
	4. Limitations of Theory	55
IV	EXPERIMENTAL TECHNIQUE	57
	1. Gun Systems	57
	2. Hopkinson Bar	59
	3. Pressure Plate	64
V	RESULTS AND DISCUSSION	67
	1. Hopkinson Bar Tests	67
	2. Pressure Plate Tests	70
VI	CONCLUSIONS	96
	REFERENCES	97
	APPENDIX A RADIAL PRESSURE DISTRIBUTION	103
	APPENDIX B GENERAL PRESSURE-DENSITY RELATIONSHIPS	105
	APPENDIX C MATERIAL PROPERTIES	112

PRECEDING PAGE BLANK

78 10 10 027

LIST OF ILLUSTRATIONS

FIGURE		PAGE
1.	One Dimensional Shock Flow. a) Shock Propagating into a Fluid at Rest, b) Flow Brought to a Rest Across the Shock, c) Standing Shock.	18
2.	Effect of Compressibility on the Hugoniot Pressure for Water. (1 MN/m^2 = 10 Bars)	20
3.	Shock and Release Waves in Fluid Impact.	21
4.	Comparison of the Shock Velocity, u_s, and the Sound Speed in the Shocked Region, c_r.	23
5.	Variation of the Duration of the Hugoniot Pressure with Impact Velocity for a Cylindrical Projectile of Water.	23
6.	Variation of Critical Length with Impact Velocity for Water.	25
7.	Radial Distribution of Steady Flow Pressure.	29
8.	Compressibility Effects in Steady Flow. a) Stagnation Pressure, b) Pressure Distribution.	31
9.	Standing Shock in Steady Flow.	32
10.	The Impact of a Yawed Projectile.	35
11.	The Impact of a Curved Surface on a Flat Target.	37
12.	Oblique Impact of a Cylinder on a Rigid Plate.	37
13.	Variation of Hugoniot Shock Pressure with Angle of Impact for Water. (1 MN/m^2 = 10 Bars)	39
14.	The Steady Flow Phase of an Oblique Impact.	39
15.	Steady Flow Pressure Distribution for a 30° Impact of a Plane Jet of Water (Taylor, Reference 59).	40
16.	Relationships Between the Hugoniot Shock Pressure and Particle Velocity for Water with Various Porosities. (1 MN/m^2 = 10 Bars)	42
17.	Relationships Between the Stagnation Pressure and the Impact Velocity in Steady Flow for Water with Various Porosities. (1 MN/m^2 = 10 Bars)	42

LIST OF ILLUSTRATIONS (CONTINUED)

FIGURE		PAGE
18.	The Variation in Steady Flow Pressure Distribution for Water Due to the Addition of Porosity.	43
19.	Impact on an Elastic Target During the Early Shock Phase.	43
20.	Hugoniot Pressure-Volume Relationships for Water with Various Porosities. (1 MN/m^2 = 10 Bars)	52
21.	Relationships between the Shock Velocity and the Particle Velocity for Water with Various Porosities.	53
22.	Isentropic Pressure-Volume Relationships for Water with Various Porosities. (MN/m^2 = 10 Bars)	54
23.	Overall View of the Gun Range Facility Used for Bird Testing.	58
24.	Sabot Stopper for Use with Powder Gun.	59
25.	Cylindrical Projectile with Balsa Wood Sabot.	60
26.	Sabot Stripper for Use with Compressed Air Gun.	60
27.	Schematic of Hopkinson Pressure Bar.	62
28.	Overall View of the Hopkinson Bar Apparatus.	63
29.	Pressure Plate Apparatus.	65
30.	Typical Hopkinson Bar Data, Normal Impact.	68
31.	Relationship Between the Normal Component of Momentum and the Impulse Imparted to the Target for the Impact of Porous RTV.	69
32.	Relationship Between the Normal Component of Momentum and the Impulse Imparted to the Target for the Impact of Porous Gelatin.	69
33.	Relationship Between the Normal Component of Momentum and the Impulse Imparted to the Target for the Impact of Birds.	70
34.	Typical Pressure Plate Data, Normal Impact.	72
34.	Typical Pressure Plate Data, Normal Impact (Continued)	73

LIST OF ILLUSTRATIONS (CONTINUED)

FIGURE		PAGE
35.	Typical Pressure Data at Various Impact Velocities for Porous RTV, Normal Impact.	76
36.	Typical Pressure Data at Various Impact Velocities for Porous Gelatin, Normal Impact.	77
37.	Typical Pressure Data at Various Impact Velocities for Birds, Normal Impact.	78
38.	Typical Distribution of Pressure Plate Data for the Impact of Porous RTV, Normal Impact.	80
39.	Typical Distribution of Pressure Plate Data for the Impact of Porous RTV, Oblique Impact (α = 45°).	81
40.	Hugoniot Shock Pressures Measured During Normal Impact of Porous RTV. (1 MN/m^2 = 10 Bars, 10^3 kg/m^3 = .036 lb/in^3).	83
41.	Hugoniot Shock Pressures Measured During Normal Impact of Porous Gelatin. (1 MN/m^2 = 10 Bars, 10^3 kg/m^3 = .036 lb/in^3).	84
42.	Hugoniot Shock Pressures Measured During Normal Impact of Birds. (1 MN/m^2 = 10 Bars, 10^3 kg/m^3 = .036 lb/in^3).	85
43.	Steady Flow Pressures Measured at the Center of Impact During Normal Impact of Porous RTV. (1 MN/m^2 = 10 Bars, 10^3 kg/m^3 = .036 lb/in^3).	87
44.	Steady Flow Pressures Measured at the Center of Impact During Normal Impact of Porous Gelatin. (1 MN/m^2 = 10 Bars, 10^3 kg/m^3 = .036 lb/in^3).	88
45.	Steady Flow Pressures Measured at the Center of Impact During Normal Impact of Birds. (1 MN/m^2 = 10 Bars, 10^3 kg/m^3 = .036 lb/in^3).	89
46.	Radial Distribution of Steady Flow Pressures for the Normal Impact of Porous RTV.	90
47.	Radial Distribution of Steady Flow Pressures for the Normal Impact of Pure Gelatin.	91
48.	Radial Distribution of Steady Flow Pressures for the Normal Impact of Porous Gelatin.	91

LIST OF ILLUSTRATIONS (CONCLUDED)

FIGURE		PAGE
49	Radial Distribution of Steady Flow Pressures for the Normal Impact of Birds.	92
50	Hugoniot Shock Pressures Measured at Various Points Along the Target Surface During the Oblique Impact (α = 45°) of Porous RTV. (1 MN/m^2 = 10 Bars).	94
51	Hugoniot Shock Pressures Measured at the Initial Point of Impact During the Oblique Impact (α = 25°) of Porous RTV. (1 MN/m^2 = 10 Bars).	94
52	Steady Flow Pressures Measured at or Near Stagnation Point for Normal and Oblique (α = 45°) Impact of Porous RTV. (1 MN/m^2 = 10 Bars)	95
53	Shock Hugoniot for Air.	109
54	Experimental Values of Shock Velocity vs. Particle Velocity.	109

LIST OF SYMBOLS

A, B	Material constants in Cogolev's pressure-density relationship
A	Cross-sectional area of projectile
a	Initial radius of projectile and circular jet
b	Initial width of planar jet
c	Wave speed
c_ℓ	Longitudinal, elastic wave speed
c_o	Isentropic wave speed
c_r	Velocity of initial release wave (speed of sound in the shocked region)
D	Initial diameter of projectile
E	Modulus of elasticity
F	Force
fm	Mass fraction
fv	Volume fraction
I	Impulse
K	Bernoulli's constant
k	Constant in linear Hugoniot equation
L	Initial length of projectile
L_c	Critical length of projectile, defined by Equation 12
M	Initial mass of projectile
P	Pressure
P_H	Hugoniot shock pressure, defined by Equation 4
P_o	Free-stream pressure, atmospheric pressure
P_s	Steady Flow pressure at the stagnation point
q	Defined by Equation 49

LIST OF SYMBOLS (CONTINUED)

R	Radius of jet at which steady flow approaches atmospheric pressure
r	Radial distance from center of impact
T	Duration of an elastic impact
t	Time
t_B	Duration of the full shock pressure at the center of impact
t_c	Time needed for release wave to reach center of shock wave
t_D	Duration of impact for a fluid projectile
u	Velocity of fluid
u_o	Impact velocity
u_p	Particle velocity
u_s	Velocity of shock propagating into fluid at rest
x_r	Distance traveled by release wave
x_s	Distance traveled by shock wave
y	Distance from center of impact
z	Amount of porosity, volume fraction of air
α	Angle of impact obliquity (relative to target surface)
β	Material compressibility
γ	Ratio of specific heats of air
ε	Strain
ζ_1, ζ_2	Constants in Equations 24 and 25
θ	Empirical constant, Engel (Reference 41)
ρ	Density
ρ_f	Density of pure (nonporous) material
ρ_z	Average density of porous material
ϕ	Angle of projectile yaw
ϕ_{cr}	Critical angle of projectile yaw

SUBSCRIPTS

B	Center point of impact
c, cr	Critical values
H	Hugoniot
m	Soft body material
n	Air
p	Particle
p	Projectile
r	Release wave
s	Shock
t	Target
0	Initial (free-stream, atmospheric) conditions
1	Region in front of shock (unshocked region) in projectile
2	Region in rear of shock (shocked region) in projectile
3	Region in rear of shock (shocked region) in target
4	Region in front of shock (unshocked region) in target

LIST OF UNITS

Mass	g (gram)	= 0.0022046 lb_{lil} (pounds-mass)
	kg (kilogram)	= 10^3 g
Length	m (meter)	= 3.2808 ft (feet)
		= 39.37 in (inches)
	cm (centimeter)	= 0.01 m
		= 2.54 in
Time	s (second)	
Force	N (Newton)	= 0.2248 lb_f (pounds-force)
	MN (Meganewton)	= 10^6 N
Density	kg/m^3	= 0.0624 $^{lb_{m/ft^3}}$
		= 3.613×10^{-5} $^{lb_{m/in^3}}$
Pressure	MN/m^2	= 10 Bars
		= 145.04 $^{lb_{f/in^2}}$

SECTION I

INTRODUCTION

One of the major hazards to flight safety today is the inflight impact of birds. Aircraft windshields and engine blading are especially vulnerable to damage. Because of the importance of this problem, both NASA and the Air Force have extensive programs aimed at improving the impact tolerance of these critical components by developing better materials and better structural designs. However, this work is currently being hindered by a lack of understanding of the actual impact event. Fundamental research is needed to define both the loads generated during impact and the response of various structures to these loads.

Work is currently being conducted in the Air Force Materials Laboratory to define bird impact loads. This is a very complicated problem since the loads are actually coupled to the response of the structure. In order to simplify this, researchers have decided to decouple the loads from the target response. This is accomplished by studying the impact of birds against a rigid surface. The actual coupling mechanisms will be studies in a later program.

Another program being conducted in the laboratory in parallel with the bird loading program concerns the development of a "bird substitute" material. This synthetic bird would replace real birds in actual impact tests of aircraft components. Several materials are presently being considered, including gelatin and RTV (room temperature vulcanized) rubber.

In order to fulfill the requirements of both programs, it is obvious that a complete understanding of the fundamental principles of the impact process is required. It seems reasonable to expect that the basic mechanisms of impact of gelatin or RTV rubber should be similar to those of bird impact. This is based on the belief that during impact each of these materials tends to behave as a fluid. This is true for most materials at sufficiently high velocities. The requirements for a material to "flow" is that the stresses generated during impact substantially

exceed the strength of the material. For many projectile materials such as aluminum or steel, the stresses required to cause the material to fail are sufficient to cause local failure in the target. For example, the result of a hypervelocity impact is a crater.

However, there would seem to be a large group of materials, often considered solids, whose strength are very low relative to the strength of many target materials. For the purposes of this study, this group of materials will be referred to as soft body materials. Soft body impact will be defined as impact in which the stresses generated substantially exceed the strength of the projectile but are well below the strength of the target material. This implies that soft body projectiles will flow upon impact while the target may see little or no plastic deformation. Examples of soft body impact are birds and tire fragments striking engine blading, hail striking aircraft windshields, rain drops falling on a leaf, lead bullets striking a steel plate, or even bugs hitting an automobile windshield.

With this in mind it was felt that a general survey of the state-of-the-art in soft body impact would aid greatly in an understanding of the basic mechanisms of bird impact as well as the impact of various bird substitute materials. However, as seen in the Literature Survey of this report, the results of the literature search were limited. With the exception of water droplet and water jet impacts, there appears to have been no concerted effort to study the basic processes involved in soft body impact.

For the past 20 years, researchers have studied the impact of water droplets on a solid surface in order to develop an understanding of the mechanisms involved in the erosion of steam turbine blades and the erosion of aircraft and missile structures in rain. Much progress has been made in this area, although there is still controversy over the exact amplitude and distribution of loads, as well as the response of both the liquid droplet and the impacted surface to these loads.

Based on the insights gained from the literature search, it appears possible to directly apply much of the knowledge gained from fluid impact studies to the more general area of soft body impact. With this in mind, the author decided to undertake the present research program. The purpose of this research was to understand the basic processes involved in soft body impact. Both theoretical and experimental studies have been conducted on the impact of various soft body materials, including bird, gelatin, and RTV rubber.

A study of this magnitude should be of great benefit since the results could be used in many areas. As discussed above, the most important application to the Air Force would be in aiding in the understanding of bird impact as well as in the development of a bird substitute material. However, there are many other practical applications. For example, knowledge from this program would aid in the study of hail damage, rain erosion, and damage due to debris impact during a hurricane or tornado.

SECTION II

LITERATURE SURVEY

The impact of low strength materials has only been studied extensively in the last few years. Thus, there has been very little research in the area of soft body impact and almost none concentrated on the actual mechanisms involved in the impact process. Early researchers such as Hodgkinson (Reference 1), Tait (Reference 2), Vincent (Reference 3), and Raman (Reference 4) studied the coefficient of restitution (ratio of the rebound velocity to the initial velocity) of various soft objects. They found that the coefficient of restitution decreased with increasing velocity, demonstrating that the percentage of kinetic energy dissipated during impact increased with increasing velocity. Very little work has been done in this area except for recent studies of birds and bird substitute materials.

In the 1960's, several English engine people, including Allcock and Collin (Reference 5), studied the deflection of beams due to the impact of various soft objects including birds. Based on a comparison of the results, they determined that gelatin projectiles and birds produced comparable loads during impact. Tudor (Reference 6), studying the impact of gelatin projectiles on a cantilevered beam, developed a functional relationship between the beam deflection and the initial momentum of the projectile. In America work was carried out by Tsai, et al. (Reference 7) who found a similar relationship for the impact of RTV rubber balls. The only theoretical study of bird loading was performed by MacCauley (Reference 8) and Mitchell (Reference 9) in Canada. The work of both men were only crude approximations of the real impact case. MacCauley assumed the bird to behave as a perfect fluid and Mitchell assumed the bird to behave as a semi-rigid projectile. With other simplifying assumptions, both men derived expressions for the pressures generated during impact. No experimental work was performed to check their results.

Since so little has been done in the specific area of soft body impact, it was felt that a survey of the general area of impact might be of benefit. Specific interest was paid to studies concentrating on the response of the projectile to the impact, as opposed to the response of the target. It was found that numerous studies of the mechanics of the impact event and the related impact strength of materials have been conducted over a large range of impact velocities. Much of this work is summarized in textbooks by Goldsmith (Reference 10), Kolsky (Reference 11), and Johnson (Reference 12).

For the impact of solids, the mechanisms dominating the impact process vary with impact velocity. Realizing this, several individuals have attempted to divide the field of impact of solids into various physical regimes. Hopkins and Kolsky (Reference 13) defined five regimes; (a) elastic impact, (b) plastic impact, (c) hydrodynamic impact, (d) impact at sonic velocities, and (e) explosive impact. In elastic impact, the stresses generated do not exceed the yield strength of the material. Thus, the nature and duration of the impact only depend on the elastic moduli and the elastic wave velocities of the material. With increased velocity, the stresses generated cause plastic deformation. The material strength is still a dominating factor. As velocities increase still further, the stresses generated by deceleration of the projectile greatly exceed the yield stress. In this hydrodynamic regime, the projectile and target can be treated as fluids, and it is the material density which dominates instead of strength. In each of these regimes, stress waves propagate into the material, thus dissipating energy throughout the projectile and target. As the velocity of impact approaches or exceeds the wave velocity, more energy must be dissipated in the local region of impact. Wave motion plays an increasingly important role in determining the local stress distribution. Shock waves are also generated. As the velocity continues to increase, all of the energy is deposited in the local area. The heat produced is concentrated in a very small region, and is thus sufficient to melt and eventually to vaporize the material. This process is analogous to a small explosion taking place on the target surface.

Although these regimes have been defined for the impact of high strength projectiles, there is no reason to believe that these same regimes would not be applicable to the impact of low strength materials. Barber (Reference 14) found that cylindrical projectiles of RTV rubber and gelatin bounced at low velocities and "flowed" at high velocities. Similar results were also found for real birds. Thus, a further look into these various regimes should lead to a better understanding of soft body impact.

Johnson (Reference 12) described initial studies of elastic impact which applied elementary, one-dimensional, elastic wave theory to the impact of cylinders. Using this simple theory to study the problem of a cylinder impacting a rigid plate, an interfacial pressure $P = \rho c_\ell u_0$ and a duration $T = 2L/u_0$ can be derived, where c_ℓ is the longitudinal, elastic wave speed in the projectile. However, this simple theory neglects the effects of transverse strain and inertia as well as all dissipative forces in the projectile material.

Theories for elastic impact which take into account the effects of radial inertia were first proposed by Pochhamer (Reference 15) and Chree (Reference 16) independently. Later, theories were proposed by Love (Reference 17) and Rayleigh (Reference 18) and more recently by Redwood (Reference 19). Using Love's theory, Conway and Jakubowski (Reference 20) analyzed the coaxial impact of nearly perfect, square-ended, finite length bars. Their results showed a slight change in pulse shape due to the transverse effects.

Donnell (Reference 21) in 1930 was apparently the first to investigate longitudinal plastic wave propagation. However, major contributions to the theory of plastic wave propagation were not made known until after World War II when Taylor (Reference 22), Rakhmatulin (Reference 23), and Karman and Duwez (Reference 24) published their theories which had been developed independently during the war. In a later paper, Taylor (Reference 25), in an attempt to develop a simple method for determining the dynamic yield stress of materials, considered the propagation of both

elastic and plastic waves during impact of a cylinder on a rigid wall. His simple, theoretical model led at least to qualitative, if not quantitative, understanding of projectile mushrooming upon impact. Experiments by Whiffen (Reference 26) showed that Taylor's method was inaccurate except over a limited range of velocities. Hawkyard (Reference 27) examined the consequences of establishing an energy balance across the discontinuity at the plastic wavefront. His predictions of the final shape of the mushroomed projectile corresponded much more nearly to the shapes found experimentally by Whiffen than did the predictions of Taylor.

Although the theories of Taylor and Hawkyard aided in understanding the mechanisms of deformation during impact, they were too idealized to give good quantitative results. Both effectively considered the projectile to be a rigid, perfectly plastic material. In an attempt to overcome this limitation, Barenblatt and Ishlinskii (Reference 28) considered the impact of a linear, viscoplastic rod on a rigid wall. Ting (Reference 29) extended their work to study the impact of a nonlinear, viscoplastic projectile and contrasted his results with those of Barenblatt and Ishlinskii. All of this work considered one-dimensional wave propagation.

When the stresses generated during impact greatly exceed the yield stress of the material, the problem can be approached hydrodynamically. In the hydrodynamic approach used to study high velocity impacts, the material strength and viscosity are neglected and a simple pressure-density-energy equation of state is used to describe the material. For most materials this approach is applicable over a wide stress range.

Hopkinson (Reference 30), in studying the impact of a lead bullet on a steel plate, found experimentally that the stress in the target was approximately that to be expected from a fluid jet whose density was the same as for lead. Birchoff, et al. (Reference 31) in their study of explosives with lined cavities, may have been the first to incorporate into a mathematical theory the idea that a high strength material such as steel could be treated as though it were a perfect fluid when subjected to very high stress levels.

Thus, it is seen that even high-strength materials "flow" when subjected to very high pressures. The major drawback to this area of research is that the stresses generated at the projectile-target interface are so great that the target material also behaves hydrodynamically, resulting in large deformations (craters) in the target. Thus, it is not possible to uncouple the response of the projectile from that of the target. A review of the literature, as performed by Chakrapani and Rand (Reference 32), for example, showed that most of the research in this regime is concerned with predicting or measuring crater shape and depth. Therefore, it was decided that further study of this regime or the higher velocity regimes (sonic and explosive regimes) would be fruitless.

A much more promising area of research appears to be the study of the impact of fluids, in which the fluid projectile is always assumed to behave hydrodynamically. An extensive amount of theoretical and experimental work has been conducted on the impact of fluids on solid targets, in which the target is assumed to have little or no plastic deformation.

The majority of work in this area has been focused on the impact of water jets and water droplets, both in the study of rain and steam erosion as well as water jet cutting. In these investigations, there are several features of the impact process of greatest importance. Heymann (Reference 33) stated that these were: (a) the initial impact pressure, (b) the area over which the pressure acts, (c) the velocity of the lateral outflow of liquid after impact, and (d) the approximate decay time of high impact forces.

Some of the early work was conducted by Cook (Reference 34) in 1928, in which he compared the impact of a column of water to the waterhammer problem. He stated that in both cases, a moving column of water is suddenly arrested by a fixed surface, thereby causing an instantaneous pressure in the front layer of the column given by the expression $P = u_0 \sqrt{\rho K}$, where u_0 is the impact velocity, ρ is the initial density

of the water, and β is its compressibility. Noting the magnitude of this initial "waterhammer" pressure, he stated that "the pressure generated on an element of surface at its first encounter with water moving at a finite velocity is different from that produced by the steady impact of a moving stream of water at the same velocity". Heymann (Reference 35) phrased it differently, noting that in this type of impact, compressibility effects rather than flow phenomena initially predominate in the liquid. Thus, Cook and Heymann identified the two basic regimes of water jet impact, the initial shock regime and the late-time steady flow regime.

These two regimes were later identified by Bowden and Brunton (Reference 36) in their more detailed description of the impact of a cylinder against a rigid plate. In their paper, they stated that upon impact of an ideal, flat-ended cylinder on a rigid plate, stress waves propagate into the liquid and the pressure at the interface is the waterhammer pressure given by Cook (Reference 34), $P = \rho c_o u_o$, described in terms of the wave speed, c_o, instead of the compressibility, β. According to their description, as release waves propagate inward to the center of the cylinder, liquid is turned outward and flows radially with the same velocity u_o and the pressure at the interface is released and decays to the steady flow pressure. The pressure reduces to zero when all of the liquid has been turned. The duration of the high pressure was determined by the time taken for the release waves from the sides of the liquid cylinder, traveling at velocity c_o, to reach the center of the cylinder.

For the impact of a sphere on a rigid plate, Bowden and Field (Reference 37) described the event to be somewhat the same. Upon initial impact, the pressure at the interface again reaches a maximum given by the waterhammer equation. Release waves propagate inward sooner than for a cylinder of equal radius so that the duration of the peak pressure is less. They also stated that the waterhammer equation was only correct for low velocity impacts. For high values of impact velocity, the pressures are such that c_o is more correctly replaced by the shockwave velocity, u_s. Thus, they stated that the initial pressure generated upon impact of a cylinder or sphere is given by the relationship

$= \rho u_s u_o$. (This pressure will be referred to as the Hugoniot pressure, since it can be derived from the Hugoniot relationships across a shock.)

Although these two models of cylinder and sphere impact are generally accepted, there is much disagreement in the literature over certain features of the impact event. Most of this disagreement centers around the peak pressures generated initially during impact and the initial radial velocity of the released liquid.

It is generally agreed that Bowden and Field (Reference 37) were correct in stating that the instantaneous pressure generated during impact of a cylinder is the Hugoniot pressure. However, great difficulty has arisen in verifying this experimentally due to the inability to generate a flat-ended cylinder of water which can be impacted on a rigid surface. Bowden and Brunton (Reference 36) described a technique for accelerating a jet of water against a plate. However, these jets suffer from an inherently rounded front surface. Both Brunton (Reference 38) and Kinslow, et al. (Reference 39) were unable to obtain instantaneous peak pressures upon impact, probably a result of the rounded front. Thus, Kinslow recorded a peak pressure of only half that predicted. Field, et al. (Reference 40), also recorded peak pressures less than the Hugoniot pressure. Thus, work continues to develop better methods of testing for cylindrical impact.

Unlike the case of cylinder impacts, there is much less agreement concerning the magnitude and distribution of the initial pressure in spherical droplet impacts. Engel (Reference 41), an early pioneer in the field of erosion, stated that the average pressure in the region of the droplet which had been traversed by the shock could be expressed by $P = \frac{\Theta}{2} \rho c_o u_o$ where Θ, a constant, approaches unity for high velocity impact and the 1/2 is a consequence of the spherical shape of the droplet. However, she made no attempt to specify instantaneous distribution of pressure. Jenkins and Booker (Reference 42) agreed with Bowden and Field (Reference 37) that the maximum impact pressure for a curved surface is the Hugoniot pressure, and that this pressure is uniform over the liquid-solid interface until lateral jetting begins. In contrast to

this, Skalak and Feit (Reference 43) concluded that the "average" pressure over the liquid-solid interface was the Hugoniot pressure but also concluded that the pressure was not uniform, with maximum pressure (greater than $\rho u_s u_o$) near the edge of contact. Heymann (Reference 44) developed a theory based on the assumption that oblique shocks exist at the droplet edge and used this theory to predict that the pressure increases during early impact. This increased pressure exists at the droplet edge and continues to increase until lateral jetting starts. Pressures exceeding twice the Hugoniot pressure were predicted for an impact of Mach = 0.3.

Even greater disagreement resulted from contradicting experiments. As stated earlier, the jet launching technique used by Brunton (Reference 38) produced a cylinder with a rounded impact face. Thus, this jet was used by several researchers to simulate droplet impact. However, Brunton's experiment permitted the determination of average pressure only, instead of the actual distribution. Using this same technique, Kinslow, et al. (Reference 39), found the maximum pressure, about half the predicted Hugoniot pressure, to occur at the center of the impact. Johnson and Vickers (Reference 45) found approximately the same pressure at the center but, contrary to the work of Kinslow, et al., measured maximum pressures at the edge greater than the Hugoniot pressure. Using a two-dimensional droplet impact test, Rochester and Brunton (Reference 46) verified the work of Johnson and Vickers. Using high speed "shadowgraph" photography which allowed them to observe the stress waves generated in the droplet during impact, Rochester and Brunton observed a region of high pressure located at the edge of drop prior to lateral jetting. Field, et al. (Reference 40), used an experimental technique of launching a target projectile at a suspended droplet. Using a similar high speed photographic system to that of Rochester and Brunton, they also observed a region of high pressures near the edge of the droplet.

Not only is there disagreement in the literature over the amplitude and distribution of peak pressures generated during initial stages of impact, but there is also disagreement over the lateral flow velocities

resulting during these initial stages. Using the various experimental techniques, Engel (Reference 41), Jenkins and Booker (Reference 42), Fyall (Reference 47), Camus (Reference 48), and Rochester and Brunton (Reference 46) observed radial velocities from three to seven times the initial impact velocity of the jet or droplet. Bowden and Brunton (Reference 36) postulated that the high radial velocity resulted from jetting action of the water between the confines of the drop and the impacted surface. The results of Rochester and Brunton (Reference 46) correlated well with this theory. Contrary to this, Jenkins and Booker (Reference 42) found that their results compared favorably with the theory that the radial wash originates as steady, incompressible Bernoulli flow, where the maximum stagnation pressure is the initial peak impact pressure. The experimental work of Fyall (Reference 49) agreed with this theory. Even studies of ice impact by McNaughton, et al. (Reference 50) showed this theory to accurately predict initial flow of the ice particles upon impact.

Besides development and refinement of experimental techniques, a large effort has been applied to the use of numerical techniques to develop a better understanding of the impact event. Huang, et al. (Reference 51) spent a considerable amount of time in the study of cylindrical and spherical impact at subsonic velocities. For both of these cases, they found the maximum pressure to occur at the center of impact and to have a magnitude less than the Hugoniot pressure. However, these results are in doubt since the numerical technique was unable to properly handle the strong shocks generated. The apparent introduction of artificial viscosity probably prevented the program from responding rapidly enough to measure the actual peak pressures. Also, the numerical solution predicted precursor waves upon impact which propagated at velocities much greater than the shock velocity. However, there is no apparent physical reason for the existence of these waves.

Glenn (Reference 52) did similar studies in order to point up some of the discrepancies of the work by Huang, et al., and to extend the scope to include initially supersonic impact. All of his work concentrated on the impact of a flat cylinder on a rigid plate. For both subsonic and

supersonic impact, the peak pressure at the surface was the Hugoniot pressure, thereby throwing doubt on the work by Huang, et al. Glenn also found the maximum radial velocities to be greater than the initial impact velocity. Thus, Glenn's results compared well with experimental results. Numerical studies by Lesser and Field (Reference 53) and Prichett and Riney (Reference 54) also predicted the initial peak pressure at the center of a cylinder to be the Hugoniot pressure.

As stated earlier, once radial release waves have propagated into the center of the cylinder (or sphere) the pressure begins to decrease. After several wave reflections, the flow of a cylinder of fluid will approach a steady state condition. At the center, the pressure will be equal to the stagnation pressure of a jet. From Bernoulli's Equation, the stagnation pressure is seen to be $P = 1/2\rho u_o^2$ for an incompressible fluid. For a low velocity impact, this pressure is an order of magnitude less than the maximum shock pressure occurring initially at the center.

The major area of study in the steady flow regime is the distribution of pressure and velocity over the target surface. The pressure and velocity are related by Bernoulli's Equation. Thus, knowledge of one implies knowledge of the other. However, it is not possible to calculate the distribution of pressure (or velocity) in the impact region for an axisymmetric jet. An exact solution can be obtained for a two-dimensional jet. Milne-Thompson (Reference 55) derived the following expression for the potential flow velocity distribution along the surface of a plane jet impinging on a flat, rigid surface: $y/b = 2/\pi\ [\arctan(u/u_o) + \operatorname{arctanh}(u/u_o)]$ where y is the distance from the center along the surface, b is the initial width of the jet, u is the velocity along the surface, and u_o is the initial impact velocity. This solution assumes a free-streamline jet, thereby implying that at large distances from the center of impact, $u = u_o$. This expression is substituted into Bernoulli's Equation of the form $P - P_o = 1/2\ \rho u_o^2 [1 - (u/u_o)^2]$. Using elementary momentum considerations, Banks and

Chandrasekhara (Reference 56) developed a normal curve approximation to the exact pressure distribution of the form $P - P_o = 1/2\ \rho u_o^2 \exp\ [\frac{\pi}{4}\ (\frac{y}{b})]$. This distribution closely resembles that of Milne-Thompson. Using a similar approach, Banks and Chandrasekhara developed an error curve approximation for an axisymmetric jet impact of the form $P - P_o = 1/2\ \rho u_o^2 \exp\ [\ -\ (\frac{r}{a})2]$ where r is the radial distance from the center and a is the initial radius of the jet. This expression was a fair approximation to the data obtained by Gibson (Reference 57).

Leach and Walker (Reference 58) found that their experimental data was fit well by a polynomial expression of the form $P - P_o = 1/2\ \rho u_o^2\ [1-3(\frac{r}{R})2 + 2(\frac{r}{R})^3]$ where R was the value of r where $P \simeq P_o$. They found from momentum considerations that $R/a \simeq 2.58$. From this it was concluded that the region where the pressure is significantly greater than the ambient pressure is confined to about 2.6 jet radii.

Taylor (Reference 59), studying oblique impact, stated that the total downward force on the target plane decreases as the angle of incidence decreases. However, the maximum (stagnation) pressure is the same for all angles of impact, namely $1/2\ \rho u_o^2$, although the area over which this maximum pressure acts is much reduced as the angle of incidence becomes small.

Based on the above information, several points are clear. There is general agreement about the pressures generated during the impact of a cylinder of water on a rigid plate. The pressure at the center is initially $\rho u_s u_o$, the Hugoniot pressure, and remains at the level until lateral release waves permit radial flow to begin. After a sufficient time, steady flow is set up with the pressure at the center given by Bernoulli's Equation.

There is less agreement about the impact of a sphere (or droplet) of water. Physically, one expects the initial pressure at the center to be the same as for a cylinder, $\rho u_s u_o$, and to remain at this level until radial release. In addition there is extensive experimental

evidence that as the droplet impinges on the target, the peak pressure moves outward with the point of contact and increases in magnitude until lateral jetting (radial flow) begins. The duration of the droplet impact is probably too short to allow sufficient time for steady flow to be completely established.

SECTION III

IMPACT THEORY

In the following section, hydrodynamic theory is applied to the impact of a soft body against a flat target. Equations are derived for the pressures generated during impact. Much of this theory is based on the ideas presented in the Literature Survey. Concepts from various disciplines have been combined to develop a comprehensive impact theory. Initially, the normal impact of a right circular cylinder onto a rigid plate is considered. Next, several special cases are considered, including oblique impact, impact of a yawed projectile, impact of a projectile with a curved leading edge, addition of porosity to the projectile material, and the impact onto a non-rigid target. A subsection is included which explains the development of the equations of state used to represent soft body materials. A significant portion of this work deals with altering the equations of state to account for the presence of porosity. Finally, the limitations of this impact theory are presented.

1. HYDRODYNAMIC THEORY

When a projectile of any material impacts a target plate, the particles on the front surface of the projectile are instantaneously brought to rest relative to the target face and a shock is formed. The purpose of this shock wave is to bring each succeeding layer of particles to rest. The shock compression of a layer of particles is so rapid that the particles away from the edge of the projectile do not have time to "communicate" with the free surface. This implies that these particles behave as if they are in a semi-infinite medium which can undergo only plane strain compression. Thus, shock compression in a bounded medium is usually considered to be a plane strain process.

The pressure in the shock compressed region is very high initially and is constant throughout the region at early times. As the shock propagates up the projectile, the particles along the projectile's edge are subjected to a very high pressure gradient due to the shock loading

on one side and the free surface on the other. This pressure gradient causes the particles to be accelerated radially outward and a release wave is formed. The function of this release wave is to relieve the radial pressures in the projectile.

A very complicated state of stress begins to develop in the projectile. The radial pressure release causes shear stresses to appear. The radial acceleration of the particles also results in tensile stresses being developed. If, at any time, the state of stress is such that the strength of the material is exceeded, the material will "flow". For soft body impact, it will be assumed that the stresses throughout the impact event greatly exceed the material strength, so that the flow will continue indefinitely. For these materials, to a first approximation the material strength can be neglected so that they can be considered to behave as fluids.

After several reflections of the release waves, a condition of steady flow is established. A constant pressure and velocity field is set up in the projectile, and the particles flow along paths which are fixed in space, called streamlines.

In the following section, a hydrodynamic impact theory will be used to study the mechanisms involved in soft body impact. In order to simplify the analysis, the case of a homogeneous, right-circular cylinder impacting normally on a rigid plate will be considered initially. By assuming the target to be rigid, the response of the target material to the impact pressures can be neglected. This simplifies the problem and allows the researcher to concentrate on the response of the projectile. Several assumptions are implicit in this theory. The projectile material will be considered homogeneous, even when high amounts of porosity are considered. As stated previously, the strength of the projectile material will be neglected. Also, in order to simplify the analysis, the material viscosity and the frictional forces along the impact surface will be neglected.

a. Shock Regime

For the normal impact of a cylinder on a rigid plate, the flow across a shock can be considered one-dimensional and adiabatic, irreversible. Figure 1-b illustrates a shock wave propagating into a fluid at rest, where u_s is defined as the velocity of the shock propagating into the fluid at rest and u_p is the velocity of the particles behind the shock in this reference system. From this figure, it can be seen that the particle velocity is actually the change in velocity across the shock.

Figure 1-b illustrates the case for which the velocities are all measured relative to the fluid in the shocked state. This case is synonymous with the impact of a cylinder on a rigid plate. The projectile's initial velocity is seen to be u_0 and it is brought to rest behind the shock.

In order to write the conservation laws across the shock, the steady state shock condition must be considered. This case is shown in Figure 1-c.

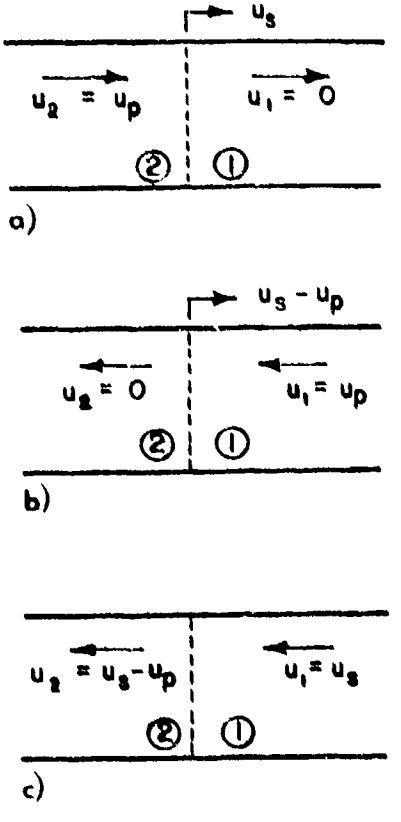

Figure 1. One Dimensional Shock Flow. a) Shock Propagating into a Fluid at Rest, b) Flow Brought to a Rest Across the Shock, c) Standing Shock.

For this case, the equations of conservation of mass (continuity) and momentum may be written

$$\rho_1 u_s = \rho_2 (u_s - u_p) \tag{1}$$

$$P_1 + \rho_1 u_s^2 = P_2 + \rho_2 (u_s - u_p)^2 \tag{2}$$

Combining these two equations, the pressure behind the shock is found to be

$$P_2 - P_1 = \rho_1 u_s u_p \tag{3}$$

The pressure in the shocked region, given by Equation 3, is often referred to as the Hugoniot pressure. Throughout the remainder of this report, this pressure will be represented by the notation, P_H. For the impact of a cylinder on a rigid plate, it can be seen that $u_p = u_o$. Thus, for this case, Equation 3 becomes

$$P_H = \rho_1 u_s u_o \tag{4}$$

For very low impact velocities, the shock velocity, u_s, can be approximated by the isentropic wave speed in the material, c_o. Thus, for low impact velocities, Equation 4 may be approximated by the relation

$$P_H = \rho_1 c_o u_o \tag{5}$$

As stated in the Literature Survey, many researchers believed that the shock pressure generated during the impact of water on a rigid surface could be given by Equation 5. Kinslow (Reference 39) apparently used this relation in expressing shock pressures for a water jet impact at 633 m/s. Although this relation may be adequate for very low velocity impact, it deviates markedly from Equation 4 for higher velocities. Figure 2 demonstrates the differences in pressures found from these two relationships for water. At Mach = 1.0, Equation 5 gives a shock pressure of only 1/3 that of the actual value given by Equation 4. Kinslow's results, for a velocity of 633 m/s, are seen to be in error by more than 40%.

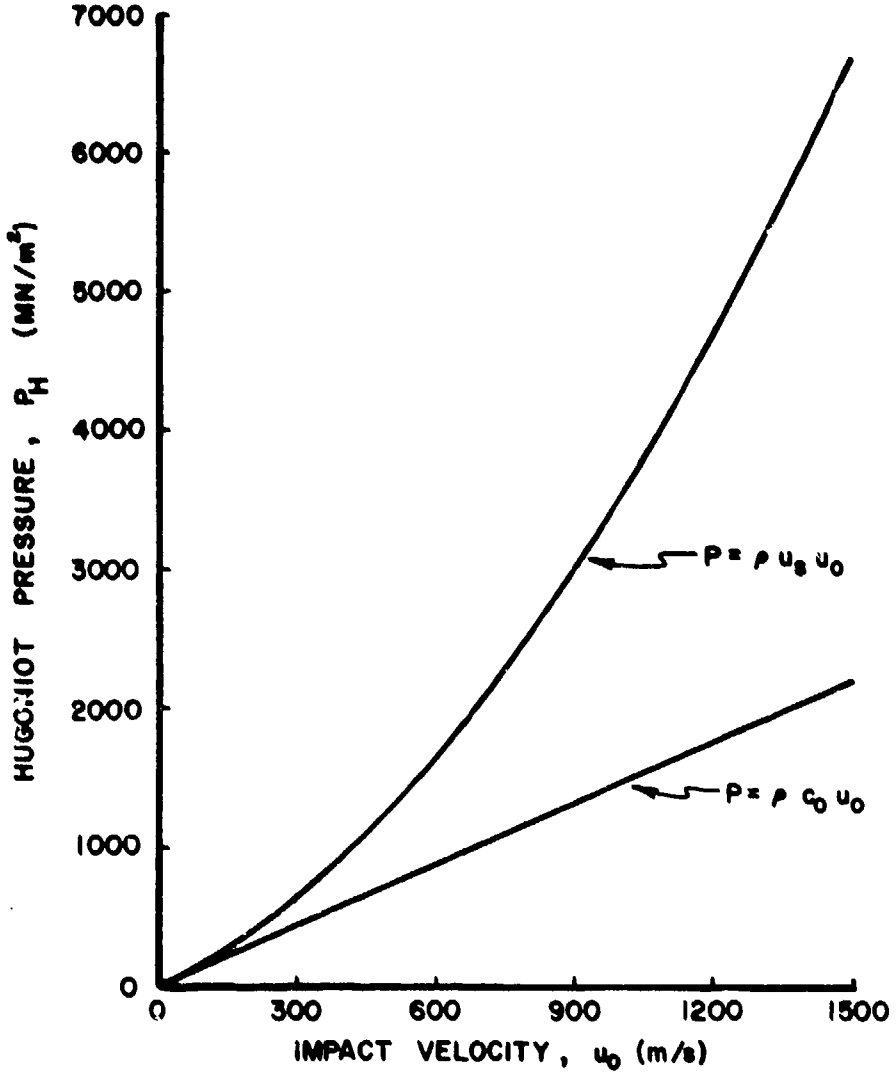

Figure 2. Effect of Compressibility on the Hugoniot Pressure for Water. (1 MN/m^2 = 10 Bars)

b. Release Regime

As soon as the shock is formed, it begins to propagate up the projectile and radial release waves propagate in towards the center axis of the projectile. The problem can no longer be considered one-dimensional in nature. For the normal impact of a cylinder, the problem becomes two-dimensional, axisymmetric.

Figure 3 shows the release regime of impact for a cylinder with an original L/D of 2. Figure 3-b illustrates the shocked region in the

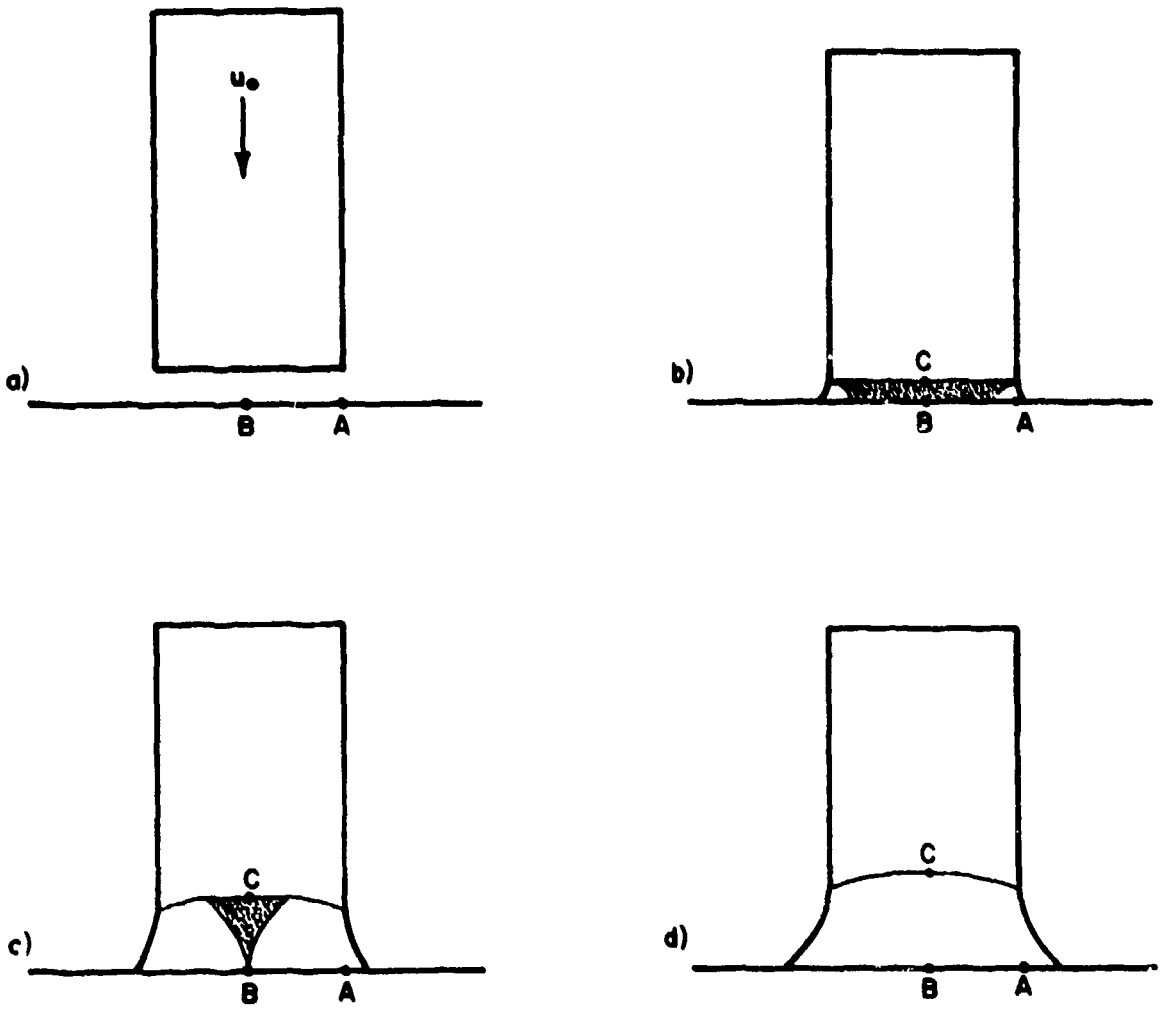

Figure 3. Shock and Release Waves in Fluid Impact.

projectile just after impact. The pressure in the shocked region is given by Equation 4. It should be noted that the velocities of the shock and release waves are much greater than the initial velocity of the projectile. Figure 3-c shows the moment when the release waves have converged on Pt. B, the axis of the cylinder. Figure 3-d shows the moment when the release waves have just caught the center of the shock, Pt. C. The region of fully shocked material no longer exists. The curvature of the shock is due to the release process, which has progressively weakened the shock, thereby decreasing the shock velocity.

Several reflections of the release wave are probably necessary to establish steady flow. The existence of steady flow, of course, is dependent on the length (or L/D) of the cylinder. For very short cylinders, the impact event will be over before the release regime has ended. Although there is no simple, analytical method for studying the release regime, several critical items can be identified.

The duration of the shock pressure at the center of impact can be approximated by the amount of time that it takes the initial release wave to reach the center, Pt. B of Figure 3-c. The release wave can be considered to be a fan of weak expansion waves, which implies that the release process can be considered isentropic. The velocity of the initial release wave is just the speed of sound in the shocked material, c_r, which is given by the expression

$$c_r^2 = (dP/d\rho)_{P_H} \tag{6}$$

which is the slope of the isentropic pressure-density curve at the Hugoniot state. Thus, the expression for the time necessary for the release wave to initially reach the center is

$$t_B = a/c_r \tag{7}$$

where a is the initial radius of the cylinder. Figure 4 shows the speed of sound in the shocked region, c_r, plotted versus impact velocity for water. Using this information, the duration of the Hugoniot pressure, t_B, can be obtained from Equation 7. Figure 5 shows the relationship between t_B and the impact velocity, u_o, for cylindrical projectiles of water of various radii. (The equation of state of water is given in a later section).

Another important item is the time that it takes the front of the release wave to just capture all of the shock wave. As stated previously, immediately upon impact the release wave begins to interact with the shock at the edge of the projectile. Since the wave speed in the fully shocked medium is always greater than the shock speed, the release wave will interact with progressively more of the shock as the

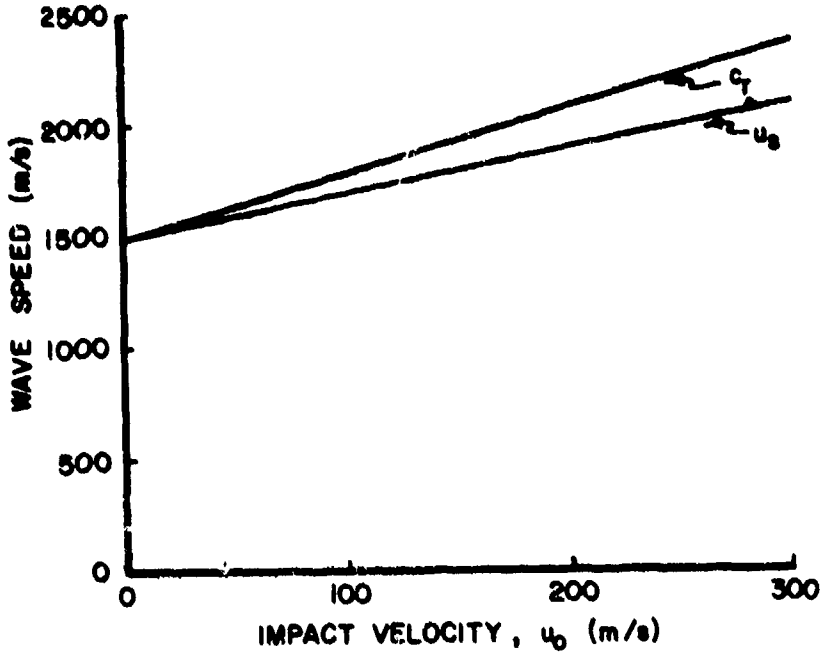

Figure 4. Comparison of the Shock Velocity, u_s, and the Sound Speed in the Shocked Region, c_r.

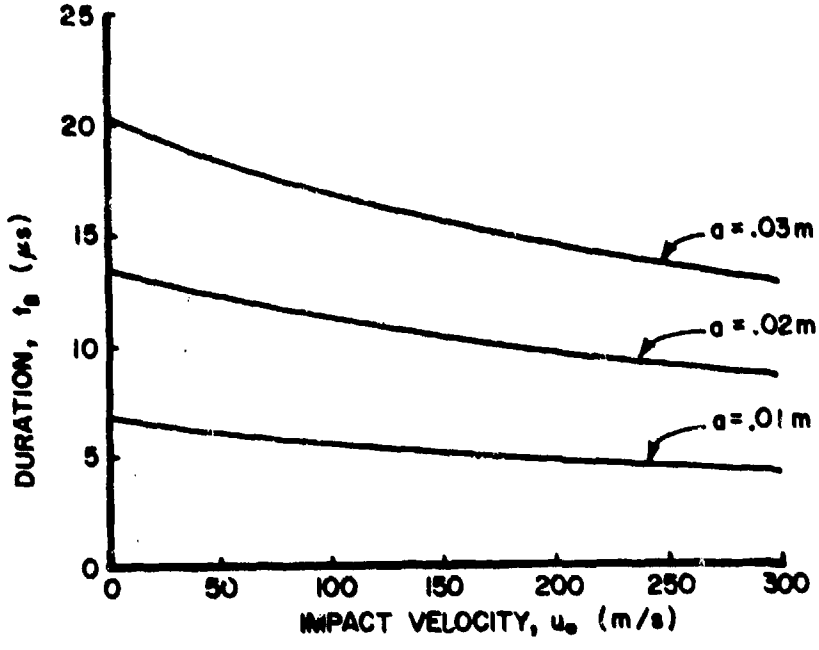

Figure 5. Variation of the Duration of the Hugoniot Pressure with Impact Velocity for a Cylindrical Projectile of Water.

impact continues. Figure 3-d shows the condition in which the release waves have just converged on Pt. C. After this time, the pressure in the region behind the shock will rapidly decay. The time of this occurrence, t_c, may be derived from geometric considerations. In order for the release wave starting at Pt. A to interact with the shock at Pt. C, it must travel a radial distance, a, and an axial distance equal to the axial distance traveled by the shock. At the time of intersection, the shock has propagated a distance

$$x_s = (u_s - u_o)t_c \tag{8}$$

where $(u_s - u_o)$ is the velocity of the shock relative to the target as seen in Figure 1-b. From this it can be seen that the release wave will have traveled a distance

$$x_r = (x_s^2 + a^2)^{\frac{1}{2}} \tag{9}$$

in the time, t_c, given by the expression

$$t_c = x_r/c_r \tag{10}$$

Thus, it can be seen that

$$t_c = \frac{a}{(c_r^2 - (u_s - u_o)^2)^{\frac{1}{2}}} \tag{11}$$

From Equation 11 an expression can be derived for the critical projectile length, L_c, which is the length for which the radial release wave will just intersect the shock on axis, Pt. C, as the shock reaches the end of the projectile. Again, from geometry, it can be seen that

$$L_c = u_s t_c \tag{12}$$

Combining Equations 11 and 12 and nondimensionalizing, it is seen that

$$(L/D)_c = \frac{u_s}{2(c_r^2 - (u_s - u_o)^2)^{\frac{1}{2}}} \tag{13}$$

For a projectile with an $L/D < (L/D)_c$, the shock will reflect off the projectile rear surface before it has all been captured by the radial release waves. The shock will be reflected in the form of a rarefaction wave. This rarefaction wave could complicate the impact event

by causing a tensile failure in the projectile, decreasing the incoming velocity of the end of the projectile, and disturbing the radial release process.

However, for a projectile with an $L/D > (L/D)_c$, the shock will be substantially weakened by the release waves prior to reaching the projectile rear surface and its effects will be reduced or effectively cancelled. Figure 4 showed both u_s and c_r as a function of impact velocity for water. Using these values, $(L/D)_c$ for a cylinder of water can be obtained from Equation 13. Figure 6 shows a plot of $(L/D)_c$ versus impact velocity for water.

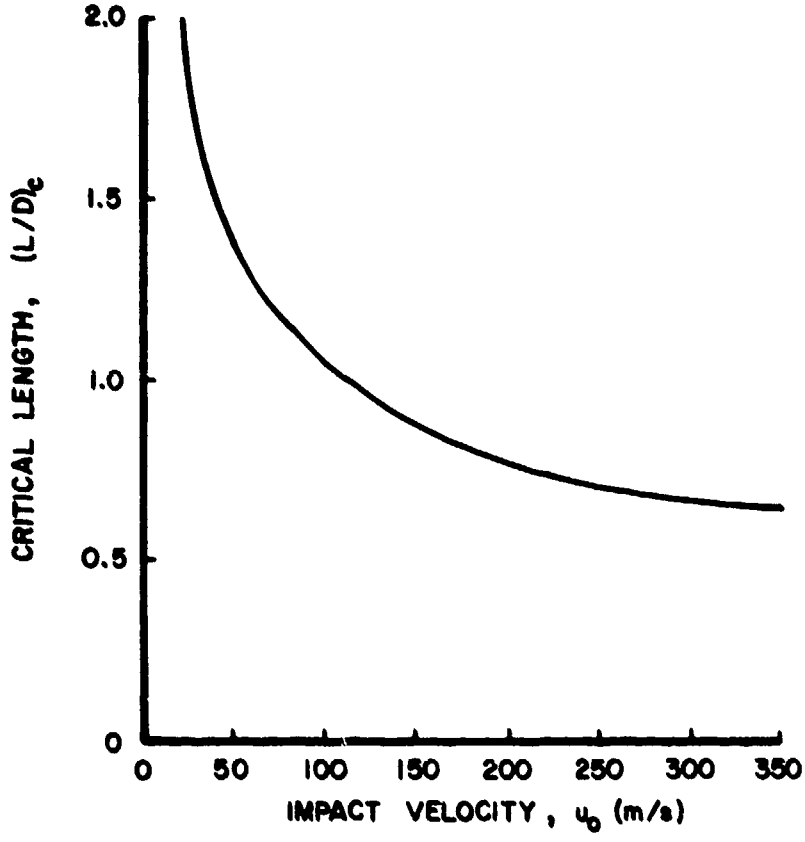

Figure 6. Variation of Critical Length with Impact Velocity for Water.

For a projectile of sufficient length, steady flow should be set up up after several reflections of the radial release waves. It seems likely that for a projectile with a length somewhat greater than L_c, a condition of steady flow should exist for some time.

c. Steady Flow Regime

During the release phase, the shock is constantly being weakened by the release waves, with an accompanying decrease in shock velocity. For a low velocity impact (subsonic), the shock wave will be weakened to the point that it will disappear. By this time, for steady flow, streamlines will be established. However, for a supersonic impact, the shock wave will not disappear. Instead, its velocity will decrease until it becomes a standing shock. Behind this standing shock, the flow will be subsonic and will follow steady state streamlines. Because of the standing shock, the velocity and pressure fields set up in the fluid will be different for the two cases.

(1) Subsonic Flow

If it is assumed that the shearing forces and body forces are negligible throughout the flow field and that all stream properties vary continuously in all directions, then along each streamline, Bernoulli's Equation can be written

$$\int \frac{dP}{\rho} + \int u\, du = K \qquad (14)$$

where K is constant along the streamline and may vary from one streamline to another. For the case of a cylinder impacting a rigid plate, the flow field is essentially uniform at some distance away from the impact surface, so that the K must be the same for each of the streamlines in this region. This implies that K has the same value throughout the entire flow field. For this case, the pressure P, at any point in the flow field can be related to the velocity, u, at that point by the relation

$$\int_{P_o}^{P} \frac{dP}{\rho} + \int_{u_o}^{u} u\, du = 0 \qquad (15)$$

where P_o and u_o are the pressure and velocity of the uniform flow field some distance away from the impact surface and are approximated by the atmospheric pressure and the initial impact velocity.

In order to obtain the pressure at any point along the impact surface from Equation 15, the velocity at that point must be known and the equation of state of the material, $\rho = \rho(P)$, must be known. The equations of state for soft body materials will be discussed in a later section. The expression for the velocity at a point is not found so easily. For a two-dimensional fluid jet, the velocity field in the fluid was obtained by Milne-Thompson (Reference 55) from potential flow theory. However, no closed form solution of potential flow theory has been developed for a circular jet. The normal approach is to assume an expression for the velocity field based on empirical data.

In this approach, the pressure at the center and the pressure at the edge are found using Equation 15. Then a general expression for the pressure distribution is assumed based on empirical data. This expression is forced to satisfy the pressure boundary conditions and conservation of momentum.

For the normal impact of a uniform, cylindrical projectile on a rigid plate, axial symmetry dictates that the point at the center of the plate be the stagnation point. The pressure at the center of the plate is the stagnation pressure, P_s (gage pressure), and the velocity at the center is zero. Therefore, at the center of the plate, Equation 15 takes the form

$$\int_{P_o}^{(P_s + P_o)} \frac{dP}{\rho} = \frac{u_o^2}{2} \tag{16}$$

If the fluid is assumed incompressible, Equation 16 gives

$$P_s = \tfrac{1}{2} \rho u_o^2 \tag{17}$$

For most materials, the density tends to increase the applied pressure, so that Equation 16 implies

$$P_s \geq \tfrac{1}{2} \rho u_o^2 \tag{18}$$

The second pressure boundary condition is that the pressure must go to zero at some radial distance from the center.

Simple momentum considerations require that during steady flow, the impulse imparted to the target by a unit of fluid must be equal to the axial momentum lost during impact. This may be written

$$\int_{o}^{t_D} (F\ dt) = \int_{u_o}^{u} (M\ du) \tag{19}$$

where the force, F, is assumed constant during steady flow and the duration of impact is represented by t_D. For a unit of fluid with initial values of mass M, density ρ, length L, and cross-sectional area A, this expression becomes

$$F\ t_D = M(u-u_o) \tag{20}$$

For most soft body materials, the rebound velocity after impact, u, is so small that it may be ignored. Also, during steady flow, the duration of impact for a unit of fluid of length, L, is simply the time required for the fluid to flow through its length. That is,

$$t_D = L/u_o \tag{21}$$

Thus, the force generated in the steady flow regime is seen to take the form

$$F = \rho A u_o^2 \tag{22}$$

Since the force is simply the integral of the pressure over the impact surface, this expression may be rewritten

$$2\pi \int_{o}^{\infty} Pr\,dr = \rho A u_o^2 \tag{23}$$

From the above arguments, it is evident that any assumed expression for pressure must predict the pressure to be maximum at the center, given by the stagnation pressure P_s, decreasing with radius to a value of zero at some point, and that the expression for pressure must satisfy Equation 23.

As stated in the Literature Survey, both Banks and Chandrasekhara (Reference 56) and Leach and Walker (Reference 58) developed expressions

for the pressure distribution due to the normal impact of a water jet. The expression of Banks and Chandrasekhara took the form

$$P = \tfrac{1}{2} \rho u_o^2 \exp \{-\zeta_1 (\tfrac{r}{a})^2\} \tag{24}$$

and that of Leach and Walker took the form

$$P = \tfrac{1}{2} \rho u_o^2 \{1-3(\tfrac{r}{\zeta_2 a})^2 + (\tfrac{r}{\zeta_2 a})^3\} \tag{25}$$

where r is the radial distance from the center, a is the initial radius of the jet, and ζ_1 and ζ_2 are constants used to make Equations 24 and 25 conform to Equation 23. For this case, ζ_1 = 0.5 and ζ_2 = 2.58. Figure 7 shows a plot of Equations 24 and 25.

The main drawback to these two expressions is that they define a maximum pressure at the center, P_s, of 1/2 ρu_o^2. As was shown earlier, this is only true exactly for an incompressible fluid. For a compressible material, the pressure will be greater. The effect of compressibility on the stagnation pressure can be demonstrated by

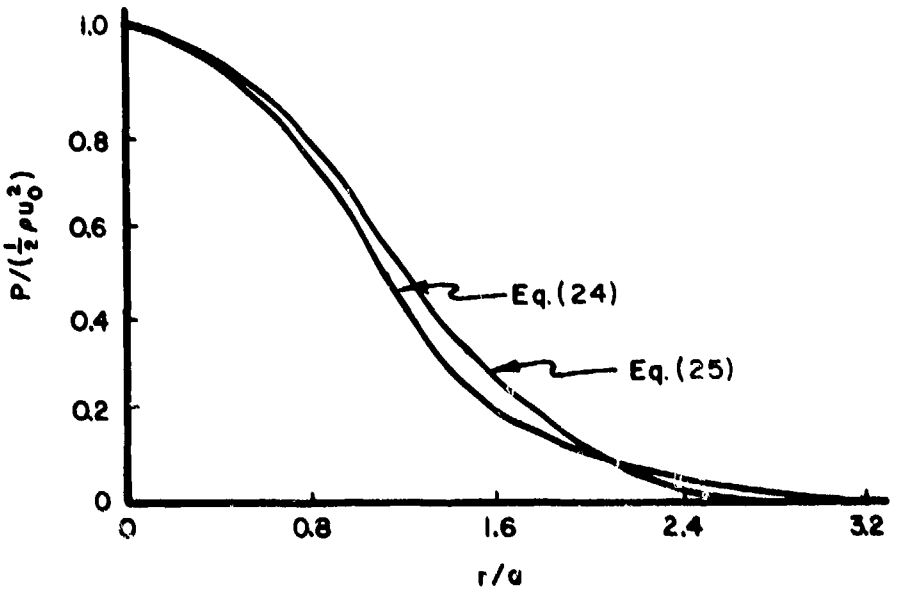

Figure 7. Radial Distribution of Steady Flow Pressure.

considering the impact of a cylinder of water. Using the equation of state for water which is given in a later section, Bernoulli's compressible equation in the form of Equation 15 can be solved for P_s. Figure 8-a shows the results. Although the stagnation pressure is not dramatically different from $1/2\ \rho u_o^2$ for low velocities, the difference is evident at higher velocities. This pressure difference would be even greater for very compressible materials.

For soft body impacts, Equations 24 and 25 may be generalized to allow for the increased stagnation pressure due to compressibility. Thus, they may be written

$$P = P_s \exp\{-\zeta_1(\frac{r}{a})^2\} \tag{26}$$

and

$$P = P_s\{1-3(\frac{r}{\zeta_2 a})^2 + 2(\frac{r}{\zeta_2 a})^3\} \tag{27}$$

respectively, where the constants ζ_1 and ζ_2, derived in Appendix A, are given by Equations A-7 and A-9

$$\zeta_1 = P_s/\rho u_o^2$$

$$\zeta_2 = (3.33\ Pu_o^2/P_s)^{\frac{1}{2}}$$

The effect of compressibility on the pressure distribution should be evident. Figure 8-a shows that for an impact velocity of u_o = 1400 m/s, $P_s = 1.14\ (1/2\rho u_o^2)$. Figure 8-b shows a plot of Equation 27 using this value of P_s.

(2) Supersonic Flow

For the supersonic impingement of a fluid jet normally onto a rigid plate, a standing shock is set up in the flow. The change in particle velocity across the shock may be small. However, the flow behind the shock will be subsonic because of the greatly increased local sound speed.

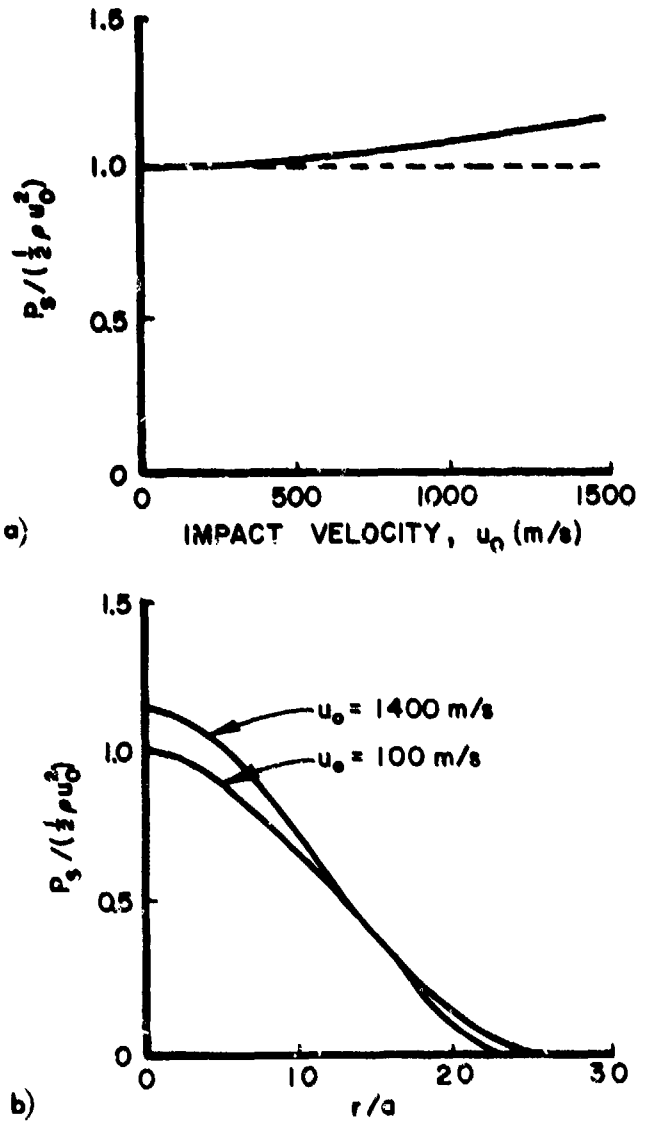

Figure 8. Compressibility Effects in Steady Flow. a) Stagnation Pressure, b) Pressure Distribution.

In the previous section on subsonic flow, Bernoulli's Equation was used to relate the pressures along the impact surface to the pressure, P_o, density ρ_o, and velocity, u_o, in the uniform flow region. However, for supersonic flow this approach cannot be used since the standing shock is a discontinuity surface and Bernoulli's Equation only holds in a continuous flow field. Instead, the change in stream properties across the shock must be evaluated using shock relations. Bernoulli's Equation can then be used throughout the flow field behind the shock. Figure 9 illustrates this case. Region 1 in front of the shock is a uniform flow field and the stream properties in this region are the initial properties, namely P_o, ρ_o, and u_o. In Region 2 just behind the shock, the properties may not be constant over the cross section since the shock may not be a perfectly plane shock. However, at the center axis, the shock can be assumed plane and one-dimensional shock equations can be used. The properties along the axis just behind the shock will be designated P_2, ρ_2, and u_2.

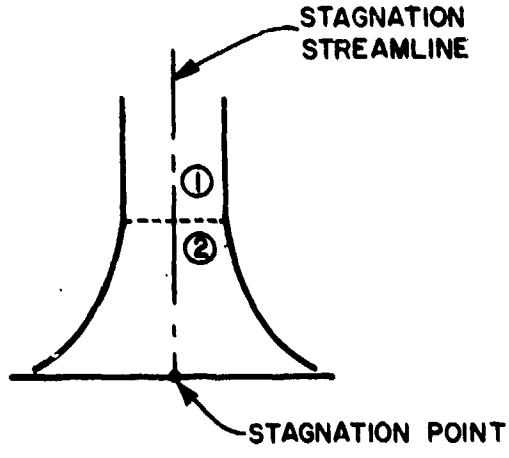

Figure 9. Standing Shock in Steady Flow.

Since no uniform flow field exists behind the shock, Bernoulli's Equation will take the form

$$\int_{P_2}^{P} \frac{dP}{\rho} + \int_{u_2}^{u} u\, du = 0 \tag{28}$$

and will hold only along the streamline which passes through the center of the projectile and the stagnation point in the center of the impact region.

The case of a standing shock was shown in Figure 1-c. For this case, Equations 4 and 1 take the form

$$P_2 = \rho_o u_s u_p \tag{29}$$

where

$$\rho_o u_s = \rho_2 (u_s - u_p) \tag{30}$$

$$u_s = u_o \tag{31}$$

$$u_p = u_o - u_2 \tag{32}$$

One more equation is needed in order to solve this set of equations. Such an equation, relating the shock velocity, u_s, with the particle velocity, u_p, will be given for various soft body materials in a later section. Thus, for a given set of initial conditions and a given material, Equations 29, 30, 31, and 32 can be solved for P_2, ρ_2, and u_2.

Using these values, the pressure at the stagnation point on the surface of the plate can be found using Bernoulli's Equation of the form

$$\int_{P_2}^{P_s} \frac{dP}{\rho} = \frac{u_2^2}{2} \tag{33}$$

In this relationship, the equation of state of material must be the pressure-density relationship for an isentropic compression passing through the points P_2, ρ_2.

As in the subsonic flow case, once P_s is determined, Equations 26 and A-7 or 27 and A-9 can be used to develop an expression for the pressure distribution along the surface of the plate.

d. Termination of Impact

As stated previously, the particles of fluid flow along streamlines which are set in space. These streamlines are curved near the plate surface so that the impacting material is "turned" during impact. For subsonic flow, as the fluid nears the target surface there is a gradual decrease in velocity with a corresponding increase in local pressure. Thus, during steady flow there is a pressure field set up in the fluid in which the local pressure is maximum at the stagnation point and decreases to the atmospheric pressure, P_o, at a substantial distance from this point. As the end of the projectile nears the impact surface, it enters this field of increasing local pressure and disrupts the field due to the immediate drop in pressure behind the projectile rear surface. For supersonic impact, this happens when the projectile end passes through the standing shock. In either case, release waves emanate from the rear surface and propagate to the impact surface, thereby causing a slight decrease in the impact velocity of the rear surface as well as a decrease in the pressure along the impact surface of the target. This process continues until the end of the projectile reaches the surface of the plate and the impact event is ended.

As stated earlier in Equation 21, the total duration of the impact can be approximated by the time needed for the projectile to "flow through" its length, or $t_D = L/u_o$. Deviation from this could be caused by the decrease in projectile velocity due to release waves from the back surface of the projectile.

2. SPECIAL CONSIDERATIONS

In the last section a theory was presented concerning the normal impact of a right-circular cylindrical projectile of fluid against a rigid target. However, there are several other cases of special interest. Included among these is the oblique impact of a right-circular cylinder, the normal impact of a yawed projectile, and the normal impact of a

projectile with a curved leading edge. Next, the porosity of the projectile material is seen to have a great effect on the impact pressure. Finally, the impact of a fluid projectile against a nonrigid target is considered.

a. Projectile Yaw

Figure 10-a presents the normal impact of a right-circular cylinder in which the axis of the cylinder is yawed by an angle ϕ to the velocity vector. The amplitude of the shock Hugoniot pressure will be the same as that for a projectile impacting without yaw. However, the duration of this pressure at various points along the target surface will differ if the yaw angle, ϕ, is greater than the critical angle, ϕ_{cr}.

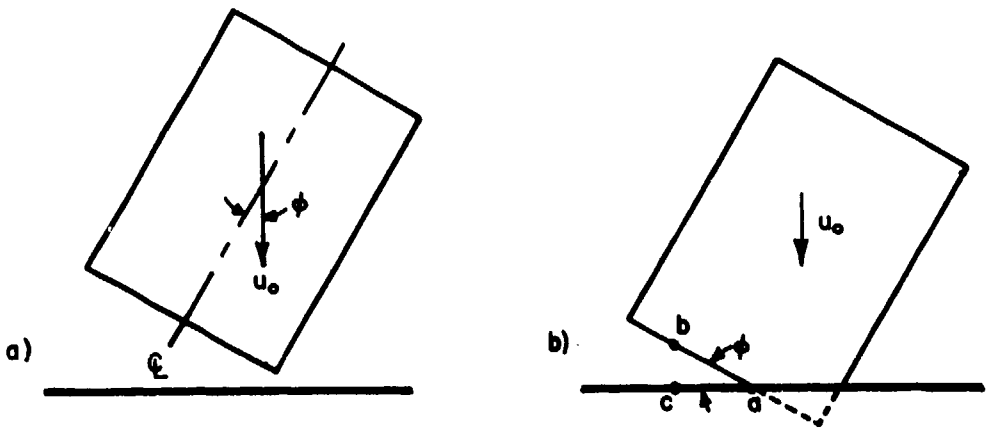

Figure 10. The Impact of a Yawed Projectile.

In Figure 10-b, the projectile is seen during initial impact. If the shock originating at point a arrives at point b prior to point b reaching the impact surface, then a release wave will develop and propagate back into the shocked region. The critical angle, ϕ_{cr}, is the angle of yaw for which the shock will just reach point b at the instant point b reaches the surface. From the figure, it can be seen that for $\phi = \phi_{cr}$, the ratio of the distance traveled by point b, $\overline{bc}$, to the

distance traveled by the shock, $\overline{ab}$, must be equal to the ratio of the velocity of point b, u_o to the shock velocity, u_s. This may be written

$$\text{for } \phi = \phi_{cr}, \qquad \frac{\overline{bc}}{\overline{ab}} = \frac{u_o}{u_s} \tag{34}$$

From geometry, it is evident that

$$\sin \phi_{cr} = \frac{\overline{bc}}{\overline{ab}} \tag{35}$$

Thus, the relationship for the critical angle becomes

$$\phi_{cr} = \sin^{-1}\left(\frac{u_o}{u_s}\right) \tag{36}$$

The critical angle changes with velocity for most materials since the shock velocity is normally a function of the impact velocity.

For an impact in which the yaw is less than the critical angle, the amplitude and duration of the shock pressure at the various points over the surface will be essentially the same as that for the impact of a projectile without yaw. However, for an impact in which the yaw is greater than the critical angle, the full shock Hugoniot pressure will exist only at the initial point of impact. At each of the other points on the impacting surface of the projectile, the material will have been shocked and partially released before impacting the surface, thereby reducing the shock pressure generated upon impact. Also, the duration of the shock pressures at the center will be decreased due to the immediate formation of release waves.

b. Projectile Leading Edge Curvature

For the impact of a curved surface on a flat target, the angle, ϕ, which the impacting surface makes with the target surface increases as the impact progresses. This condition is demonstrated in Figure 11.

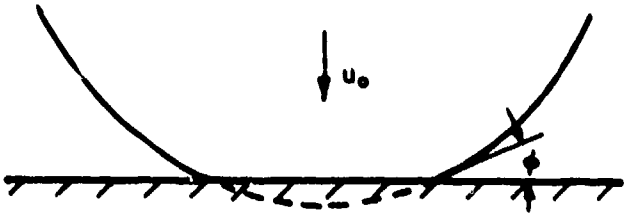

Figure 11. The Impact of a Curved Surface on a Flat Target.

Once the angle ϕ exceeds ϕ_{cr} as defined by Equation 36, a release wave will form and propagate into the shocked region. This implies that the duration of the Hugoniot shock at the center will be less for the impact of a sphere than for a cylinder (without yaw) of like diameters.

c. Oblique Impact

Figure 12-a demonstrates the oblique impact of a right-circular cylinder against a rigid plate in which the velocity vector is directed along the axis of the cylinder and intersects the target at an angle α relative to the target surface.

(1) Shock Regime

For the oblique impact of a projectile on a rigid plate, a coordinate transformation aids in the understanding of the shock process. From Figure 12-a it is evident that the component of projectile velocity normal to the plate is $u_o \sin \alpha$ and the component tangential to the plate is $u_o \cos \alpha$. Figure 12-b shows the impact in the transformed

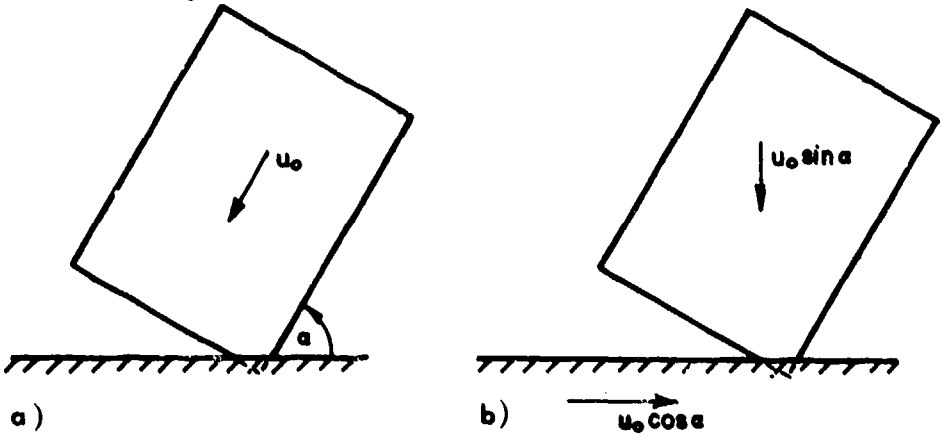

Figure 12. Oblique Impact of a Cylinder on a Rigid Plate.

coordinate system in which the projectile is seen to impact normally onto the moving plate. Assuming the frictional forces along the surface are negligible, this case is identical to the normal impact of a yawed projectile with an initial velocity of $u_o \sin \alpha$. Correspondingly, the Hugoniot shock pressure will be identical to that produced by a normal impact of a projectile with an initial velocity of $u_o \sin \alpha$. Figure 13 demonstrates the decrease in shock pressure with impact angle of obliquity for the impact of a cylinder of water.

(2) Release Regime

The release process is similar to that of the yawed projectile. For this case, the angle that the impacting projectile surface makes with the target surface is seen to be governed by the relation $\phi = 90°-\alpha$. For the impact in which $\phi > \phi_{cr}$, the full Hugoniot pressure will occur only at the initial point of impact.

(3) Steady Flow

The steady flow phase of impact for a fluid cylinder is shown in Figure 14. From momentum considerations it can be seen that the majority of fluid will flow "downstream". This causes the stagnation point to shift "upstream" of the center of the plate. As long as a stagnation point exists, the pressure at that point will be given by Equation 16. Thus, the maximum pressure generated during steady flow will be independent of the angle of impact. However, the distribution of pressure along the surface will be greatly dependent on the impact angle.

Although no expression for pressure distribution in an oblique impact of a circular jet has been developed, Taylor (Reference 59) developed a distribution for a two-dimensional (plane) jet of water. This distribution is shown in Figure 15 for an impact angle, α, of 30°. In this figure, the profile of the projectile is superimposed on the pressure distribution to demonstrate the distance that the stagnation point, s, has shifted upstream from the center of impact.

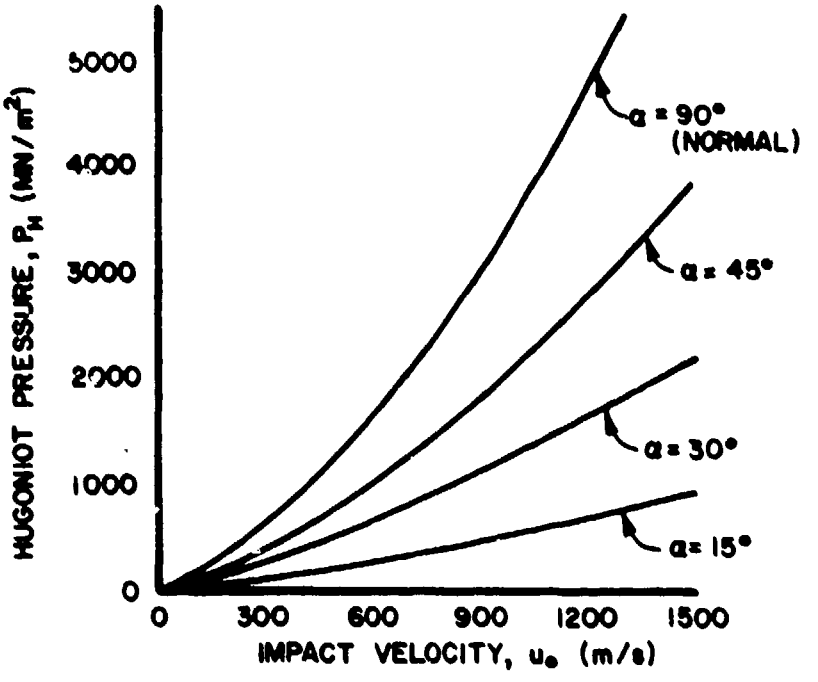

Figure 13. Variation of Hugoniot Shock Pressure with Angle of Impact for Water. (1 MN/m^2 = 10 Bars)

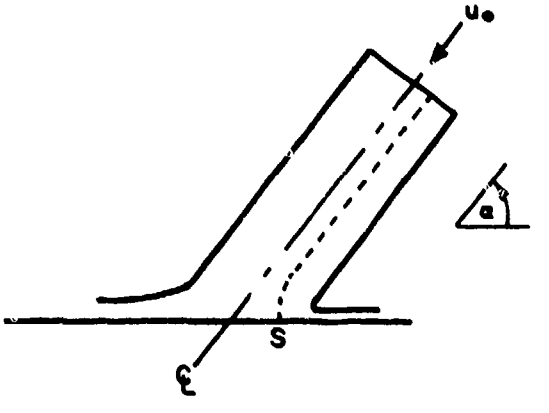

Figure 14. The Steady Flow Phase of an Oblique Impact.

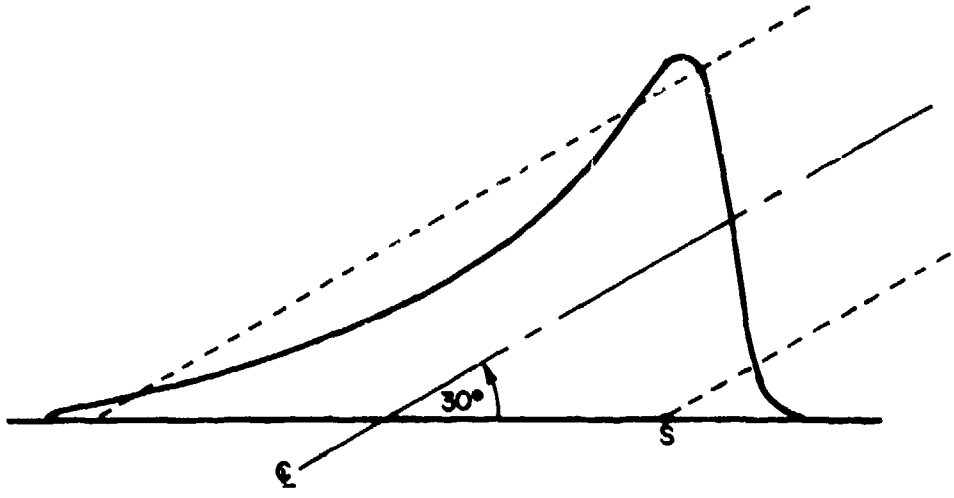

Figure 15. Steady Flow Pressure Distribution for a 30° Impact of a Plane Jet of Water (Taylor, Reference 59).

From simple momentum considerations, Equation 22 stated that the total force exerted on the target at any instant of time for a normal impact could be given by the relation $F = \rho A u_o^2$. However, the momentum transferred to the target during an oblique impact is only the normal component of the total momentum. Thus, for an oblique impact, Equation 22 can be rewritten

$$F = \rho A u_o^2 \sin \alpha \qquad (37)$$

For normal impact, $\alpha = 90°$ and Equation 37 reduces to Equation 22. Thus, the pressure distribution for an oblique impact is seen to be different from that for a normal impact, due both to the decrease in total force and the loss of axial-symmetry.

d. Material Porosity

In the previous section on Hydrodynamic Theory, the Hugoniot shock pressure was presented as a function of impact velocity for water in Figure 2. Later, in Figure 7, the distribution of steady flow pressure was given for the impact of a jet of water. In both of these cases, the water was assumed to have no porosity. As will be seen in the next section on Equations of State of soft body materials, the presence of

porosity has a great effect on both the shock velocity and compressibility of a material during impact. Thus, the equation of state for a porous material differs from that of a nonporous material.

The decrease in shock velocity due to proosity results in a marked decrease in the shock pressures. Figure 16 presents the variation in Hugoniot pressure with porosity, z, for the normal impact of a cylinder of water. (As defined in the next section, z is simply the volume fraction of air in the water). Likewise, the decrease in density due to the addition of porosity causes a decrease in the stagnation pressure during steady flow. However, the increase in compressibility effects tend to counteract this, so that the resulting decrease is relatively small. Figure 17 presents the variation in the steady flow stagnation pressure for water with porosity.

In Figure 8, the alteration of the steady flow pressure distribution due to compressibility effects was presented. In that case, the increased material compressibility resulted from increased impact velocity. Compressibility effects are even more pronounced for materials which have porosity. Figure 18 presents the pressure distribution for both porous and nonporous water using Equation 27. In this figure, the pressure is nondimensionalized with respect to the incompressible flow pressure $1/2\rho_z u_o^2$, where ρ_z, defined in the next section by Equation 58, is the average density of the porous water for this case. Also, the radial distance from center is nondimensionalized relative to the initial projectile radius, a.

e. Non-Rigid Target

Up to this point the theory has been concerned with impact on a rigid plate. However, all real target materials are non-rigid to some extent. Thus, the response of the target during impact cannot be overlooked. If the target material can be assumed to behave elastically, the initial target response is straightforward. At very early times during the impact, only the local area of the target directly under

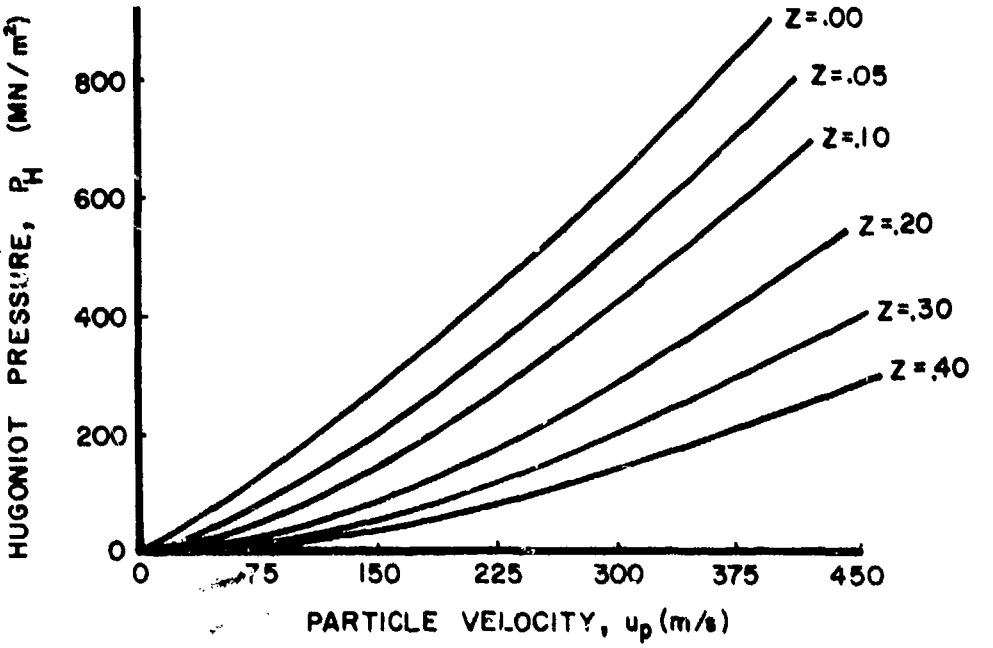

Figure 16. Relationships Between the Hugoniot Shock Pressure and Particle Velocity for Water with Various Porosities. (1 MN/m^2 = 10 Bars)

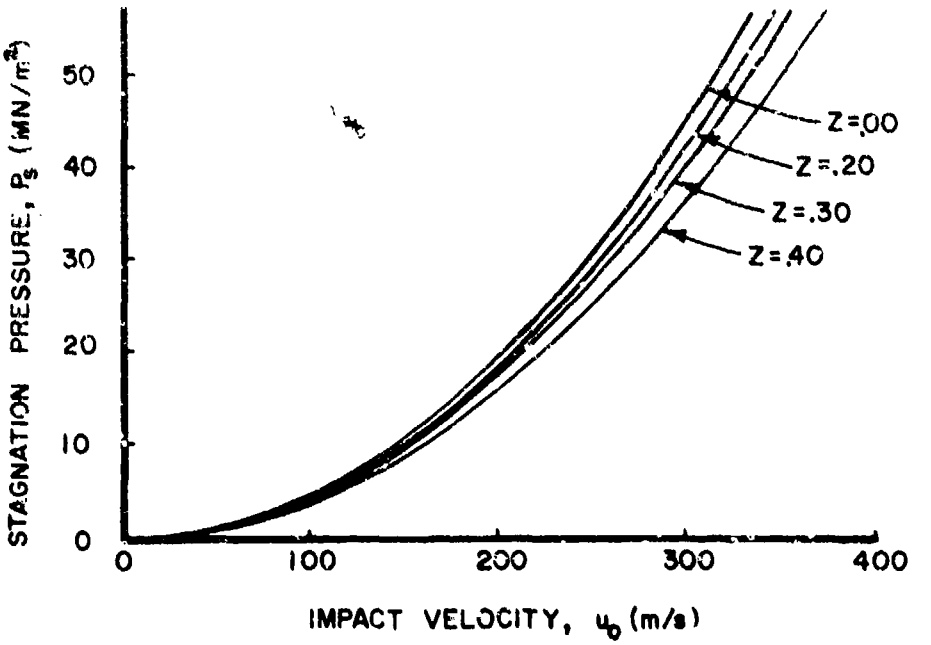

Figure 17. Relationships Between the Stagnation Pressure and the Impact Velocity in Steady Flow for Water with Various Porosities. (1 MN/m^2 = 10 Bars)

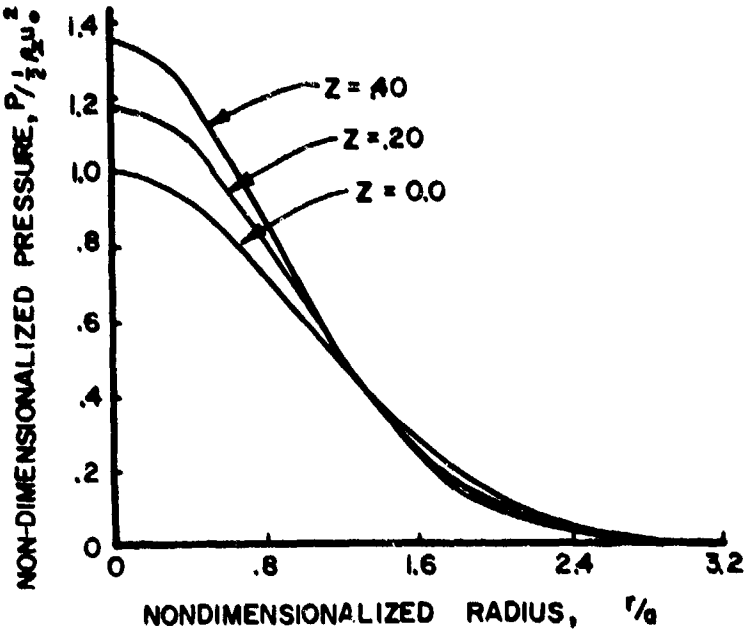

Figure 18. The Variation in Steady Flow Pressure Distribution for Water Due to the Addition of Porosity.

the impacting projectile is affected by the impact. Figure 19 illustrates this early shock regime. From this figure it is evident that to a first approximation the shock waves may be considered initially planar, and one-dimensional shock equations can be used for the target as well as the projectile.

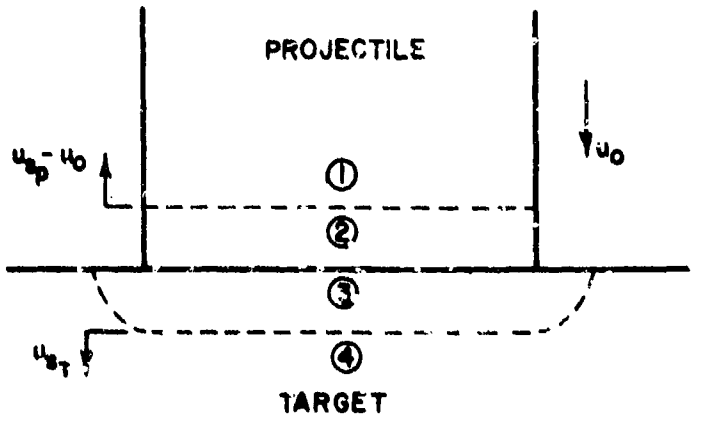

Figure 19. Impact on an Elastic Target During the Early Shock Phase.

In Figure 19, Region 2 is the shocked region in the projectile and Region 3 is the shocked region in the target.

For the impact on a non-rigid target, Equation 4 is seen to take the form

$$P_H = \rho u_s u_p \tag{38}$$

where u_p, the particle velocity, is no longer equal to the initial impact velocity. In Regions 2 and 3, Equation 38 may be written

$$P_2 = \rho_p \, u_{s_p} \, u_{p_p} \tag{39}$$

$$P_3 = \rho_t \, u_{s_t} \, u_{p_t} \tag{40}$$

At the projectile-target interface, equilibrium requires that

$$\begin{aligned} P_2 &= P_3 \\ u_2 &= u_3 \end{aligned} \tag{41}$$

From the definition of particle velocity, it can be seen that

$$u_{p_p} = u_o - u_2 \tag{42}$$

$$u_{p_t} = u_3 - u_4 = u_3 \tag{43}$$

Thus, the particle velocities can be related by the expression

$$u_{p_t} = u_o - u_{p_p} \tag{44}$$

Substituting Equation 44 into Equation 40 and equating the pressures P_2 and P_3 gives

$$\rho_p u_{s_p} u_{p_p} = \rho_t u_{s_t} (u_o - u_{p_p}) \tag{45}$$

From this, it can be seen that

$$u_{p_p} = u_o \left\{ \frac{\rho_t u_{s_t}}{\rho_p u_{s_p} + \rho_t u_{s_t}} \right\} \tag{46}$$

Thus, the pressures generated at the projectile-target interface for the impact of an elastic target material are seen to be

$$P = \rho_p u_{s_p} u_o \left\{ \frac{\rho_t u_{s_t}}{\rho_p u_{s_p} + \rho_t u_{s_t}} \right\} \tag{47}$$

To demonstrate the difference between the pressures predicted by Equation 4, which assumes a rigid target, and Equation 47, several calculations were made for the normal impact of water on various targets at a velocity of 200 m/s. For the impact on steel, the shock pressure found using Equation 47 is approximately 4% less than that found using Equation 4. For titanium, the difference is approximately 8%; for aluminum, approximately 11%; and for polycarbonate, approximately 35%.

For thin targets, the initial shock wave in the target reflects off the rear surface as a tensile wave of similar strength. This wave propagates back to the impact surface, causing a decrease in the shock pressures at the surface. Continuing wave reflections cause an increase in the local particle velocity of the target and a decrease in pressure. As the impact proceeds, the entire target structure develops a velocity along the initial axis of impact. The net result of this target deformation is that the relative velocity between the projectile and target decreases with a resulting decrease in the flow pressures.

3. EQUATIONS OF STATE

In order to determine the pressures generated during impact, the material properties of the projectile and target must be known. These are applied to the problem through the equation of state of the materials.

a. Shock Compression

The expression for the initial shock pressure is given by Equation 4, $P_H = \rho_0 u_s u_0$. In this expression, ρ_0, the initial density, and u_0, the initial velocity, are known for any given impact. Thus, in order to solve for the shock pressure, a second expression is needed which relates the response of the projectile material under shock loading.

It has been found that for most solids and fluids (including water and air) the relationship between the shock velocity and particle velocity can be expressed as

$$u_s = c_o + k\, u_p \tag{48}$$

where k is a constant for the material and c_0 is the sound speed (velocity of propagation of an infinitesimal disturbance) in the material. This relationship, often called the "linear Hugoniot", will be used to represent all soft body materials in this research. It can be substituted into Equation 4 directly (by recalling that for normal impact of a rigid target, the particle velocity, u_p, is simply the initial velocity of the projectile). Thus, Equations 4 and 48 are sufficient for determining initial shock pressure.

However, it is also desirable to obtain a relationship between the pressure and density on both sides of the shock by combining Equation 48 with Equations 1 and 4. Equation 1, the continuity equation across the shock, may be written in the form

$$\frac{u_p}{u_s} = 1 - \frac{\rho_1}{\rho_2} = q \tag{49}$$

where the subscripts 1 and 2 refer to Region 1 in front of the shock and Region 2 behind the shock.

Substituting this relationship into Equation 48 gives

$$u_s/c_o = 1/(1-kq) \tag{50}$$

and Equation 4 may be written in the form

$$P_2 = \rho_1 u_s u_p \tag{51}$$

Thus, substituting Equations 49 and 50 into Equation 4 gives

$$P_2 = \rho_1 c_o^2 q/(1-kq)^2 \tag{52}$$

Another approximate expression for the pressure-density relationship across a one-dimensional shock was given by Cogolev, et al. (Reference 60), and takes the form

$$P_2 = A\left\{\left(\frac{\rho_2}{\rho_1}\right)^B - 1\right\} \tag{53}$$

where A and B are material constants. Ruoff (Reference 61) has demonstrated that for a material which exhibits a linear Hugoniot, Equation 48, the constants may be approximated by the expressions

$$\begin{aligned} A &= \rho_1 c_o^2/(4k-1) \\ B &= 4k-1 \end{aligned} \tag{54}$$

where k is the constant in Equation 48.

Thus, the pressure and density behind the shock can be obtained from either Equations 52 or 53 if the relationship between the shock velocity and particle velocity can be approximated by Equation 48. For water, Heymann (Reference 35) showed that Equation 48 provides a quite accurate fit to the data up to Mach 1.2 (approximately 1800 m/s).

b. Isentropic Compression

The expression for the steady flow pressure is Bernoulli's compressible equation, Equation 15,

$$\int_{P_o}^{P} \frac{dP}{\rho} + \int_{u_o}^{u} udu = 0$$

In order to solve this equation for a given impact velocity, the pressure-density relationship in isentropic compression must be given for the projectile material.

For very low pressure levels, two simple expressions are often used to approximate the isentropic pressure-density relationship for solids and liquids. The first is simply

$$\rho = \text{constant} \tag{55}$$

Although never exact, the assumption of incompressibility can often be used for low velocity impacts without causing considerable error. This, of course, will not be true for porous materials.

The second relationship is obtained from the definition of the bulk modulus

$$\beta = -\rho \frac{dP}{d\rho} \tag{56}$$

For very low pressures, β, the bulk modulus, is often assumed constant. For more accuracy, a relationship of the form

$$\beta = \beta_o + \beta_1 P + \beta_2 P^2 + \ldots. \tag{57}$$

may be assumed.

However, for the pressures normally generated during soft body impacts, the assumptions of incompressibility and constant bulk modulus are inadequate. Instead, equations of state accurate to pressures of several hundred MN/m^2 (several kilobars) are needed. In this pressure

range, the isentropic pressure-density relationships for most solids and fluids, including water, can be approximated by the Hugoniot shock relationship (Reference 62) given by Equations 52 or 53.

c. Effect of Porosity

It has been stated that for most soft body materials, Equations 52 or 53 can be used to describe the pressures and densities resulting from both isentropic compression and shock compression. Both of these equations are based on a linear Hugoniot relationship, Equation 48. It has been observed that departure from linearity is usually due to porosity or phase change (Reference 63).

Although phase changes do not occur in the soft body impacts of interest, many of the soft body materials are porous. The cellular structure of animal and vegetable matter normally contains a small amount of porosity. Rubber, in its many uses, is often used with large amounts of porosity. Thus, for these materials, Equations 52 and 53 are not representative.

In order to develop isentropic and shock relationships which will hold for porous materials, a simple theory by Torvik (Reference 64) will be considered. Torvik's theory predicts the pressure-density relationship across a shock for a homogeneous mixture based on the pressure-density relationships of each constituent. Although Torvik used this theory to develop a pressure-density relationship under shock compression, there is no reason why it should not be used also to develop the isentropic relationship. Thus, in this report, Torvik's theory has been used to develop both shock and isentropic relationships for mixtures of which one component is air. The derivation of both the shock and isentropic relationships using this theory are presented in Appendix B. The main assumptions made are that the porous material is macroscopically homogeneous and isotropic and that the density of each constituent of the mixture is the same as that for a homogeneous sample of that constituent of the same pressure.

In the context of this report, a porous material is defined simply as a mixture in which one of the constituents is air. The amount of porosity of the material, z, will be defined as the volume fraction of air in the mixture. If the full density of the soft body material (density with no porosity present) is represented by ρ_f and the average density of the soft body material with porosity is represented by ρ_z, then from Equation B-1 it can be seen that the average density of the material can be defined by the expression

$$\rho_z = z\ \rho_{air} + (1-z)\ \rho_f \tag{58}$$

where the volume fraction of air, fv_n, has been replaced by z and the volume fraction of the soft body material by the term (1-z). For the materials of interest $\rho_f >> \rho_{air}$, so that Equation 58 can be approximated by the relationship

$$\rho_z = (1-z)\ \rho_f \tag{59}$$

For a porous soft body material, the isentropic pressure-density relationship can be obtained from Equation B-9. Substituting the terms just defined, this equation becomes

$$\frac{\rho_{z1}}{\rho_{z2}} = (1-z)\left(\frac{P_2}{A} + 1\right)^{-1/B} + z\left(\frac{P_2}{P_1}\right)^{-1/\gamma} \tag{60}$$

where the subscript 1 refers to the initial (unstressed) state and the subscript 2 refers to the final (stressed) state, A and B are empirical constants given by Equation 54, and α is the ratio of specific heats of air. Similarly, the shock pressure-density relationship can be obtained from Equation B-18 and takes the form

$$\frac{\rho_{z1}}{\rho_{z2}} = (1-z)\left(\frac{P_2}{A} + 1\right)^{-1/B} + z\ (1-q) \tag{61}$$

where q is defined in Equation B-17. The difference in the isentropic and shock relations is due to the fact that the pressure-density relationships for air are different for these two cases, whereas these relationships have been assumed the same for the soft body material.

The effect of porosity can best be demonstrated by applying Equations 60 and 61 to the case of water with varying amounts of porosity added. The properties of water are given in Appendix C. Figure 20 shows two plots of Equation 61 for this case in which porosity is varied from 0 to 40%. Figure 20-a shows the variation in specific volume (density^{-1}) with pressure up to 500 MN/m^2 (5 kbar) and Figure 20-b looks at the lower portion of these curves for pressures up to 20 MN/m^2. The relationship between the particle velocity and the shock velocity for porous materials is obtained by simultaneous solution of Equations 1, 3, and 61. This relationship is shown in Figure 21 for water with porosity added. From the solution of these three equations, the relationship between the shock pressure and particle velocity is also obtained. This relationship was used in an earlier section to determine the effect of porosity on the shock pressures generated during impact. Figure 16 shows the Hugoniot shock pressure as a function of impact velocity and porosity for the impact of water onto a rigid plate.

The isentropic pressure-density relationship, Equation 60, for water with porosity is shown in Figure 22 (for water, volume = (density^{-1}). In isentropic compression, the volume of air in the mixture is seen to vanish under substantial pressure. Simultaneous solution of Equations 15 and 60 result in the relationship between steady flow pressure and impact velocity. This relationship was used in a previous section to derive the variation in the steady flow pressure at the stagnation point to the amount of porosity in a projectile of water. This information was presented in Figure 17.

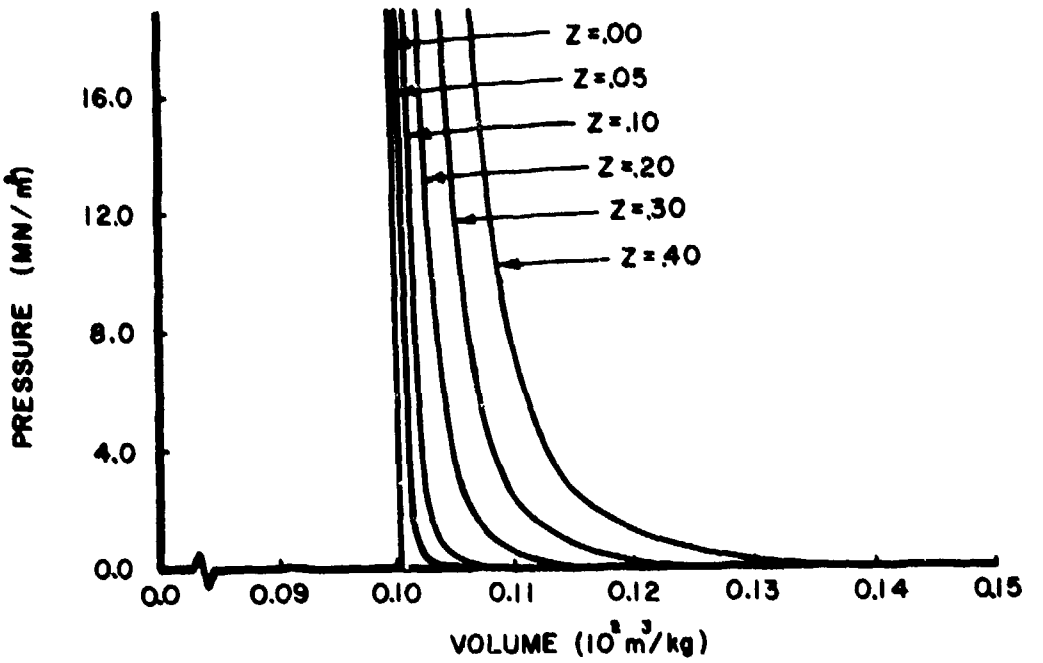

a

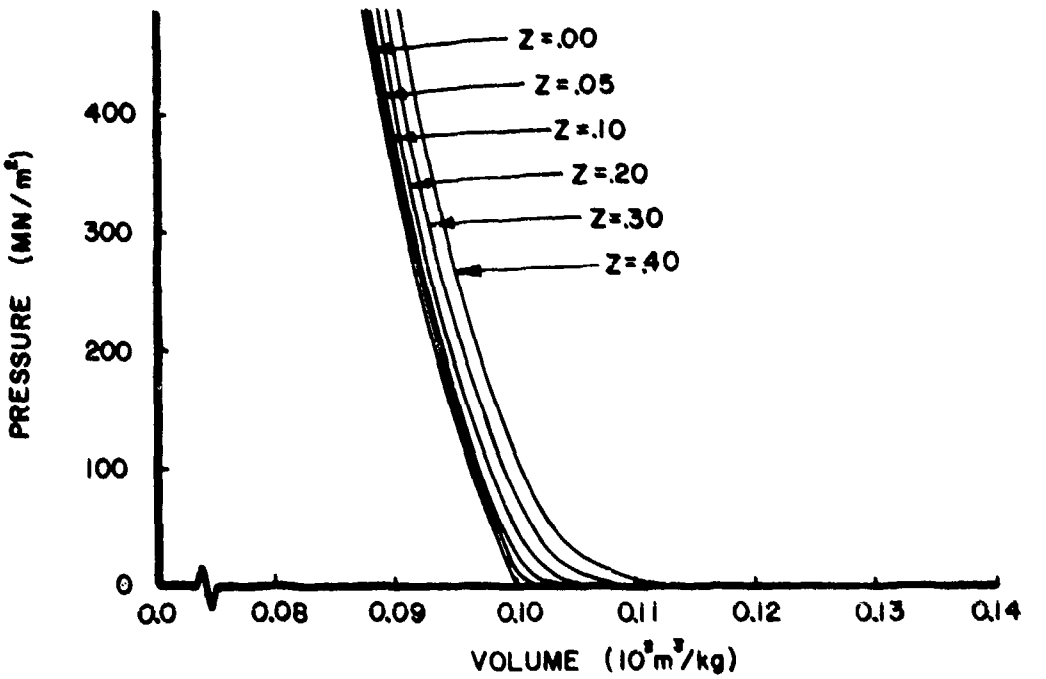

b

Figure 20. Hugoniot Pressure-Volume Relationships for Water with Various Porosities. (1 MN/m^2 = 10 Bars)

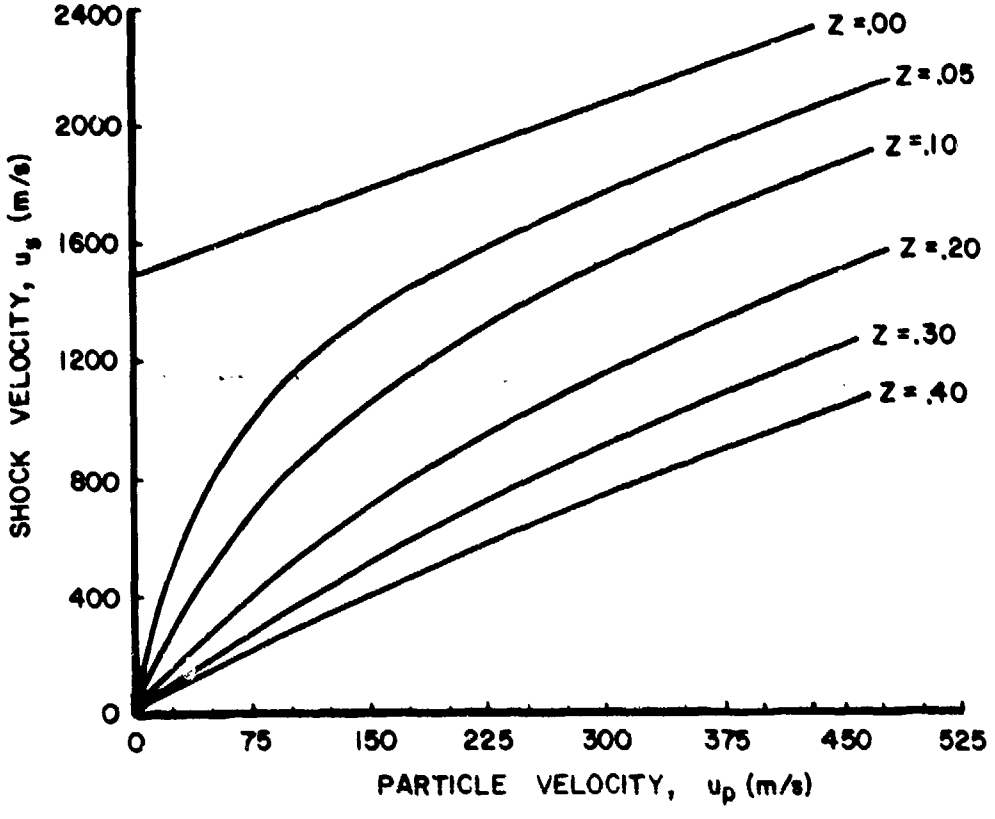

Figure 21. Relationships between the Shock Velocity and the Particle Velocity for Water with Various Porosities.

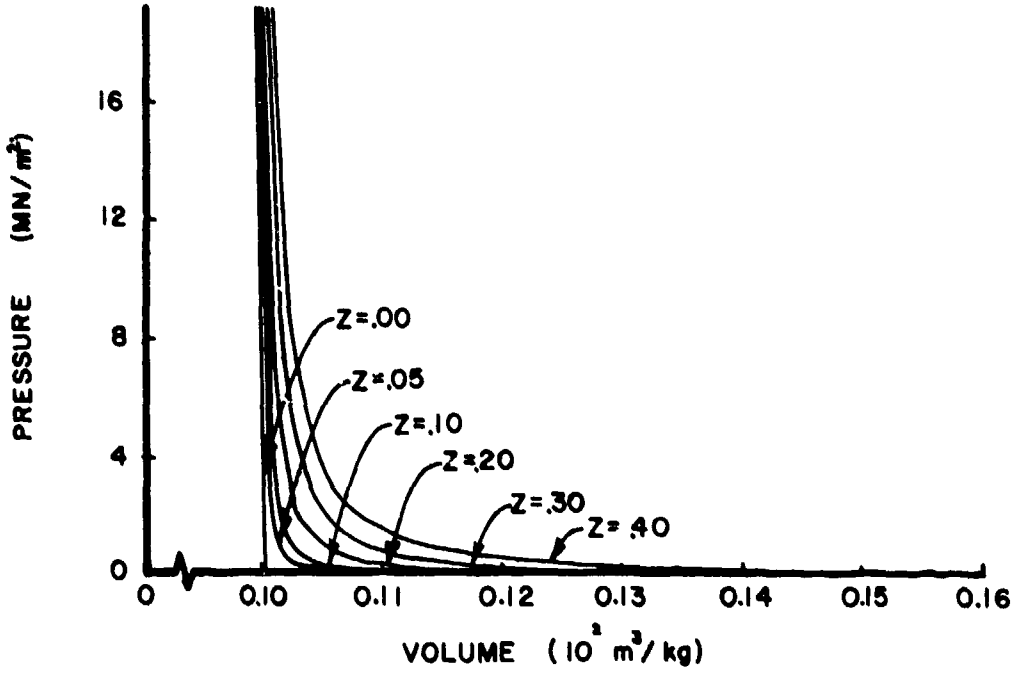

a

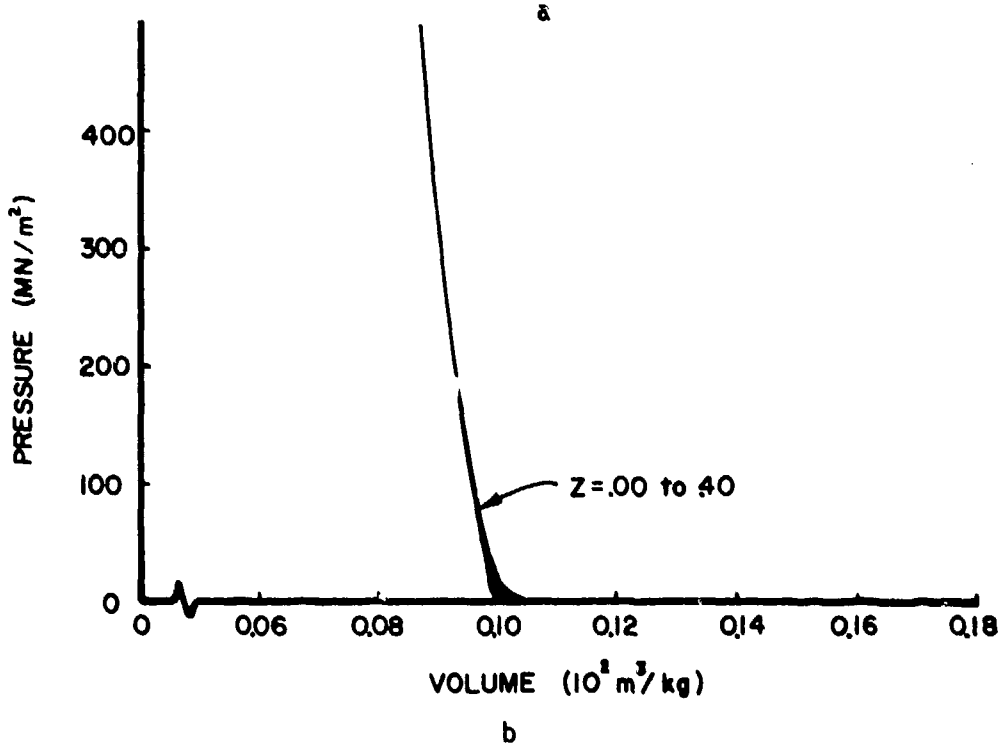

b

Figure 22. Isentropic Pressure-Volume Relationships for Water with Various Porosities. (MN/m^2 = 10 Bars)

4. LIMITATIONS OF THE THEORY

The basic theory assumes that a soft body can be treated as a homogeneous fluid during impact. The main case described was the impact of a right-circular cylinder against a rigid plate, with other cases being studied briefly. The extent to which the theory is limited in application will now be considered.

Application of this theory to nonhomogeneous materials may result in several errors. Variations of density in the material will result in variations of the flow pressure. Secondly, mixture theory, which is the basis of the equations of state for porous materials, requires that the material be macroscopically homogeneous. If this is not so, the propagation of waves in the material will be affected, with an accompanying deviation in the shock velocity and shock pressure.

As stated earlier, a material may be treated as a fluid during impact if the pressures generated during impact are much greater than the strength of the material. For a projectile with a length-to-diameter ratio (L/D) of approximately one or less, this probably requires that the Hugoniot shock pressure be an order of magnitude greater than the tensile strength or shear strength of the material. For a projectile with an L/D greater than one, there is an added requirement that the stresses generated in the projectile during steady flow must also exceed the material strengths. However, as will be discussed later in the Results section, it appears that the theory may accurately predict pressure for impacts in which there are large distortions during impact, even though the material strength is not exceeded.

The theory, originally developed for a cylindrical projectile, is not limited to this geometry. However, it is probably the most convenient to study, both theoretically and experimentally. For projectiles which are spherical in shape, there is not sufficient length for steady-flow to be established. However, the initial shock and release processes as explained in the theory should still exist. In order for steady-flow to be established, the projectile must have an L/D greater than one.

Finally, the theory requires that the target remain flat, although limited deflections of the target are allowed. Large distortions of the surface, such as "pocketing" of a plate, are not allowed since the paths of the streamlines will be altered, thereby influencing the flow pressure. Also, the aerial dimensions of the target surface should be several times the diameter of the projectile, so that full turning of the projectile results.

SECTION IV

EXPERIMENTAL TECHNIQUE

The purpose of the experimental program was to measure the forces and pressures generated during soft body impact on a rigid surface. Two basic tests were used in this program. A Hopkinson bar with strain gages was used to measure impulse imparted to the target during the impact and a flat plate with pressure transducers was used to measure the temporal distribution of pressure at various points on the plate surface.

The Hopkinson bar gave a reliable measure of the impulse (or momentum) imparted to the impact surface as well as the relative distribution of impulse during the impact event. The flat plate gave a reliable measure of pressure imparted to the target during the impact although there were an insufficient number of pressure transducers to give the distribution of pressures over the entire surface for any given test. Both of these tests will be presented in greater detail along with the gun system used for launching the projectiles.

1. GUN SYSTEM

All of the impact tests for this program were conducted on the gun range shown in Figure 23. This gun range is located in the Impact Mechanics Facility of the Air Force Materials Laboratory. For these tests, the gun was used in two different configurations. As shown in Figure 23, the projectile was explosively driven during early testing. In later tests, the projectile was driven by compressed air.

a. Powder Gun

Figure 23 shows the original powder gun configuration. During launch, the projectile was housed in a sabot made of high density polyethylene. This heavy sabot was needed to withstand the high acceleration forces generated by the exploding gas. As the sabot traveled down the gun barrel, the high pressure gases behind the sabot were vented in the blast chamber. Complete venting of the high pressure gases was necessary to establish a constant velocity in the projectile

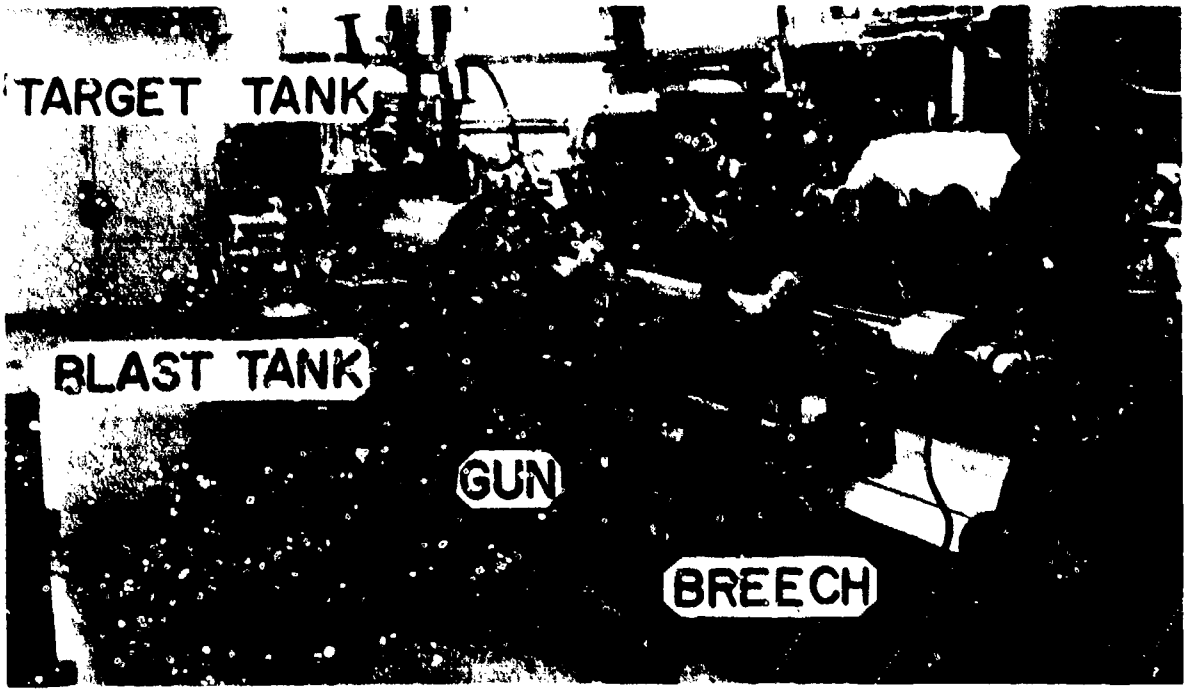

Figure 23. Overall View of the Gun Range Facility Used for Bird Testing.

prior to impact. When the sabot and projectile reached the end of the blast tank, the sabot was trapped by the sabot stopper, shown in Figure 24. The stopper was so designed to allow the projectile to continue its flight without loss of velocity.

The high acceleration forces during early launch and the rapid stopping of the sabot often damaged the projectiles. Requirements for a thick sabot wall also limited projectile diameter to about 5 cm. For these reasons, it was decided to redesign the gun for compressed air. A more complete description of the powder gun can be found in a report by Barber, et al. (Reference 65). Also included in that report is a detailed explanation of the velocity measuring system and the photographic system.

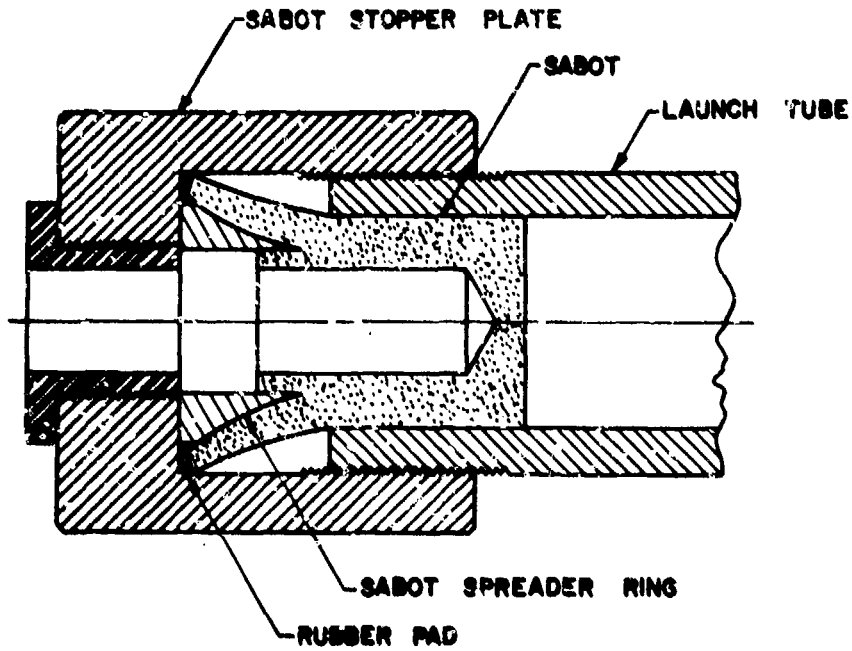

Figure 24. Sabot Stopper for Use with Powder Gun.

b. Compressed Air Gun

During the final phases of this project, projectiles were accelerated by compressed air vented from a large tank. There were many advantages to this system. The heavy, polyethylene sabots were replaced by light, thin-walled balsa wood sabots. This was due to the lower acceleration forces inherent in compressed air guns. Figure 25 is a picture of a typical projectile seated in a balsa wood sabot. In order to separate the projectile from the sabot, a sabot stripper as shown in Figure 26 was used. In this technique, the last section of the gun barrel has a decreasing inner diameter. As the sabot enters this section, it is gently decelerated over a distance of several meters. This slow deceleration enhances a clear separation of the projectile from the sabot. Barber, et al. (Reference 66) presented the compressed air launching system in greater detail.

2. HOPKINSON BAR

In 1914, Hopkinson (Reference 30) reported the use of a circular bar to measure the temporal distribution of force generated during the impact of a lead bullet on the end face of the bar. Previous workers,

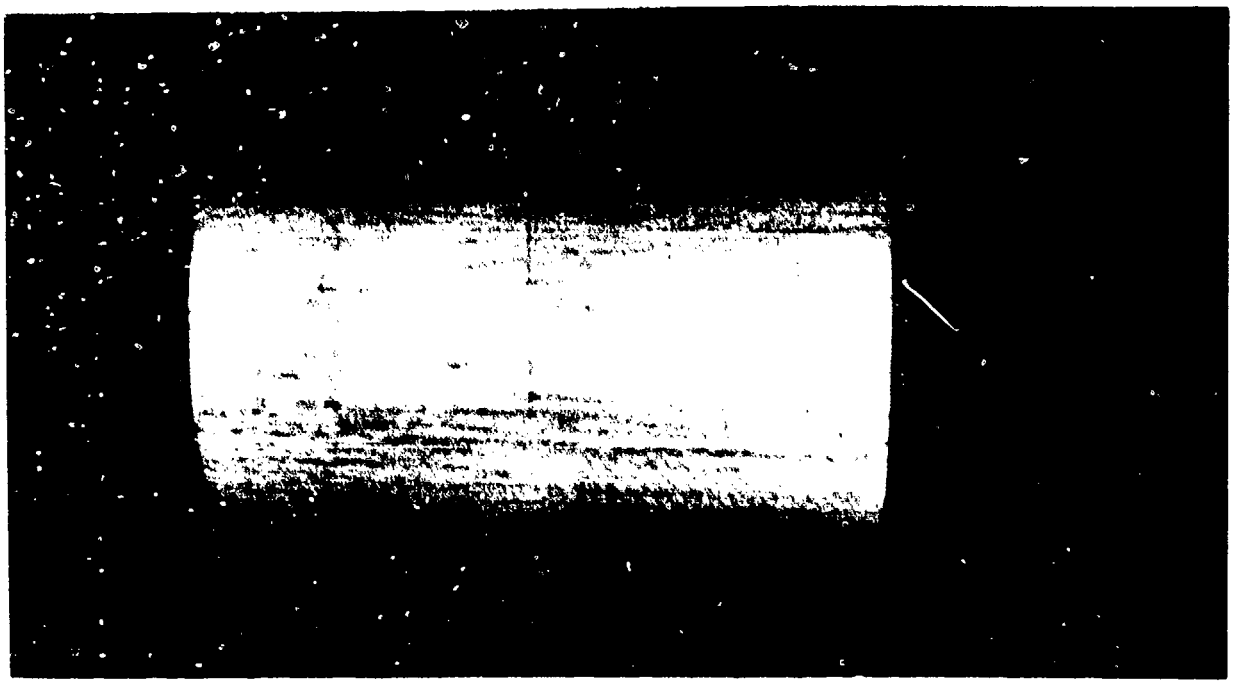

Figure 25. Cylindrical Projectile with Balsa Wood Sabot.

Figure 26. Sabot Stripper for Use with Compressed Air Gun.

suspending a bar as a pendulum, had measured only the total momentum transferred to the bar during an impact on an end face. Hopkinson developed an ingenious method using two bars suspending as pendula, in which one bar was impacted by the bullet and the other acted as a momentum trap. Upon impact of the first bar, a stress wave, generated at the impact surface, propagated down the length of the bar. This wave then passed into the second bar where it was "trapped" and measured by the height of swing of the second bar. By this method Hopkinson was able to resolve the transferred momentum (the impulse) in time, thereby obtaining the force generated during impact as a function of time.

Although this method worked well, it required many impact tests using a like projectile and like velocity in order to resolve the force-time distribution. In the present research programs, the stress waves were measured using strain gages.

a. Theory

When a soft body projectile impacts a Hopkinson bar, a shock wave propagates into the projectile as described earlier. At the same time, a stress wave is generated in the bar. It is essential for a Hopkinson bar test that the pressures generated at the impact surface be much less than the yield strength of the bar material. For this case, the stress wave in the bar will take the form of an elastic wave. As this wave propagates down the bar, the radial stresses will be released rapidly, so that the wave will become a plane stress wave, traveling at the longitudinal wave speed, c_ℓ, of the bar material.

It is essential that the stress wave in the bar be elastic for several reasons. An elastic wave will propagate essentially undisturbed into the bar. Also, the strain measured by the strain gages will be linearly related to the stress at that section of the bar.

The strain gages are normally located at least ten diameters down the bar from the impact end. This is necessary to give the elastic wave sufficient time to become planar so that the average strain in the cross section will be the same as that measured by the gages. For this

case, the strain will be linearly related to the average stress at the cross section and the stress will be related to the force by the area of the cross section.

Figure 27 is an illustration of a Hopkinson bar. When the projectile impacts the end of the bar, the amplitude of the pressures generated vary over the impact surface. The resultant stress wave in the bar is nonplanar. However, by the time the wave reaches the strain gages, it has become planar and the stress measured by the gages is only the average of the initial stress distribution. Since the exact stress distribution cannot be measured, only the total force is used. The relation for force is

$$F = EA\varepsilon \tag{62}$$

where E is the modulus of elasticity of the bar, A is the cross-sectional area of the bar, and ε is the strain recorded.

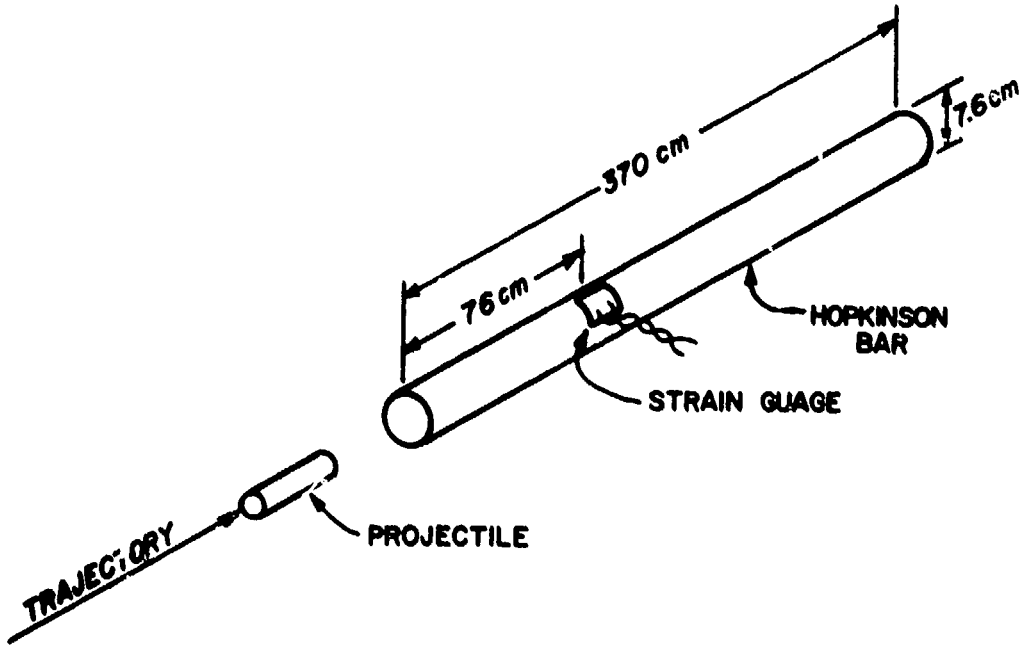

Figure 27. Schematic of Hopkinson Pressure Bar.

Because of the large diameter of the bar, high frequency components of the stress wave are unable to propagate down the bar without being dispersed (Reference 11). Thus, the measured force profile is somewhat different from the actual forces generated at the impact surface. However, even though the force history will be somewhat distorted, the total impulse imparted to the bar can still be obtained by integrating the force-time trace.

b. AFML Facility

Figure 28 is a picture of the aluminum Hopkinson bar mounted in the AFML range.

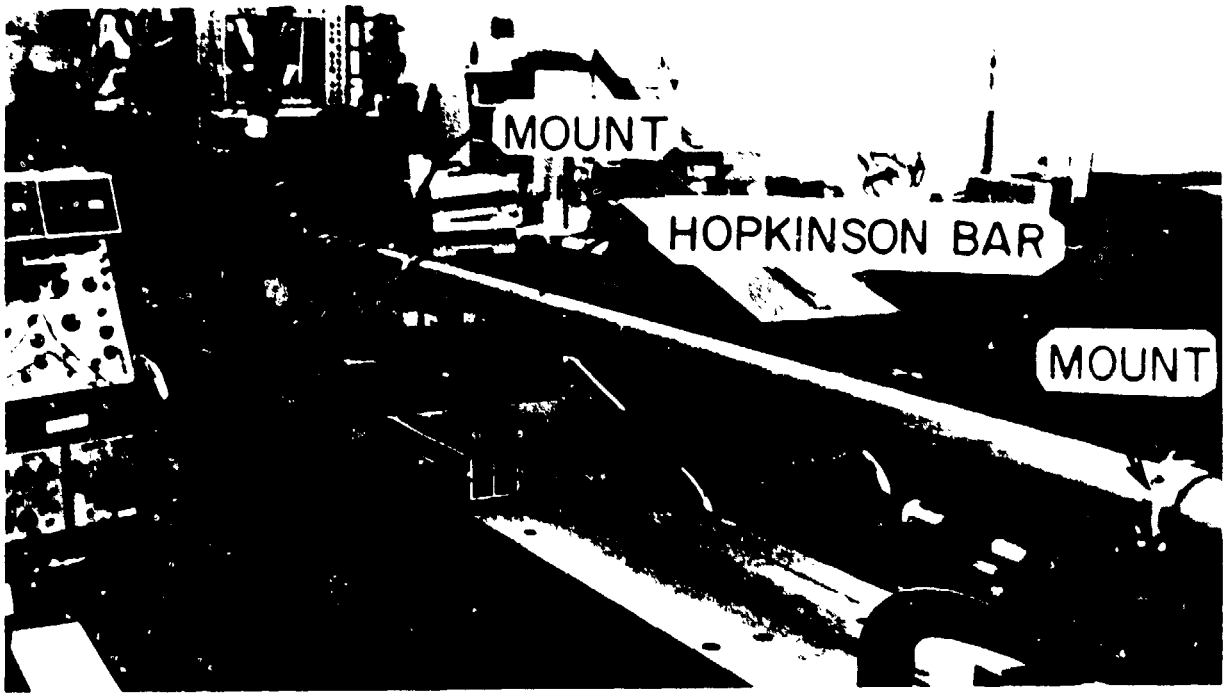

Figure 28. Overall View of the Hopkinson Bar Apparatus.

The bar is 7.6 cm in diameter and 370 cm long. The gages are mounted 76 cm from the impact end. The bar is mounted in Teflon rings to allow for free movement and expansion of the bar. This is necessary to prevent extraneous wave reflections in the bar.

The Hopkinson bar was used in three modes. For normal impact, the end face of the bar was cut at a right angle to the axis of the bar and the projectile trajectory was along the axis of the bar. For oblique impact, the end face of the bar was cut at an angle of 25° and 45° to the axis of the bar and the projectile trajectory was again along the axis of the bar.

c. Data Reduction

Equation 62 was used to obtain the force from the strain measurements. The strain data, recorded with oscilloscopes, was converted to force, digitized, and integrated with time numerically to obtain the total impulse delivered during impact.

3. PRESSURE PLATE

As stated earlier, the response of the Hopkinson bar is limited by geometrical wave dispersion. Thus, the force history recorded using this device is somewhat inaccurate. Also, it is not capable of measuring the distribution of pressure at the impact surface. The obvious method for obtaining this information is to mount pressure transducers on the surface of a rigid plate. A method similar to this was used by such researchers as Bowden and Brunton (Reference 67) and Kinslow, et al. (Reference 39) to measure the pressures generated during the impact of a water jet. However, as seen in the Literature Survey, the results of previous researchers using similar methods of pressure measurement for the impact of water appear to be incorrect. The main source of error was probably insufficient frequency response of the transducers to measure the short duration shock pressures (on the order of a microsecond or less). This problem was compounded by the inability to control the exact size and shape of the projectile.

Both of these problems were overcome in this study by using much larger projectiles with sufficient material strength to hold their shape. The larger diameter and the flat impacting surface of the projectiles resulted in shock durations of 10 μs or greater at the center of impact.

a. AFML Pressure Plate Facility

Figure 29 is a picture of the pressure plate used at the AFML facility.

Figure 29. Pressure Plate Apparatus.

The pressure transducers used for these tests were piezoelectric quartz pressure transducers manufactured by PCB Corporation. The four transducers were mounted flush to the surface and located at the center of impact and 1.27 cm, 2.54 cm, and 3.81 cm from the center. The steel plate, 15.25 cm in diameter and 5.08 cm thick, was mounted as shown in the figure. The transducers are described in a report by Barber, et al. (Reference 65) to a much greater extent.

b. Data Reduction

Several examples of actual pressure traces are shown in the next section. These traces are digitized from the original oscilloscope traces. The amplitudes of the pressures were obtained by multiplying the output voltage of the gage by the gage calibration factor.

The transducers were not originally designed for direct impact testing. This fact resulted in several problems during their use. The gages did not have adequate acceleration compensation. Thus, plate vibrations caused spurious noise to appear in many of the tests results. Secondly, the resonant frequency of the gages was approximately 300 kHz. For the strong shocks which displayed high amplitudes and short rise times, this condition caused resonance to appear in the output of the gages as well as apparent overshoot of the initial pressure pulses. This overshoot is apparent in several of the actual pressure traces displayed in the next section. The accuracy of the shock pressure measurements was also limited by the finite frequency response of the gages (reportedly, 100 kHz) which prevented measurements of rise times of less than 5 μs.

SECTION V

RESULTS AND DISCUSSION

In order to check the applicability of the soft body theory presented earlier, a series of tests were conducted using the Hopkinson bar and the flat plate apparatus. The projectiles for the majority of the tests consisted of birds (chickens) and the bird substitute materials RTV rubber and gelatin. The various material properties used in the theoretical analyses are presented in Appendix C.

All of the projectiles, except the birds, were right circular cylinders. This greatly simplified comparison of theory and experiment. Both the RTV and gelatin were tested with and without porosity in order to see its influence on the pressures generated during impact. Neoprene and beef steak were tested briefly in order to study the effect of material strength and homogeneity. The effects of impact obliquity were studied by conducting tests at three angles, 25°, 45°, and 90° (normal) to the surface of the plate.

1. HOPKINSON BAR TESTS

The assumption that the various soft body projectiles behave as fluids during impact requires that the projectile rebound velocity be negligible. For normal (90°) impacts, this implies that the impulse imparted to the target must be equal to the initial momentum of the projectile, assuming the target is rigid. For oblique impact cases, this implies that the impulse must be equal to the normal component of the initial momentum, that is,

$$I = M u_o \sin \alpha \qquad (63)$$

In order to obtain an accurate measure of the total impulse, various soft body projectiles were impacted against the Hopkinson bar apparatus described previously. Projectile mass, impact velocity, and impact angle were varied for each of the materials tested. The results of these tests are shown in Figures 30, 31, 32, and 33.

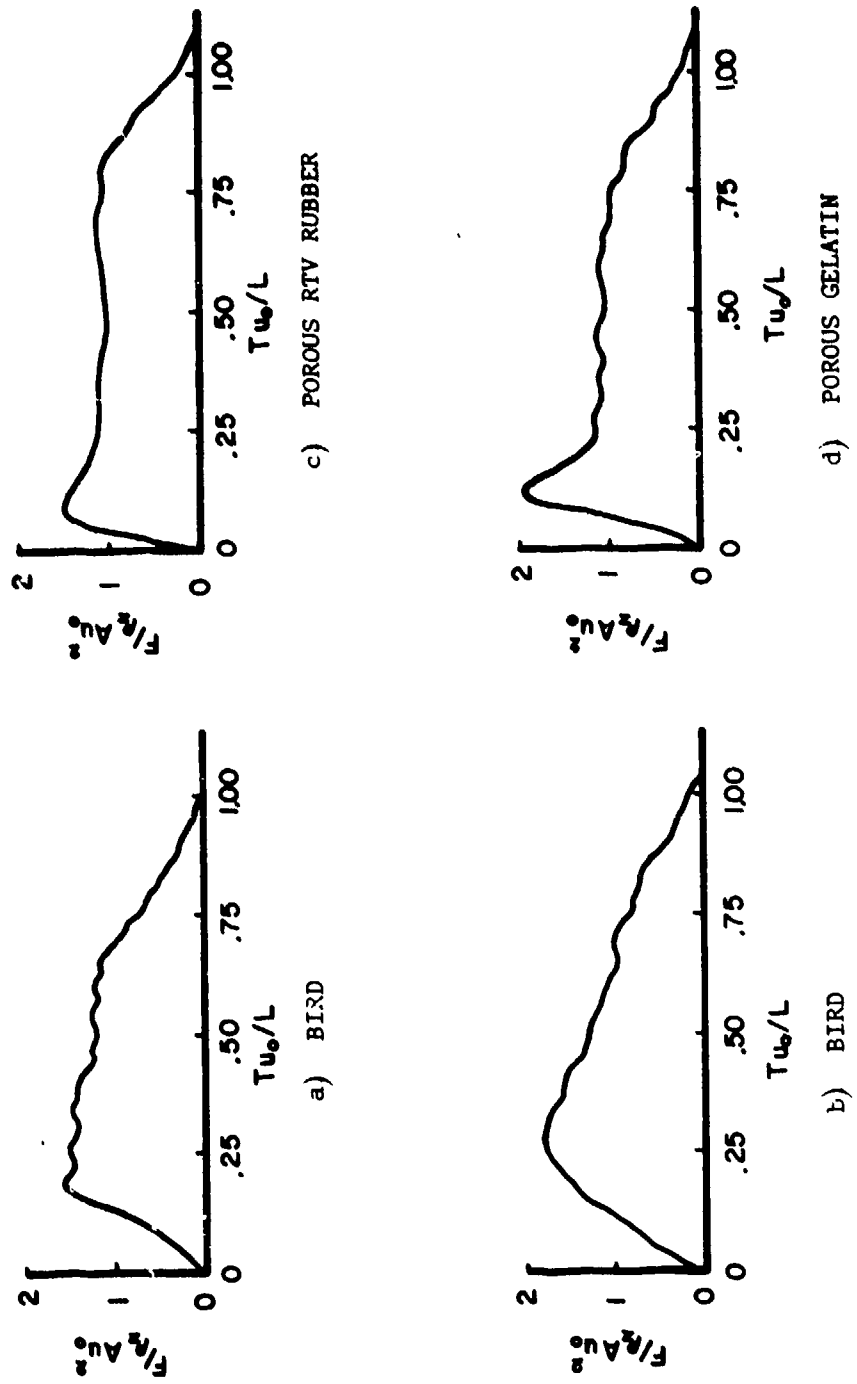

a) BIRD

b) BIRD

c) POROUS RTV RUBBER

d) POROUS GELATIN

Figure 30. Typical Hopkinson Bar Data, Normal Impact.

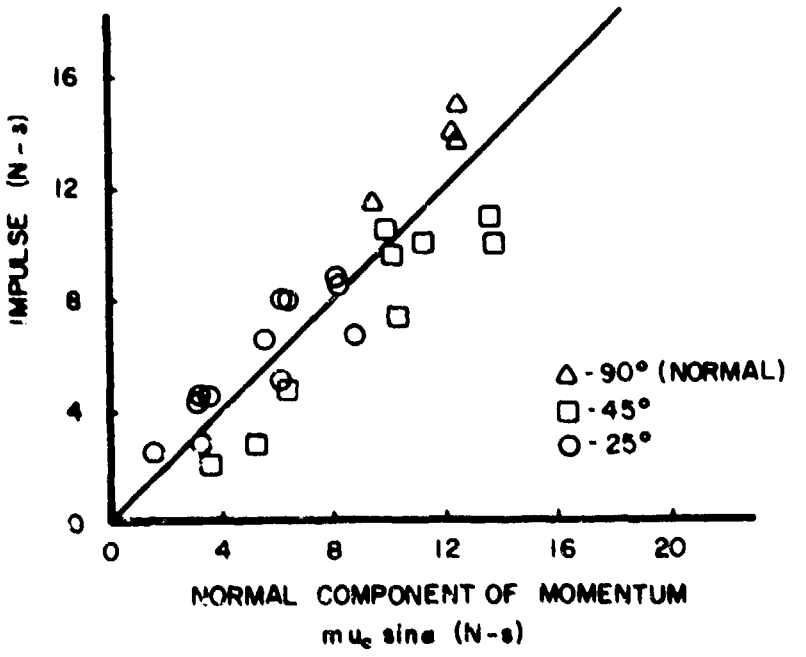

Figure 31. Relationship Between the Normal Component of Momentum and the Impulse Imparted to the Target for the Impact of Porous RTV.

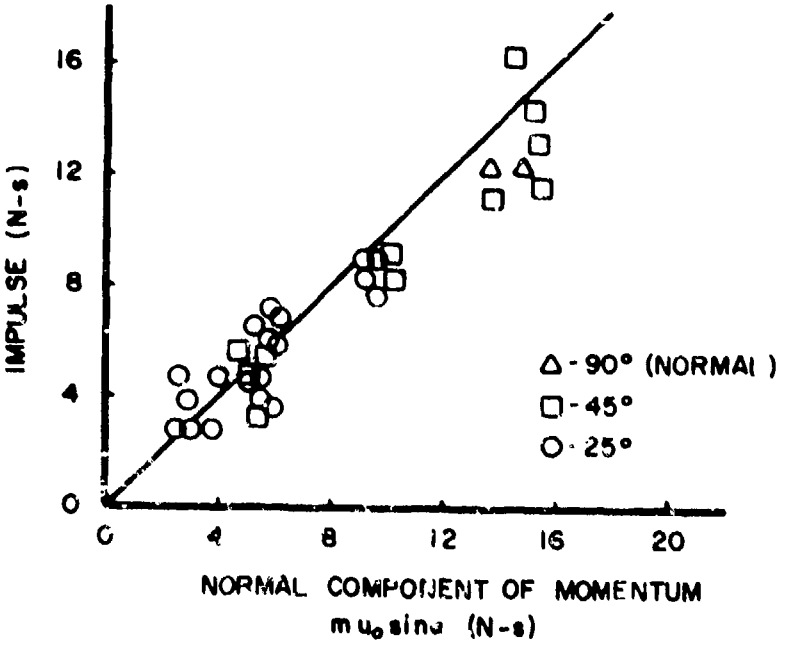

Figure 32. Relationship Between the Normal Component of Momentum and the Impulse Imparted to the Target for the Impact of Porous Gelatin.

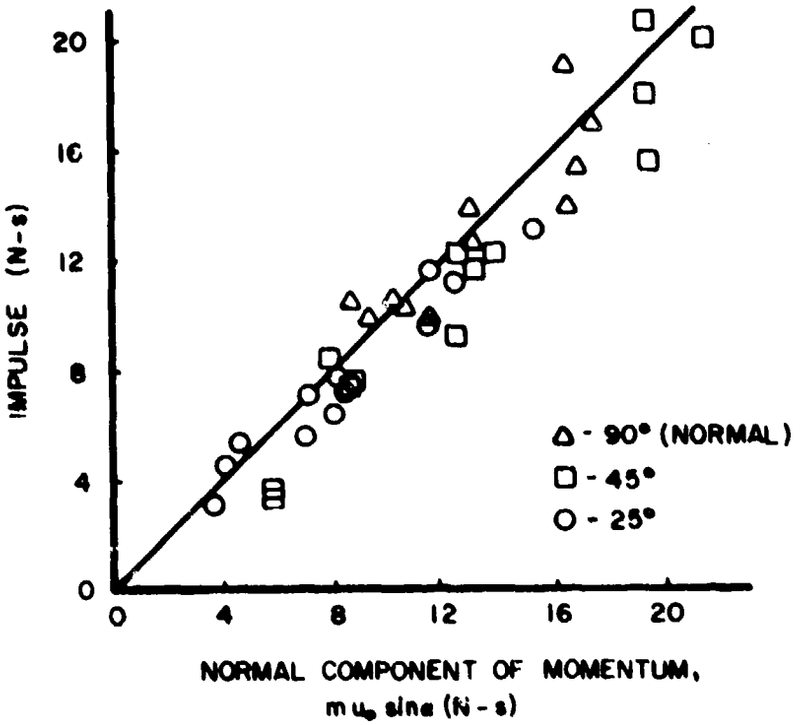

Figure 33. Relationship Between the Normal Component of Momentum and the Impulse Imparted to the Target for the Impact of Birds.

Figure 30 presents examples of the measured force histories from which the impulse measurements were obtained by integration. These are only approximate force histories since the Hopkinson bar effectively filters the higher frequency components. The impulse measurements are compared with the normal component of momentum in Figures 31, 32, and 33 for porous RTV, porous (micro-balloon) gelatin, and birds. From each of these figures, it is apparent that there is no significant deviation from the relationship given by Equation 63 for each of the materials tested.

2. PRESSURE PLATE TESTS

a. Normal Impact

The fluid model of soft body impacts against a rigid target, presented earlier, has several characteristic features. For the impact of a cylindrical projectile the pressure history at the projectile-target interface is divided into three distinct phases; the shock, the release,

and steady flow. For normal impact, the initial Hugoniot shock pressure is given by Equation 4, $P_H = \rho_o u_s u_o$, and has a duration at the center of impact given by Equation 7, $t_B = a/c_p$. During the release phase, radial flow is established. Because of the complicated release process, no analytical expressions have been derived for this phase. However, once flow is completely established, steady flow relations hold. The pressure at the stagnation point, P_s, located at the center for normal impact, is derived from Bernoulli's Equation and takes the form of Equation 16,

$$\int_{P_o}^{P_s + P_o} \frac{dP}{\rho} = \frac{u_o^2}{2}$$

and the pressure distribution across the surface may be approximated by Equation 27,

$$P = P_s \{1-3 (\frac{r}{\zeta_2 a})^2 + 2(\frac{r}{\zeta_2 a})^3\}$$

The duration of the entire impact process may be approximated by the time that it takes for the projectile to flow through itself, given by Equation 21, $t_D = L/u_o$.

In order to experimentally determine the pressure histories for various soft body impacts, the pressure plate apparatus described previously was used. All of the projectiles, except the birds, were right circular cylinders, with length-to-diameter ratios of approximately two. During this testing program, the size, mass, density, and porosity of the projectile were varied as well as the impact velocity and impact angle.

Typical pressure histories recorded at the center of impact for the various soft body materials are presented in Figure 34. Here the pressure measured with the center transducer (stagnation point) and the time are plotted in the nondimensionalized form, obtained by dividing the pressure by $P = 1/2\ \rho_z u_o^2$ (the steady-flow stagnation pressure for an incompressible fluid) and the time by $t_D = L/u_o$ (the theoretical duration of impact). ρ_z, the average density of the porous material was defined

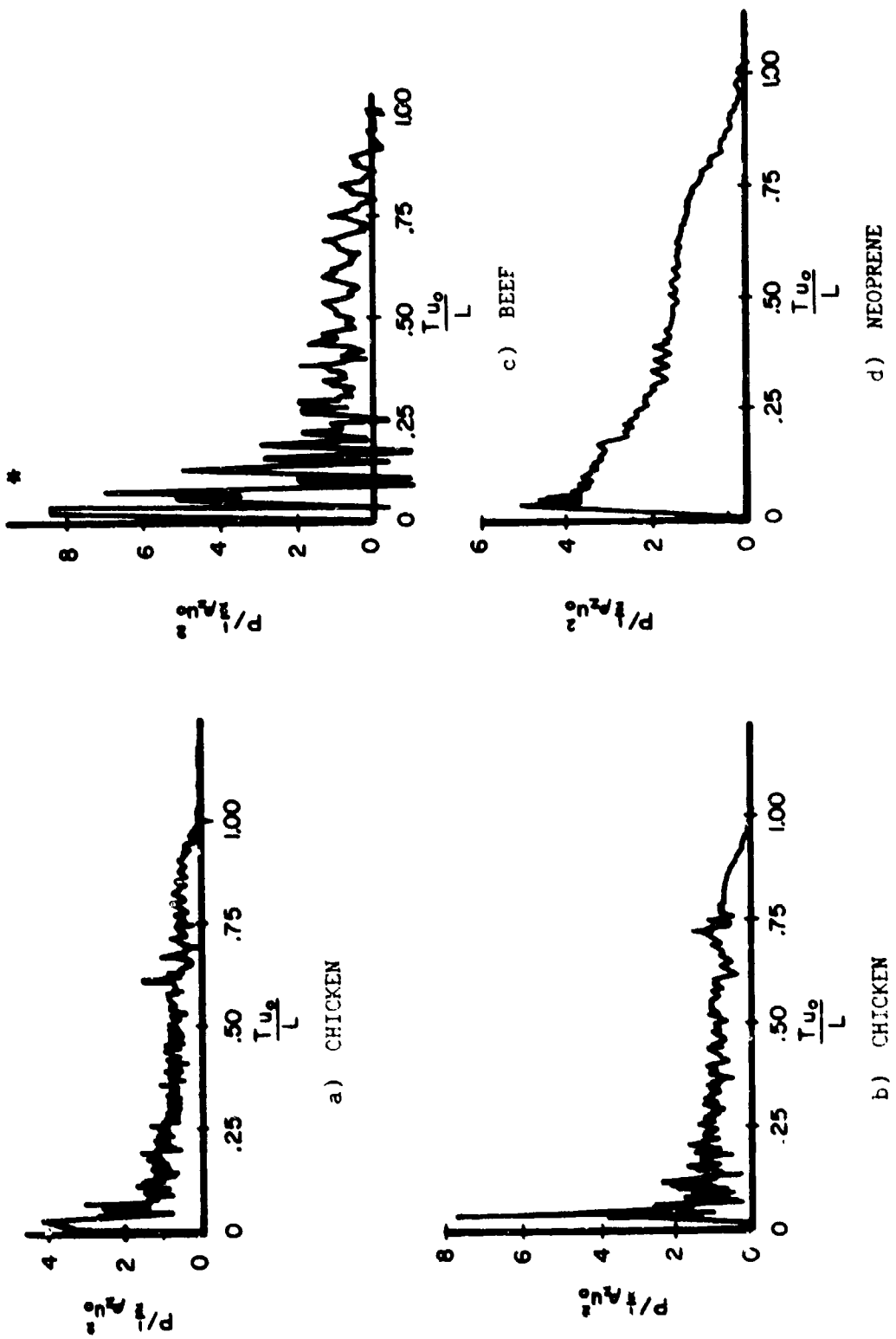

Figure 34. Typical Pressure Plate Data, Normal Impact.

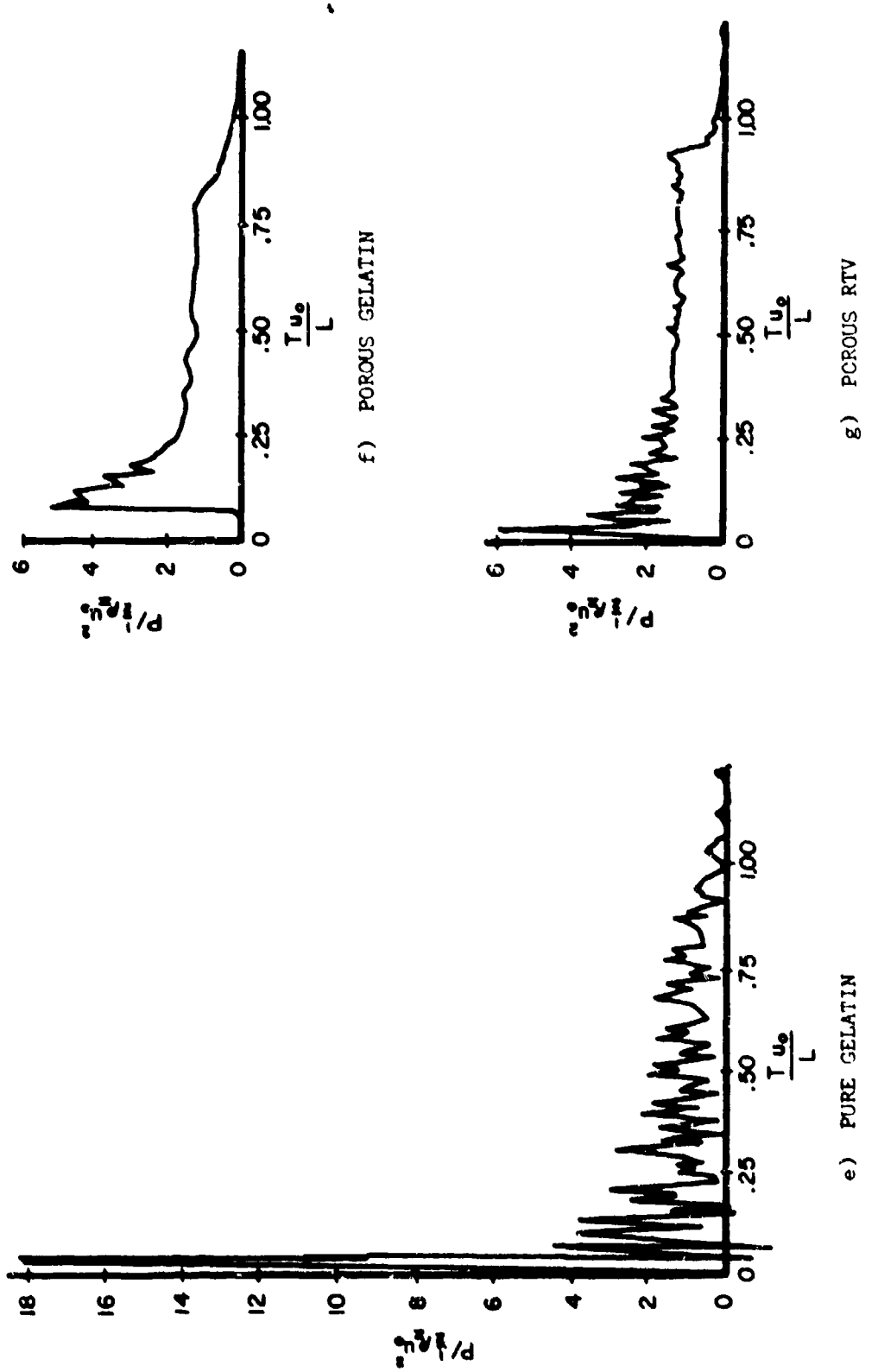

Figure 34. Typical Pressure Plate Data, Normal Impact (Continued)

in Equation 58. The impact velocity for each of these tests was approximately 200 m/s. The similarities of the pressure histories for the various materials are evident. Each shows the expected fluid characteristics; namely, an initial peak pressure followed by a decay to a lower flow pressure, with a total duration of approximately $t_D = L/u_o$. Of course, the exact shape of the pressure histories varies for each material due to differences in material properties.

The peak pressure is seen to be greatest for the pure gelatin, due to its high shock velocity and lack of porosity. Each of the other materials, with the exception of neoprene, had certain amounts of porosity which greatly decreased their shock velocities, hence their shock pressures. Neoprene, even with zero porosity, has a very low shock velocity. On some of the bird shots the pressure did not rise immediately to a peak. This was due to the impact of such things as the bird's feet or feathers prior to impact by its main body.

For each of these materials, an apparent steady flow region exists and it is most readily seen in the pressure history of porous RTV. Each of the other materials displayed a tendency for the pressure to slowly decay in this flow regime. This decay from steady flow, most obvious for the beef and pure gelatin, was described in the theory as being the unsteady flow effects due to the finite length of the projectile. As stated in the theoretical section, this effect should be greatest for subsonic impacts such as those of the beef and gelatin. It should be least apparent for supersonic impacts such as for the porous RTV and micro-balloon (porous) gelatin.

Since pure gelatin is almost incompressible at this impact velocity, its stagnation pressure is seen to be approximately $1/2\ \rho_z u_o^2$. Each of the other materials showed varying degrees of compressibility, evidenced by the fact that in the steady flow regime, their nondimensionalized pressures had values greater than one.

One of the major features distinguishing the pressure histories of birds from that of porous RTV and micro-balloon gelatin is the much larger amount of high-frequency "noise" superimposed on the pressure

profile of birds. Initial inquiries into the source of this noise were fruitless. In order to see if it was caused by the bone structure of the bird, a beef projectile was constructed and tested. As can be seen, the noise was even greater for the beef than for the birds. Thus, the effect of the bone structure was assumed negligible. Another thought was that the noise might have been caused by the break-up or tearing of the material (creation of new surfaces) during impact. This theory seemed resonable since both the birds and the beef consisted of muscle fibers which would require more energy to tear than would the RTV or gelatin. Along this line of thought, neoprene was tested since it bounces at velocities of 200 m/s and there is no resulting material break-up. Accordingly, the pressure history of the neoprene impact showed no noise except that due to acceleration loads on the gages caused by the pressure plate vibrations. Thus, there appears to be a direct correlation between the amount of energy expended in material break-up and the amount of high-frequency noise recorded. (The extreme amount of noise recorded during the impact of pure gelatin was apparently due to excitation of the gage near its resonant frequency).

A point of interest noted during this testing program was the fact that the neoprene's pressure history was somewhat similar to that of the other materials even though it did not "flow" at impact velocities as high as 200 m/s. This was noted for porous RTV and micro-balloon gelatin which bounced at impact velocities of 100 m/s. This would seem to imply that the basic fluid flow theory presented in this report holds even for materials which do not flow (or shatter) during impact but which do undergo large amount of deformation (strain).

A closer comparison of the pressure histories for the impact of birds and the two bird substitute materials, porous RTV and micro-balloon gelatin, can be obtained from Figures 35, 36, and 37. In these figures, typical pressure histories at the center of impact are shown for various impact velocities. In each figure a short line representing the predicted shock pressure amplitude, P_H, and duration, t_B, is shown as well as a long line representing the predicted amplitude of the steady flow pressure at the stagnation point, P_s. The pressure and time are again presented in nondimensionalized form.

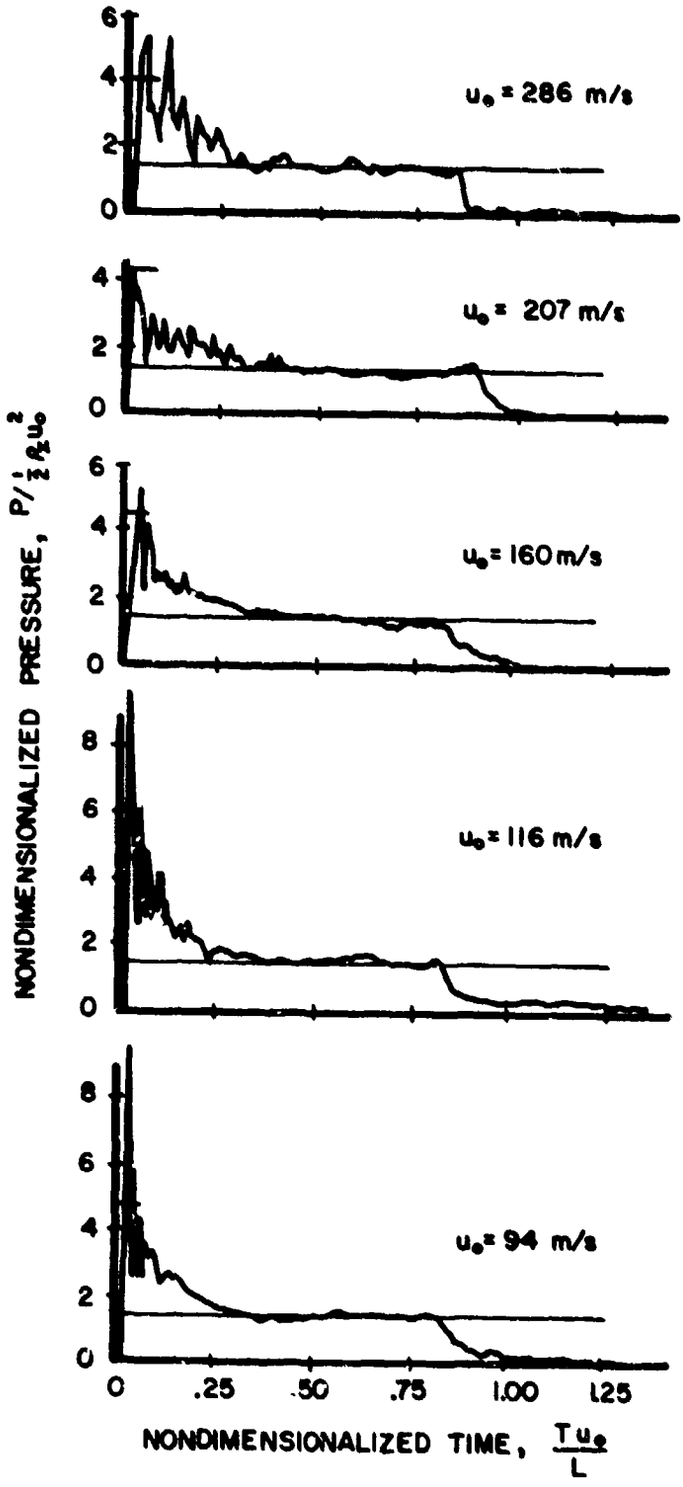

Figure 35. Typical Pressure Data at Various Impact Velocities for Porous RTV, Normal Impact.

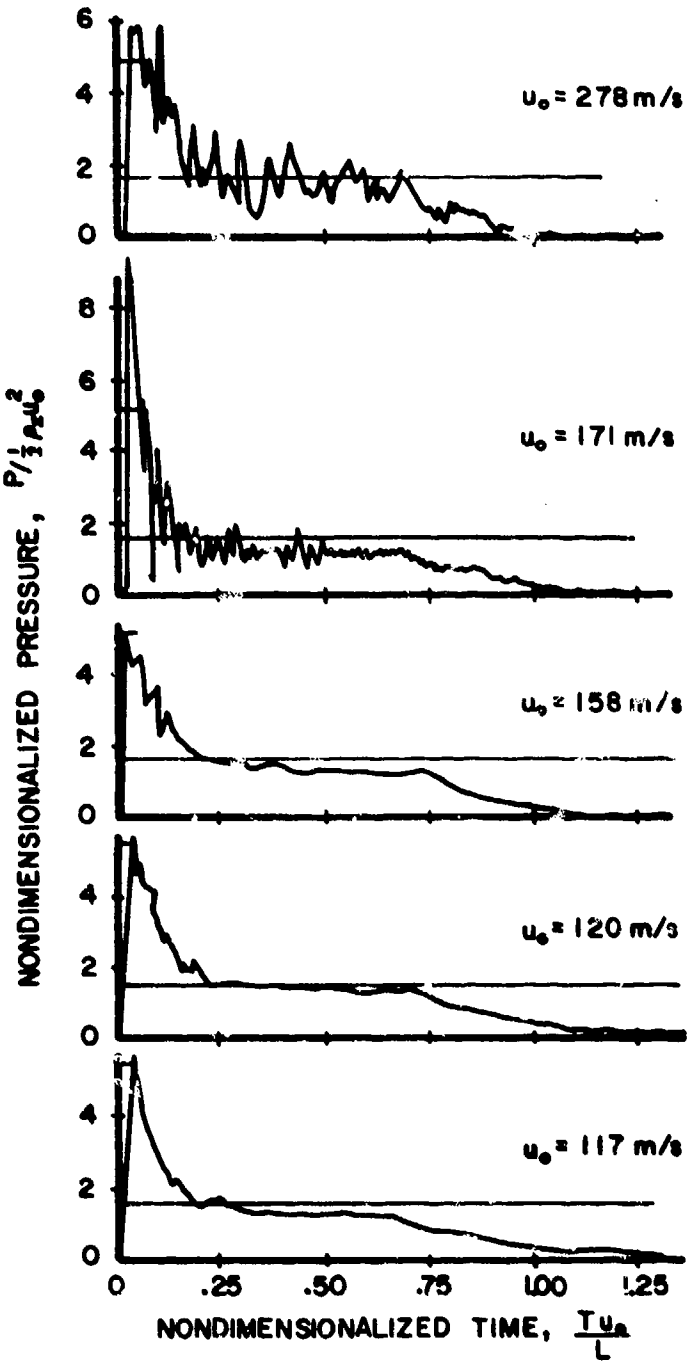

Figure 36. Typical Pressure Data at Various Impact Velocities for Porous Gelatin, Normal Impact.

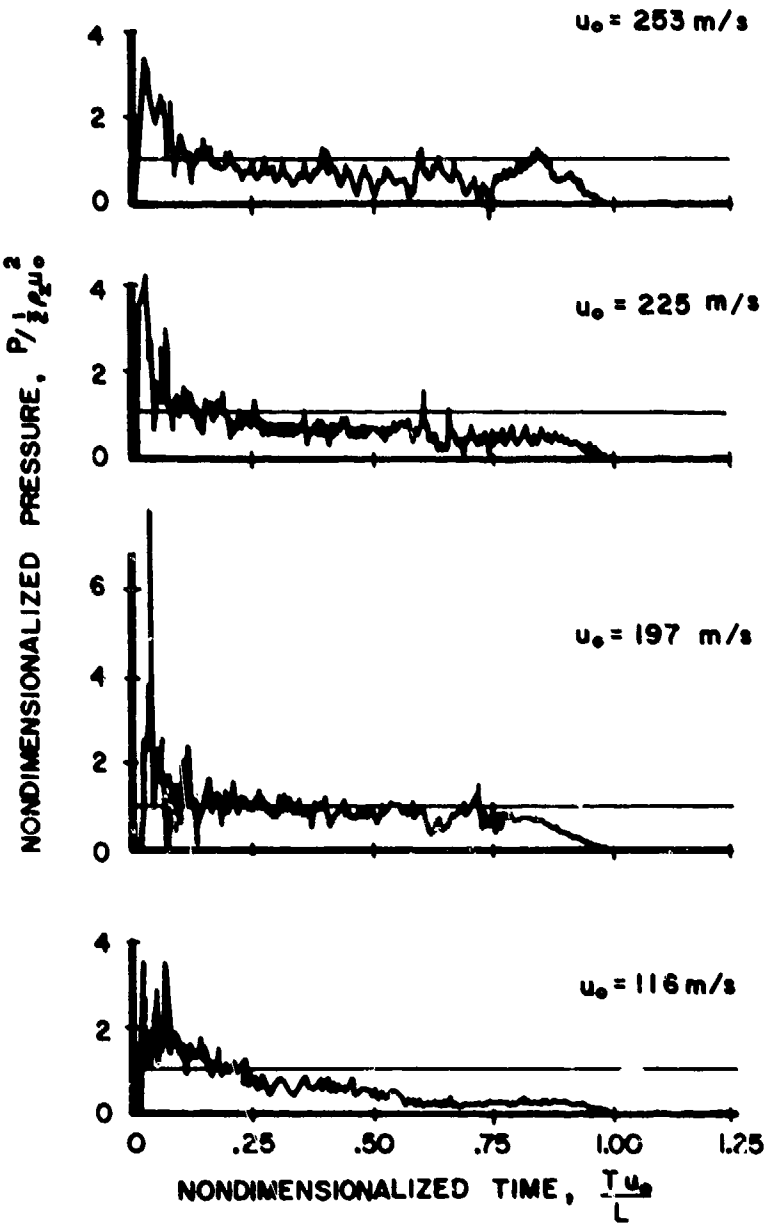

Figure 37. Typical Pressure Data at Various Impact Velocities for Birds, Normal Impact.

The calculated amplitude and duration of the shock pressures agree well with the measurements for the two bird substitute materials, although some transducer resonant excitation and resultant overshoot is seen on several shots. Discrepancies between theory and measurements for birds should be expected due to the rounded geometry and irregular surface of the bird and the prior impact of su· ·hings as feathers, wings, and legs.

As was stated earlier, each of the materials seems to display a regime of steady flow during which the measured pressure agrees with the calculated stagnation pressure. The deviations in the pressure histories for the micro-balloon gelatin at high velocity may have been due to geometric distortion of the projectile during launch or to resonant excitation.

In order to demonstrate the radial variation of pressure, Figure 38 presents a typical porous RTV impact in which the pressure histories at three transducer locations are shown. The peak pressure appears to be less at the transducer located at 0.6 r/a than at the center since the duration of the shock pressure at this point is so short that the transducer could not respond rapidly enough to record it. Of course, there was no shock at the transducer located outside the initial impact area of the projectile. This figure also demonstrates the radial decrease in pressure in the steady flow regime.

Figure 39 shows a typical pressure history for porous RTV recorded along the major axis of an oblique impact of 45°. Lines are drawn in each figure representing the calculated shock pressure, and full, steady-flow stagnation pressure. The predicted shock durations are not shown in these figures. As explained in the theory, the shock pressure for an impact velocity u_o and an impact angle α should be identical to that produced by a normal impact with an initial velocity of $u_o \sin \alpha$. From Equation 36, the 45° impact angle is seen to be very near the critical angle for RTV. This implies that the full shock pressure may exist over the entire impact surface and that the duration of the shock near the center of impact should be sufficient for the pressure gages to record the full shock pressure. Also, expected from

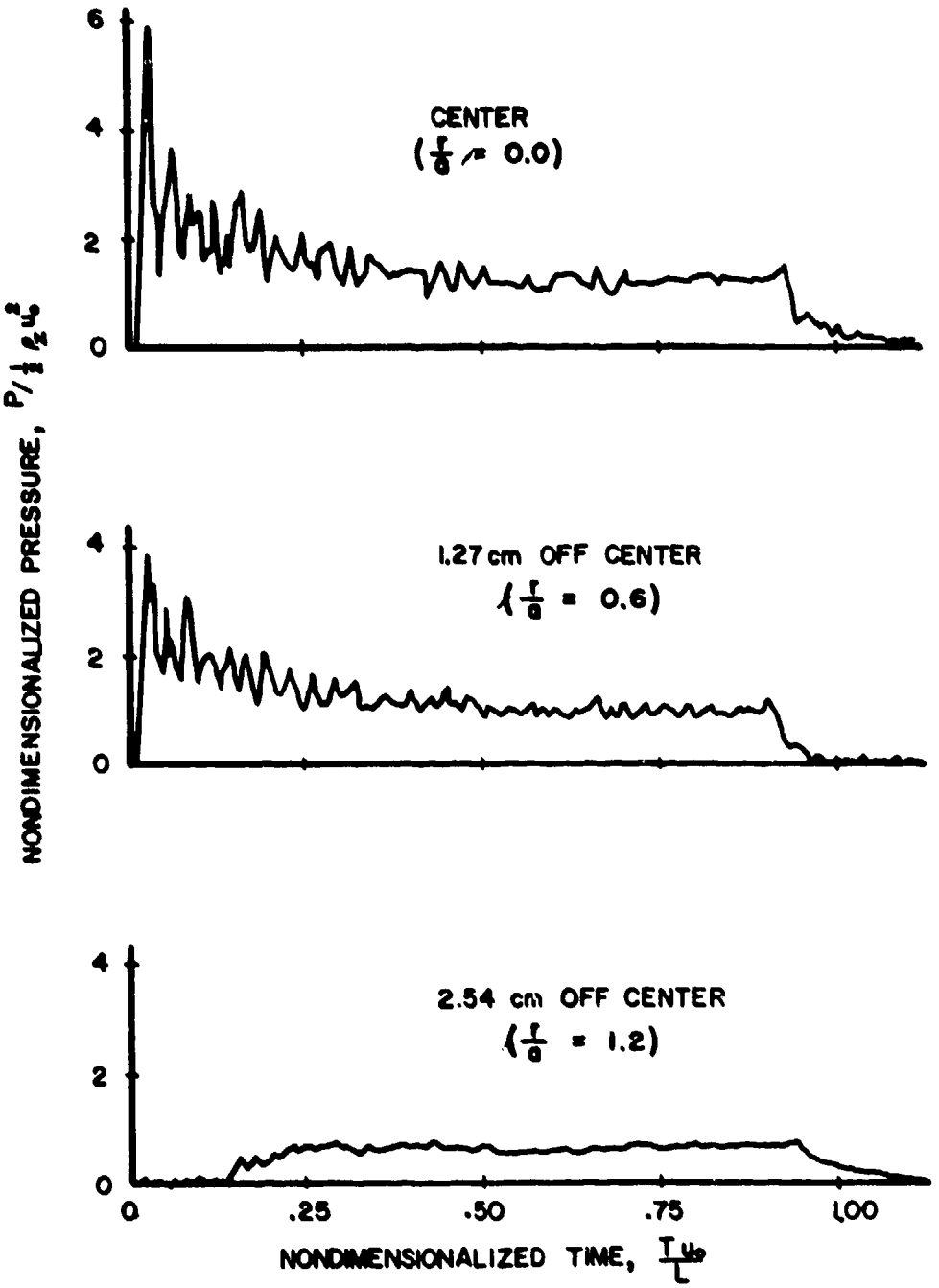

Figure 38. Typical Distribution of Pressure Plate Data for the Impact of Porous RTV, Normal Impact.

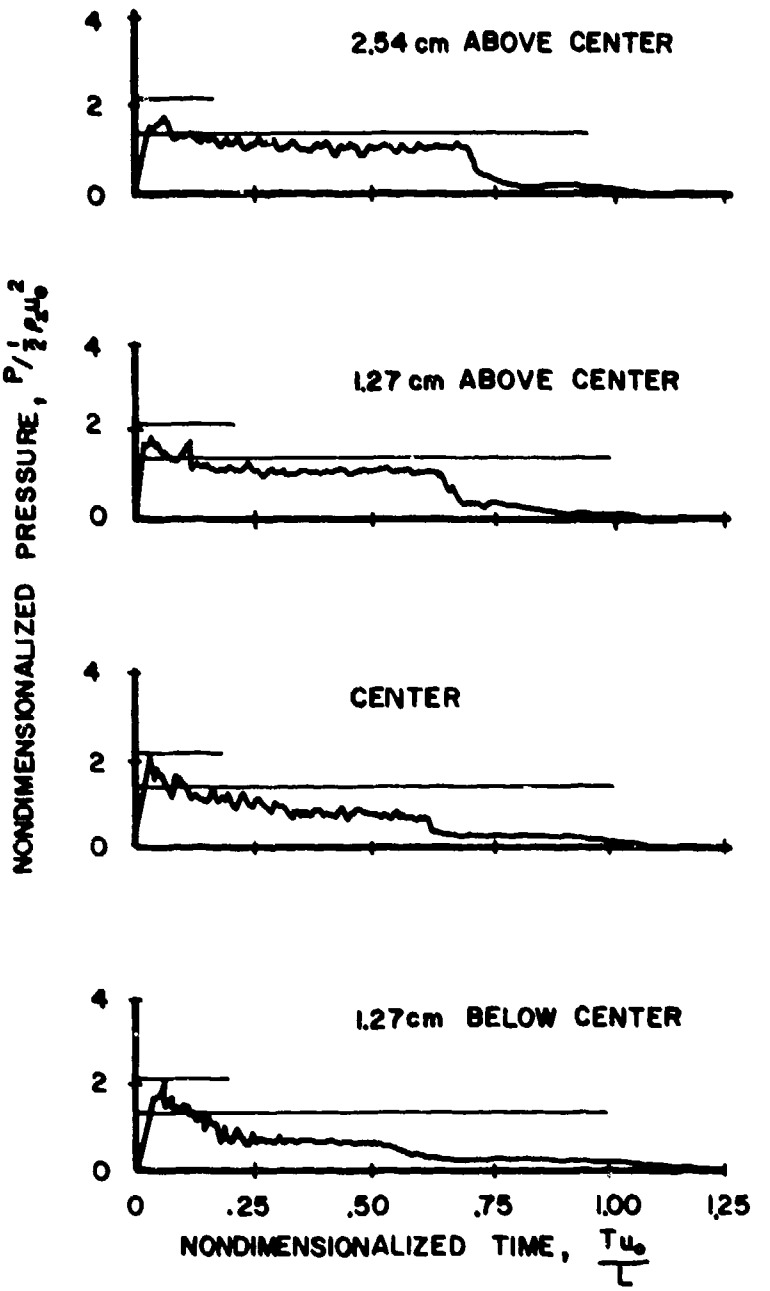

Figure 39. Typical Distribution of Pressure Plate Data for the Impact of Porous RTV, Oblique Impact (α = 45°).

the theory is the fact that the stagnation point, which is approximately 3 cm above the center transducer, should "see" the full stagnation pressure during steady-flow, regardless of the angle of impact.

From the figure, several of these points are clear. The shock pressure at the center gage is the full shock pressure, and the other gages record peak pressures near this value. The steady-flow pressure is also seen to be highest at the gage 2.54 cm above center. The fact that the pressure here is somewhat below the stagnation pressure implies that this gage was not located exactly at the stagnation point. It should be noted that for much smaller angles of impact (greater impact obliquity) the amplitude of the calculated shock pressure will be less than the steady-flow stagnation pressure for RTV.

In Figures 34-39, typical pressure histories for the various materials were presented in order to demonstrate a qualitative understanding of the pressures generated during soft body impact. However, in order to compare the fluid theory with the soft body impact experiments, a more quantitative presentation of the pressure data is required. In this section, the experimental results are compared with theoretical predictions for the various materials.

The variation of shock pressure with impact velocity for normal impact is given in Figures 40, 41, and 42 for porous RTV, micro-balloon gelatin, and birds, respectively. In Figure 40, the theoretical Hugoniot shock pressure is given for both pure ($z = 0.00$) and porous ($z = 0.50$) RTV. Experimental measurements for the porous RTV tend to be higher than that predicted. However, as stated previously, it appears in Figure 36 that the high peak pressures may have been due to some transducer overshoot. In fact, the pressures tended to oscillate about the predicted shock pressures. In Figure 41, the theoretical Hugoniot shock pressure is given for pure ($z = 0.00$) and porous ($z = 0.40$) gelatin. Experimental measurements for the impact of the micro-balloon gelatin are shown to agree very closely with the predictions.

In Figure 42, the theoretical Hugoniot shock pressure is given for birds. As stated in Appendix C, this curve is based on the assumption

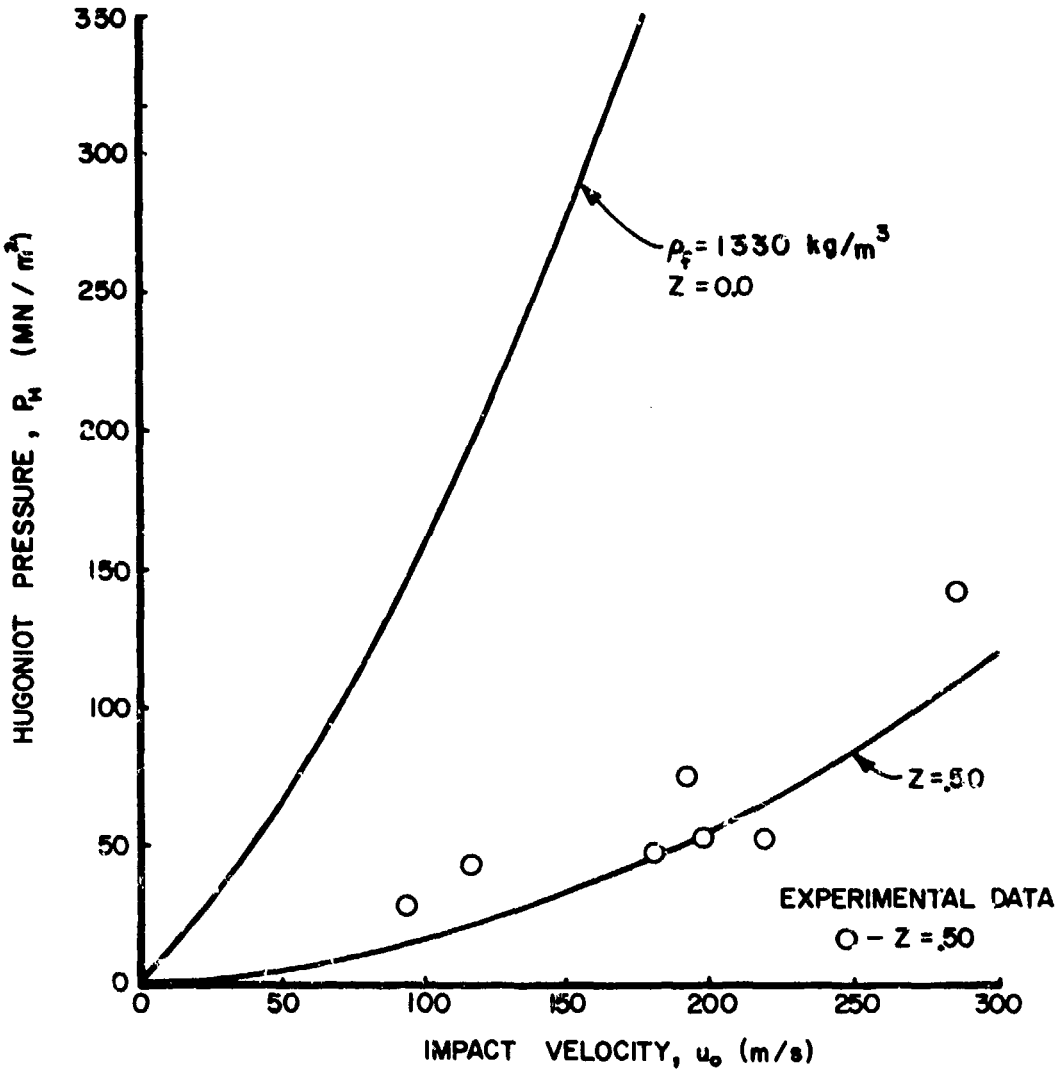

Figure 40. Hugoniot Shock Pressures Measured During Normal Impact of Porous RTV. (1 MN/m^2 = 10 Bars, 10^3 kg/m^3 = .036 lb/in^3).

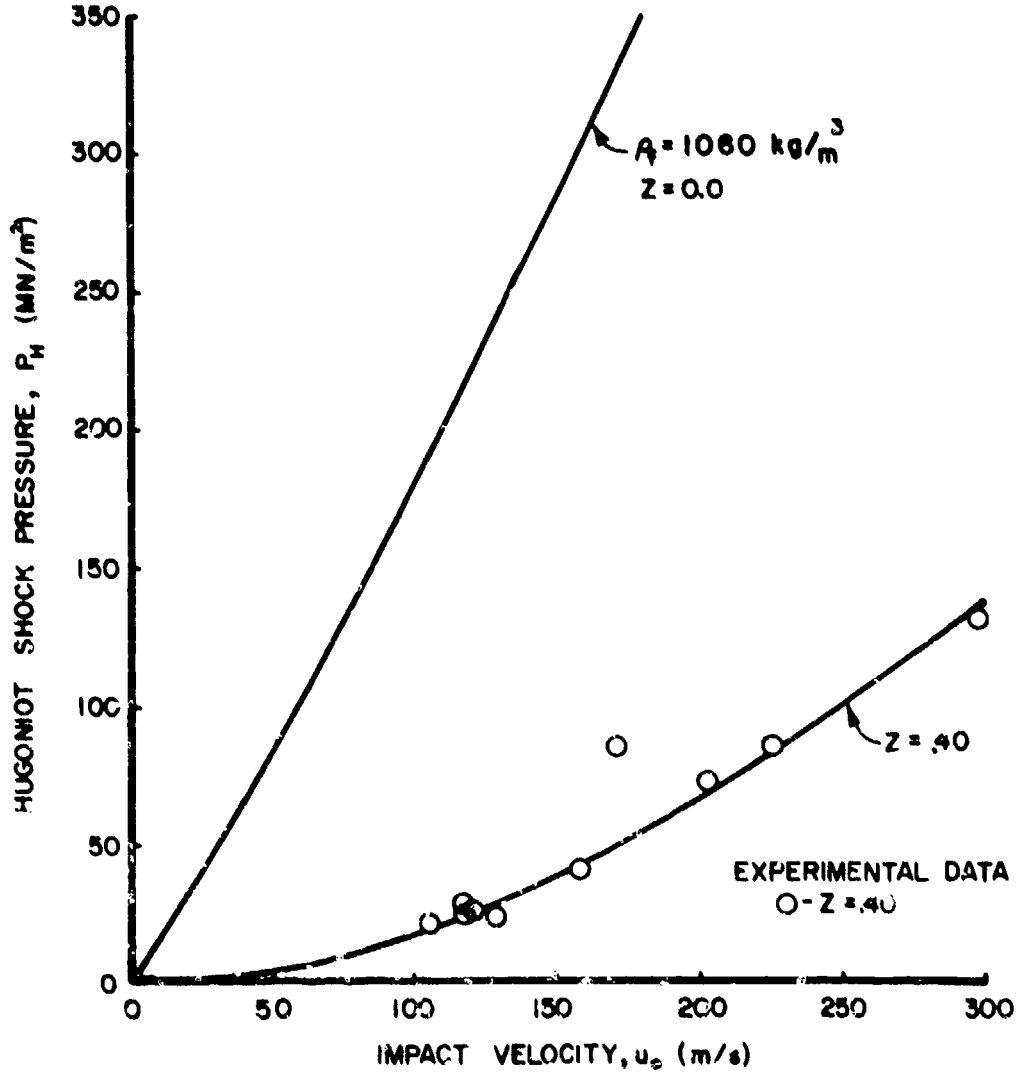

Figure 41. Hugoniot Shock Pressures Measured During Normal Impact of Porous Gelatin. (1 MN/m^2 = 10 Bars, 10^3 kg/m^3 = .036 lb/in^3).

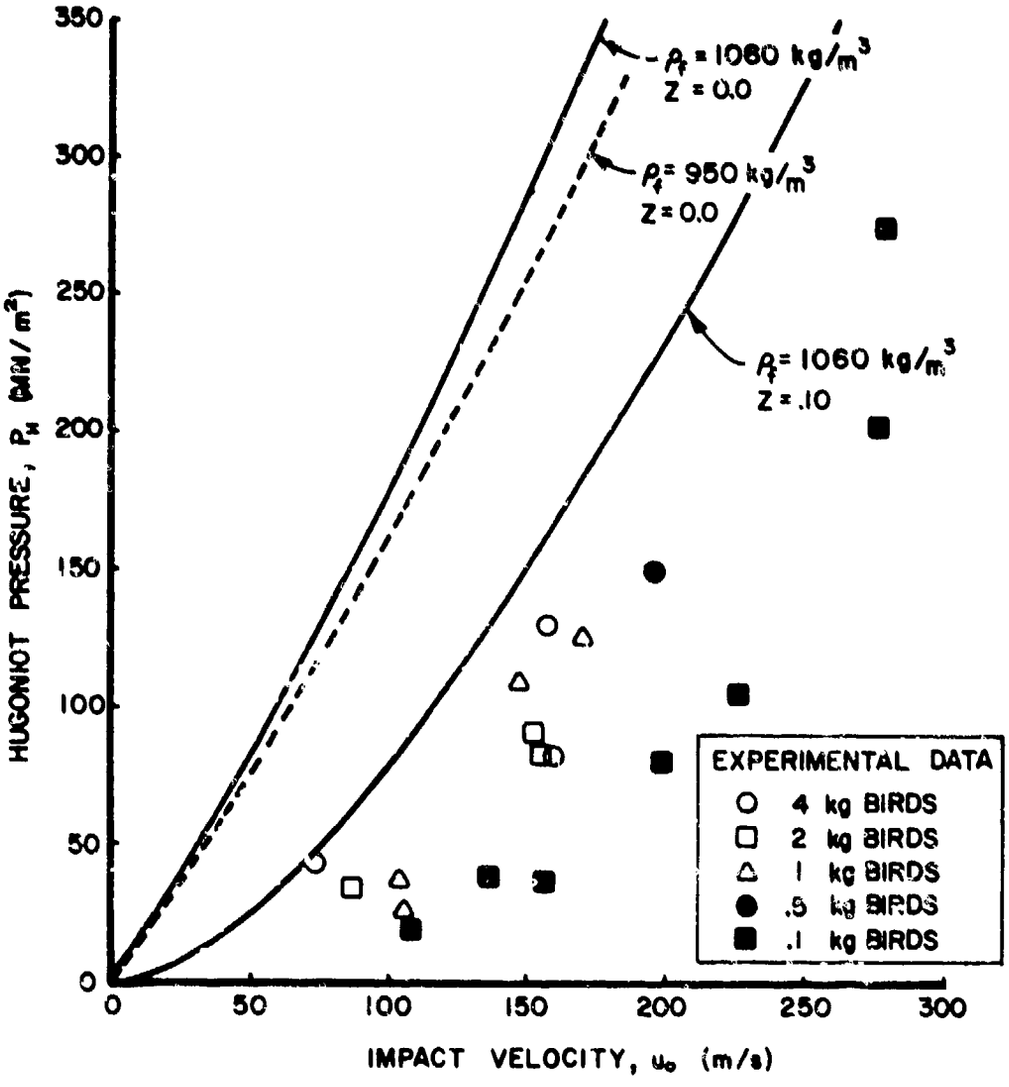

Figure 42. Hugoniot Shock Pressures Measured During Normal Impact of Birds. (1 MN/m^2 = 10 Bars, 10^3 kg/m^3 = .036 lb/in^3).

that the Hugoniot relationship for birds is similar to that for water (or gelatin) with an assumed pure density of ρ_f = 1060 kg/m^3 and a porosity of z = 0.10 (average density ρ_z = 950 kg/m^3). The data shown here were obtained from tests conducted on small birds at AFML and on large birds at AEDC (Reference 66). The measured peak pressures fall below that predicted. The fact that the peak pressure tended to increase with bird mass, hence with bird size, implies that the low peak pressure measurements may be due to the lack of planar impact for birds. As shown in the theoretical section, the duration of the full shock pressure is a function of the radius of curvature of the impacting surface, so that the shock duration at the center of impact is much less for a projectile with a rounded end than for a right circular cylinder. For small birds with an irregular impact surface and a small radius of curvature, the shock duration was probably so small that the transducers could not respond rapidly enough to record the shock pressure. For larger birds with larger radii of curvature, the duration of the shock was greater. The peak pressures measured on several of the 4 kg bird tests approached the predicted values. Other reasons for the low peak pressures include the existence of material such as feathers and legs which impacted prior to the main body and the existence of lower impedance material at the surface of the main body.

The variation of pressures in the steady flow regime with impact velocity is presented in Figures 43, 44, and 45. The pressure at the center stagnation point is plotted for RTV in Figure 43. Theoretical predictions are given for pure and porous RTV using the compressible fluid theory. A curve of $P = 1/2\ \rho_z u_o^2$ (incompressible fluid theory, ρ_z = 670 kg/m^3) is also presented for comparison. The measured stagnation pressures for porous RTV agree very closely with those predicted by the compressible theory.

In Figure 44, the steady-flow, stagnation pressure is given for both pure gelatin and micro-balloon gelatin impact tests. Theoretical curves from compressible theory are shown as well as the plot of $P = 1/2\ \rho_z u_o^2$ (ρ_z = 640 kg/m^3). The experimental data is seen to agree very nicely with the compressible theory for both types of gelatin.

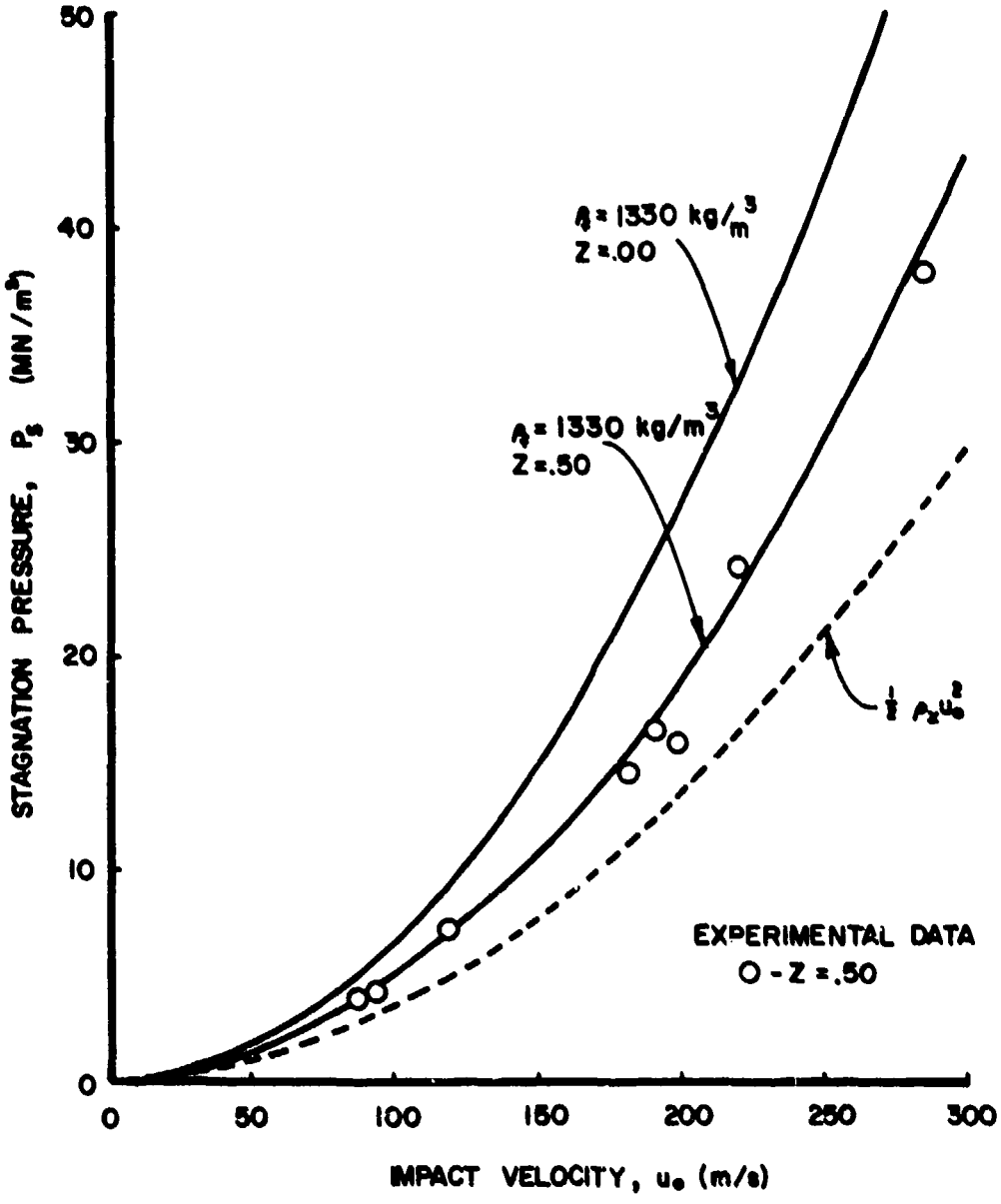

Figure 43. Steady Flow Pressures Measured at the Center of Impact During Normal Impact of Porous RTV. (1 MN/m^2 = 10 Bars, 10^3 kg/m^3 = .036 lb/in^3).

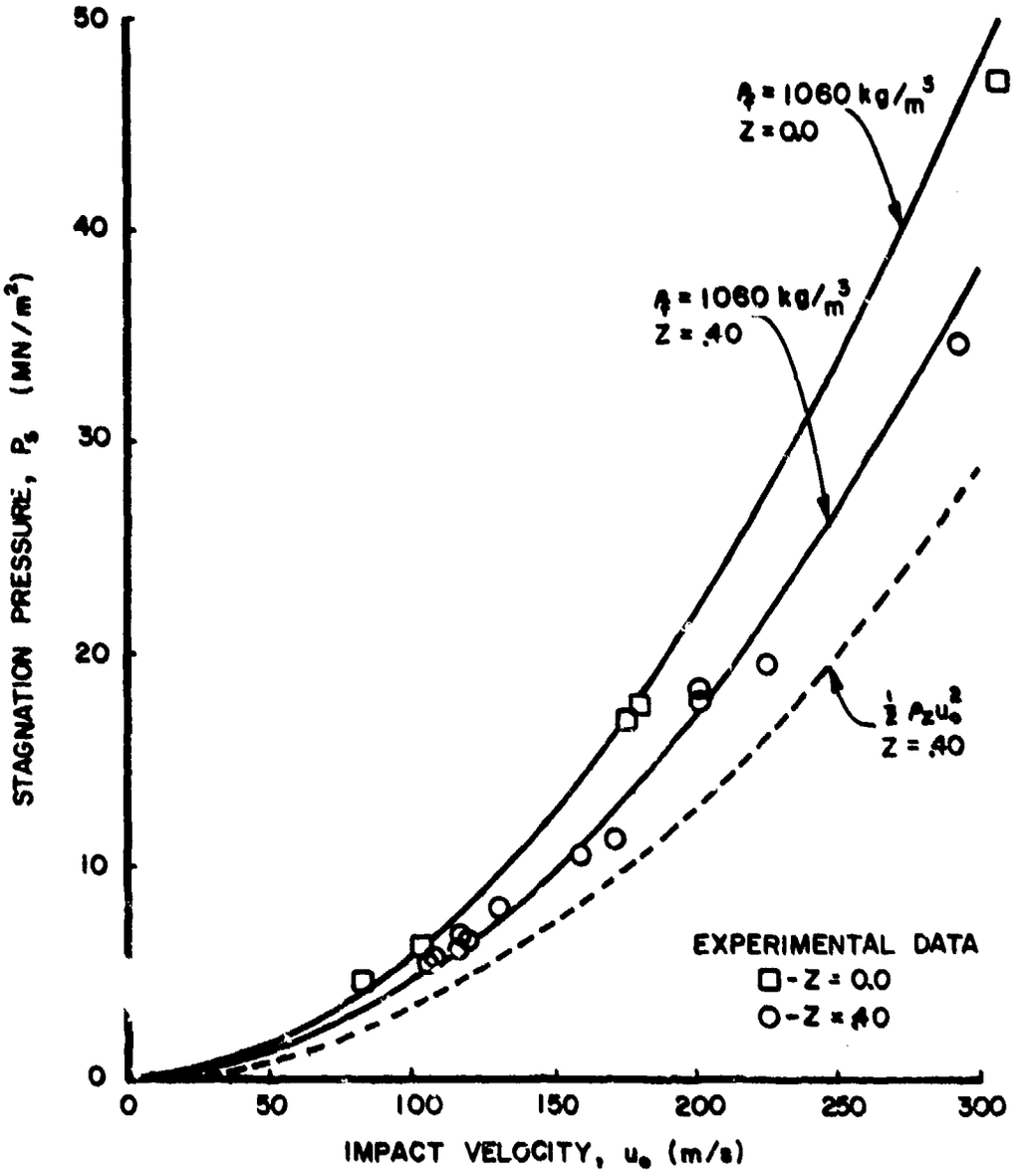

Figure 44. Steady Flow Pressures Measured at the Center of Impact During Normal Impact of Porous Gelatin. .(1 MN/m^2 = 10 Bars, 10^3 kg/m^3 = .036 lb/in^3).

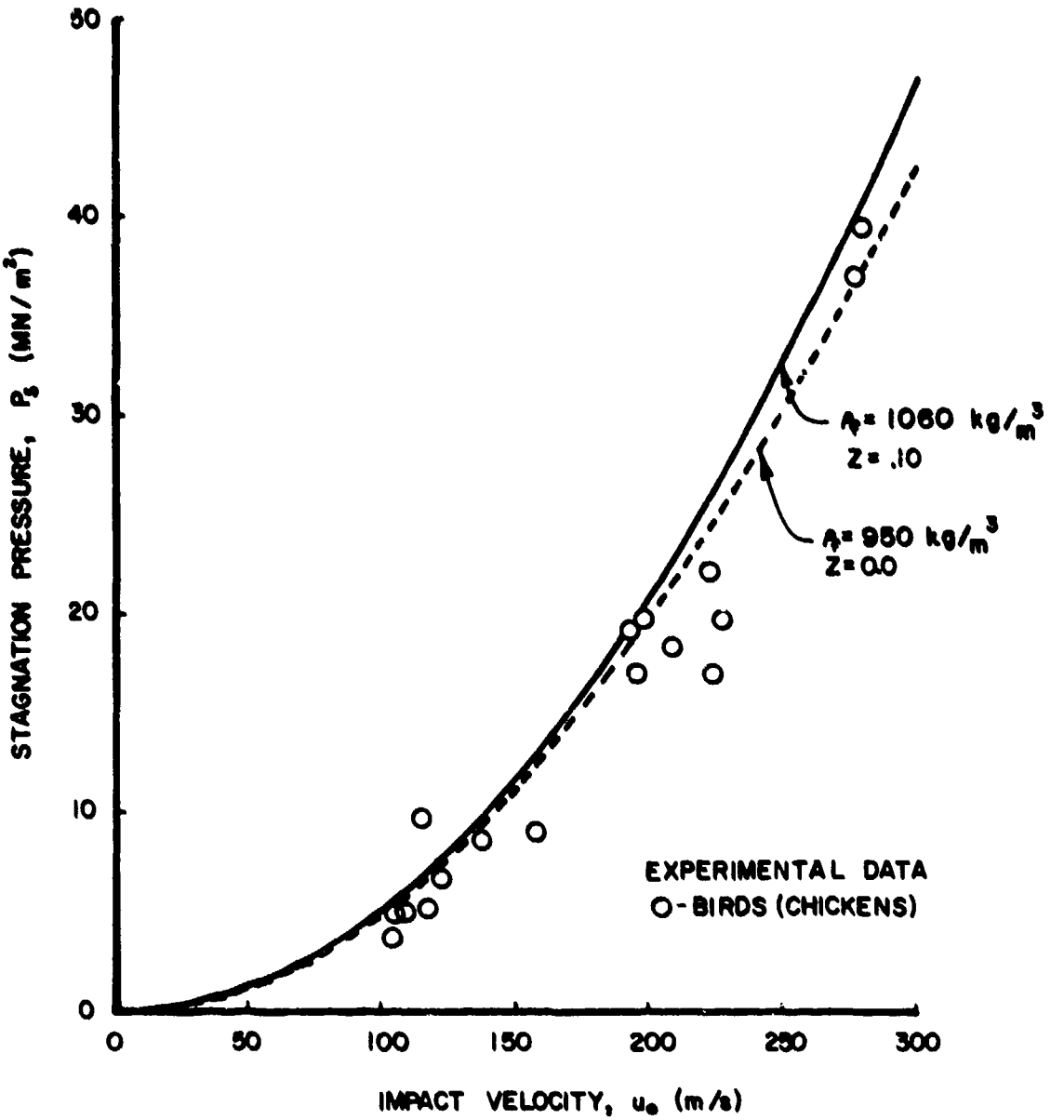

Figure 45. Steady Flow Pressures Measured at the Center of Impact During Normal Impact of Birds. (1 MN/m² = 10 Bars, 10^3 kg/m³ = .036 lb/in³).

In Figure 45, the stagnation pressure is given for the impact of birds. A theoretical prediction is made assuming ρ_f = 1060 kg/m^3 and z = 0.10 and ρ_f = 950 kg/m^3 and z = 0.0. As shown earlier in Figure 35 for the impact of birds, end effects in the bird causes a gradual decrease in flow pressure, making measurement of the steady flow pressure difficult. However, the measured data does appear to be in fair agreement with the theoretical curve based on the compressible flow theory, although there is more scatter in the data than seen previously for the RTV and gelatin.

Figures 46, 47, 48, and 49 show the variation of pressure in the steady flow regime with radial distance from the center. The pressure is again nondimensionalized and the radial distance is nondimensionalized with respect to the initial radius of the projectile, a.

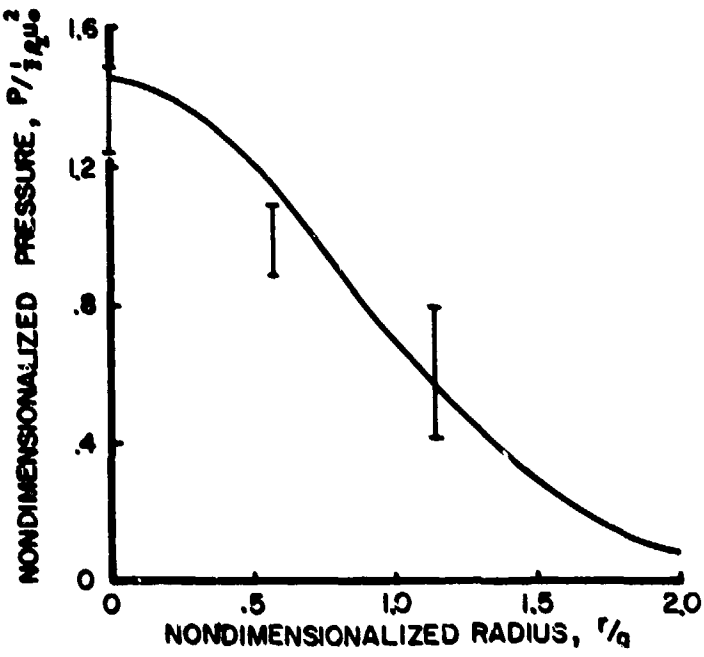

Figure 46. Radial Distribution of Steady Flow Pressures for the Normal Impact of Porous RTV.

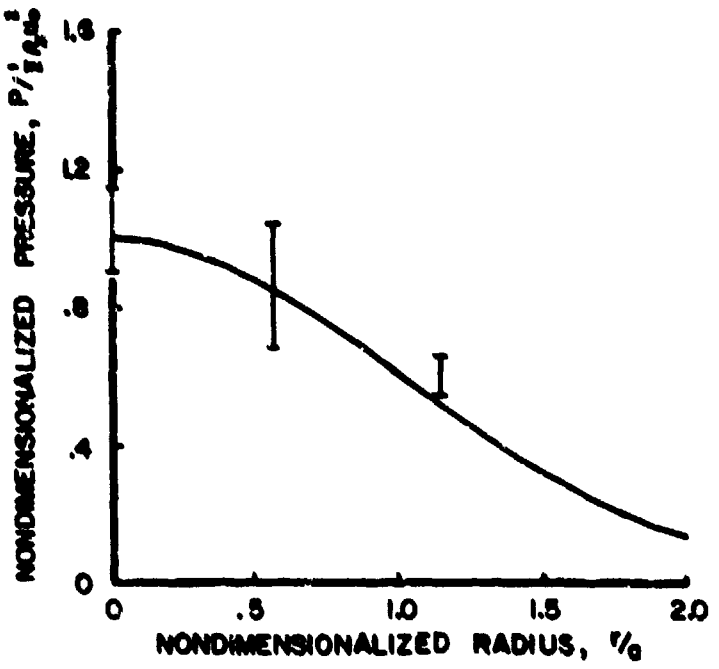

Figure 47. Radial Distribution of Steady Flow Pressures for the Normal Impact of Pure Gelatin.

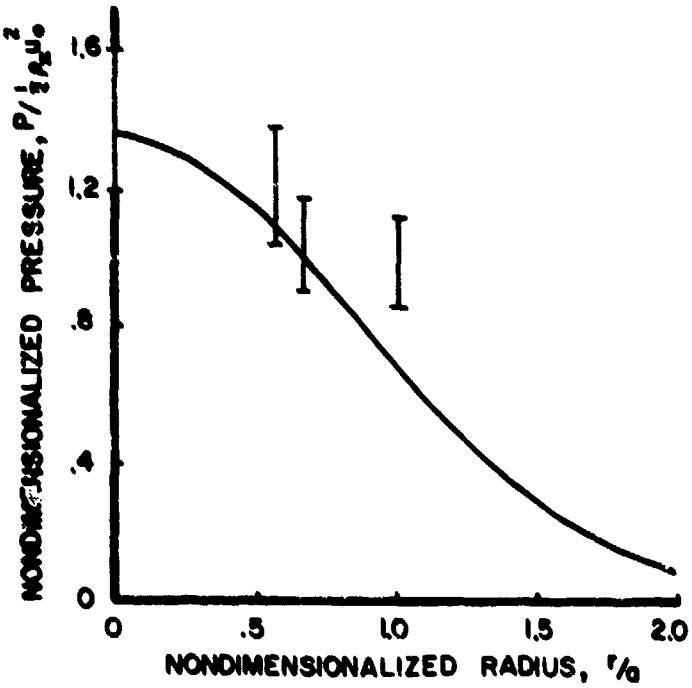

Figure 48. Radial Distribution of Steady Flow Pressures for the Normal Impact of Porous Gelatin.

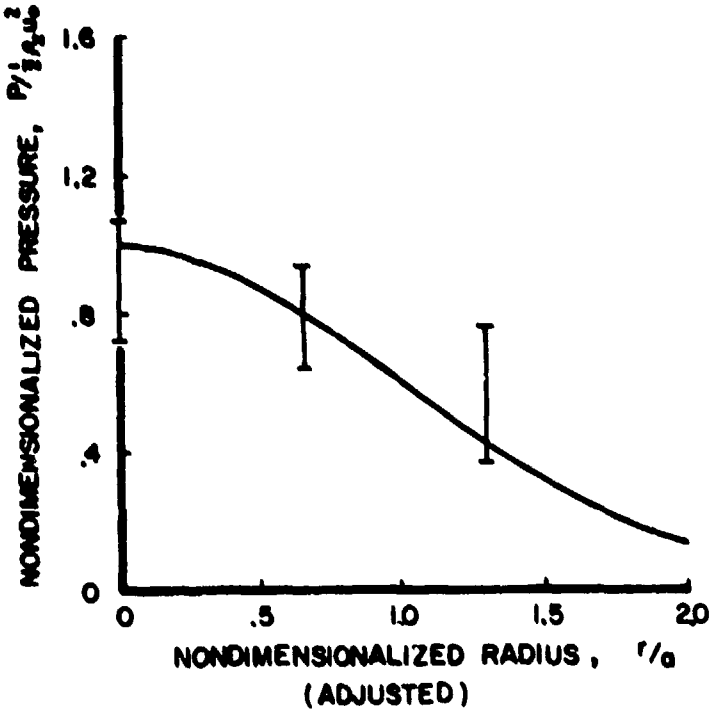

Figure 49. Radial Distribution of Steady Flow Pressures for the Normal Impact of Birds.

The theoretical curves are drawn from the approximate relationship given by Equation 27. The experimental data are presented in the form of bars which designate the data bounds. The large scatter in the data may have been due to the projectiles hitting off-center and inaccuracies in the pressure measurement. Because of the data scatter, it is not possible to determine how accurately the theoretical curves predict the actual pressure distribution.

b. Oblique Impact

Original plans called for experimental testing of normal impact only. However, during the course of this research program, it became evident that some investigation of oblique impact should be performed in order to test a few of the basic concepts.

As already noted in the Hopkinson bar tests, it was shown that the impulse imparted to the target was related to the initial momentum of

the projectile by the sine of the impact angle; that is, the impulse was equal to the normal component of momentum. As was demonstrated in Figure 39, the amplitude of the Hugoniot shock pressure for an oblique impact of angle α is simply the shock pressure predicted for the normal component, $u_o \sin \alpha$, of the impact velocity. For steady flow, the stagnation pressure is the same as for normal impact, although the stagnation point is no longer located at the center of impact, and the distribution of pressure over the surface is no longer axisymmetric.

For the purpose of this limited testing, only the impact of porous RTV was considered. Impact tests were conducted at angles of 25° and 45° to the surface of the target plate. In Figure 39, typical pressure histories along the major axis for an oblique impact of 45° were given. In Figures 50 and 51, the calculated Hugoniot shock pressures are compared with the measured peak pressures for oblique impacts of 45° and 25°, respectively. The pressure at each of the four transducers is presented for the 45° impact case. For the 25° impact case, only the data from the gage nearest the initial impact point is given. For this case, the other transducers do not see the full shock pressure since the critical angle has been exceeded. The general trend of the data seems to agree with the theory. The few high measurements may have been due to electronic overshoot of the center transducer. This belief is strengthened by the fact that this discrepancy only occurred at the center transducer for the highest velocity impacts.

In Figure 52, the steady flow pressure measured at the transducer nearest the stagnation point is presented as a function of velocity. Data for both 90° and 45° impact of porous RTV are compared with the stagnation pressure predicted by Equation 27. The measurements for 90° impact (presented previously in Figure 43) compare very favorably with the predictions. However, the data for 45° impact is less than that predicted. This was probably due to the fact that the transducer was not located exactly at the stagnation point or that the region of full stagnation pressure was smaller than the active area of the gage.

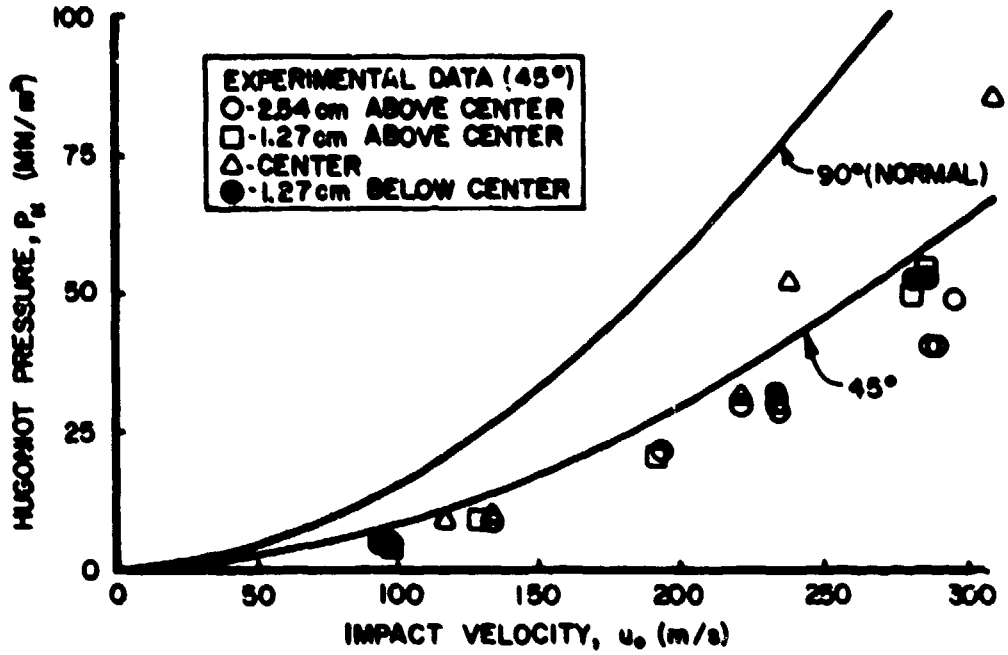

Figure 50. Hugoniot Shock Pressures Measured at Various Points Along the Target Surface During the Oblique Impact (α = 45°) of Porous RTV. (1 MN/m² = 10 Bars).

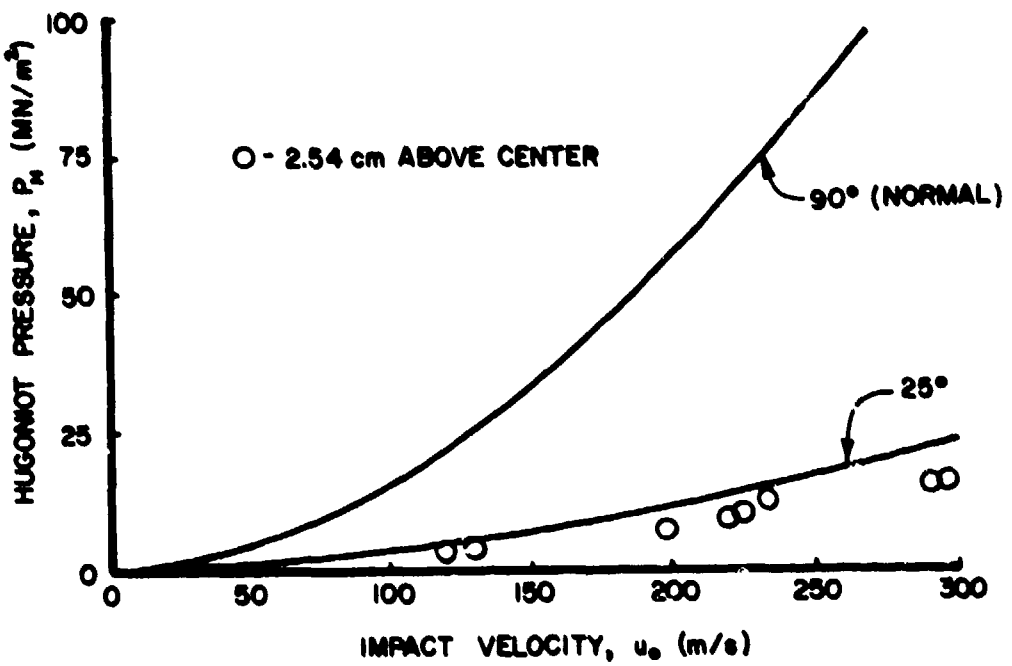

Figure 51. Hugoniot Shock Pressures Measured at the Initial Point of Impact During the Oblique Impact (α = 25°) of Porous RTV. (1 MN/m² = 10 Bars).

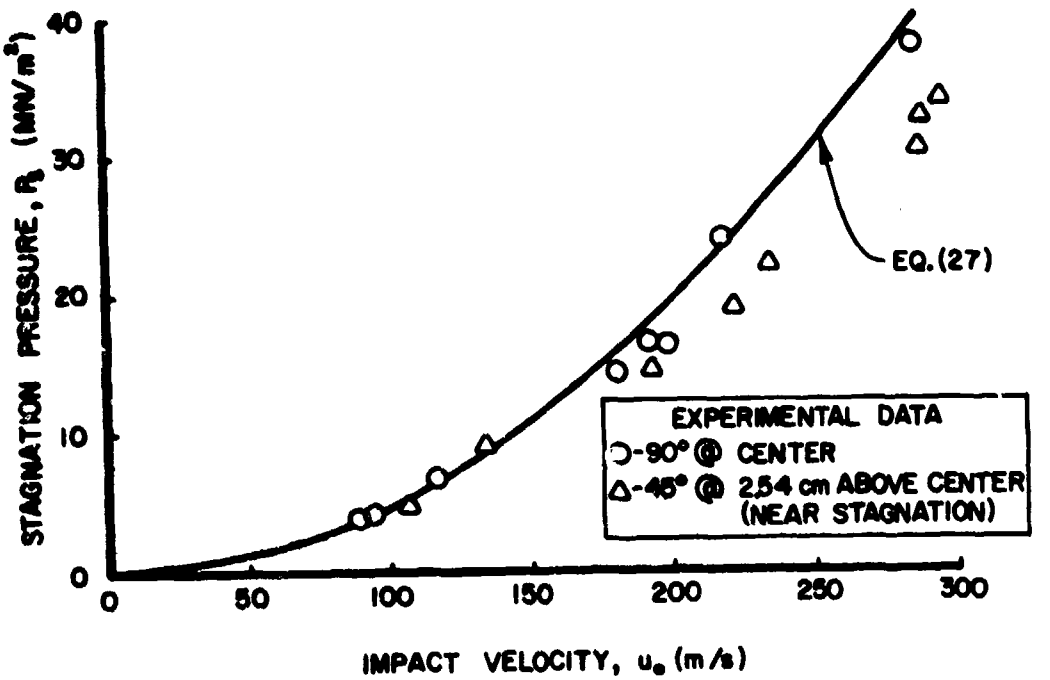

Figure 52. Steady Flow Pressures Measured at or Near Stagnation Point for Normal and Oblique (α = 45°) Impact of Porous RTV. (1 MN/m^2 = 10 Bars)

SECTION VI

CONCLUSIONS

Based on the experimental results, the following conclusions were drawn.

1. An unsteady, hydrodynamic model has been developed which describes the impact behavior of low strength (soft body) projectiles against a flat target.

2. This model has been verified experimentally for normal and oblique impacts of porous and nonporous projectile materials at impact velocities sufficient to cause large deformations or fluid like flow of the projectile.

3. Based on this model and its subsequent verification, a bird (chickens) can best be described as a low strength material with the equation of state of water, an average density of 950 kg/m^3 (.034 $lb_m/in.^3$) and 10% porosity.

REFERENCES

1. E. Hodgkinson, "On the Collision of Imperfectly Elastic Solids," Report of the Fourth Meeting of the British Association of Science, 1834, pp. 534-543.

2. P. G. Tait, Properties of Matter, Adam and Charles Black, Edinburgh, Scotland, 1885.

3. J. H. Vincent, "Experiments on Impact," Proceedings of the Cambridge Philosophical Society, Vol. 10, 1898, pp.332-357.

4. R. V. Raman, "The Photographic Study of Impact at Minimal Velocities," Physical Review, Vol. 12, 1918, pp. 442-447.

5. A. W. R. Allcock and D. M. Collin, "The Development of a Dummy Bird for Use in Bird Strike Research," National Gas Turbine Establishment, London, England, CP-1071, June 1968.

6. A. J. Tudor, "Bird Ingestion Research at Rolls-Royce," Symposium on the Mechanical Reliability of Turbo-Machinery Blading, Derby and District College of Technology, April, 1968.

7. S. W. Tsai, C. T. Sun, A. K. Hopkins, H. T. Hahn, and T. W. Lee, Behavior of Cantilevered Beams Under Impact by a Soft Projectile, Air Force Materials Laboratory, Wright-Patterson Air Force Base, Ohio, AFML-TR-74-94, Nov. 1974.

8. G. A. MacCauley, "Some Thoughts on the Forces Associated with Bird Strike," Associate Committee on Bird Hazards to Aircraft, Ottawa, Canada, Field Note No. 24, Jan. 1965.

9. J. Mitchell, "More Thoughts on Forces Associated with a Bird Strike," Associate Committee on Bird Hazards to Aircraft, Ottawa, Canada, Field Note No. 37, March 1966.

10. W. Goldsmith, Impact, Edward Arnold Ltd., London, England, 1960.

11. H. Kolsky, Stress Waves in Solids, The Clarendon Press, Oxford, England, 1953.

12. W. Johnson, Impact Strength of Materials, Edward Arnold Ltd., London, England, 1972.

13. H. G. Hopkins, and H. Kolsky, "Mechanics of Hypervelocity Impact of Solids," Proceedings of the Fourth Symposium on Hypervelocity Impact, Air Proving Ground Center, Eglin Air Force Base, Florida, 1960, paper no. 12.

14. J. P. Barber, (Private Communication).

REFERENCES (CONTINUED)

15. L. Pochhammer, "Uber die Fortpflanzungsgeshwindigkeitenkleiner Schwingungen in Einem Unbegrenzten Isotropen Kreiszylinder," Journal fur die Reine und Angewandte Mathematik, Vol. 81, 1876, pp. 324-326.

16. C. Chree, "The Equation of an Isotropic-Elastic Solid in Polar and Cylindrical Coordinates, Their Solution and Application," Transactions of the Cambridge Philosophical Society, Vol. 14, 1889, p. 250.

17. A. E. H. Love, The Mathematical Theory of Elasticity, Cambridge University Press, England, 1906, p. 551.

18. J. W. S. Rayleigh, Theory of Sound, 1 and 2, Dover Publications, New York City, New York, 1945, ch. 7.

19. M. Redwood, Mechanical Waveguides, Pergamon Press, London, England, 1960, p. 300.

20. H. D. Conway, and M. Jakubowski, "Axial Impact of Short Cylindrical Bars," Journal of Applied Mechanics, Vol. 36, 1969, p. 809.

21. L. H. Donnell, "Longitudinal Wave Transmission and Impact," Transactions of the American Society for Mechanical Engineers, Vol. 52, 1930, p. 153.

22. G. I. Taylor, "Testing of Materials at High Rates of Loading," Journal of the Institution of Civil Engineers, Vol. 25, No. 8, October, 1946, pp. 486-519.

23. K. A. Rakhmatulin, "Propagation of a Wave of Unloading," Prikladnaya Mathematika i Mekhanika, Vol. 9, No. 1, 1945, pp. 91-100.

24. Th. Karman, and P. Duwez, "The Propagation of Plastic Deformation in Solids," Journal of Applied Physics, Vol. 21, 1950, pp. 987-994.

25. G. I. Taylor, "The Use of Flat Ended Projectiles for Determining Dynamic Yield Stress. Part I, Theoretical Considerations," Proceedings of the Royal Society of London, Series A, Vol. 194, 1948, pp. 289-299.

26. A. C. Whiffen, "The Use of Flat Ended Projectiles for Determining Dynamic Yield Stress. Part II, Tests on Various Metallic Materials," Proceedings of the Royal Society of London, Series A. Vol. 194, 1948, pp. 300-322.

REFERENCES (CONTINUED)

27. J. B. Hawkyard, "Mushrooming of Flat Ended Projectiles Impinging on a Flat Rigid Anvil," International Journal of Mechanical Sciences, Vol. 11, 1969, pp. 313-333.

28. G. I. Barenblatt and A. I. Ishlinskii, "On the Impact of a Viscoplastic Bar on a Rigid Wall," Prikladnaya Matematika i Mekhanika, Vol. 26, 1962, pp. 497-502.

29. T. C. T. Ting, "Impact of a Nonlinear Viscoplastic Rod on a Rigid Wall," Transactions of the ASME, Vol. 33, Sept. 1966, pp. 505-513.

30. B. Hopkinson, "A Method of Measuring the Pressure Produced in the Detonation of High Explosive or by the Impact of Bullets," Philosophical Transactions of the Royal Society of London, A, Vol. 213, 1914, pp. 437-456.

31. G. Birchoff, D. P. MacDougall, E. M. Pugh, and G. I. Taylor, "Explosives with Lines Cavities," Journal of Applied Physics, Vol. 19, No. 6, June 1948, pp. 563-582.

32. B. Chakrapani and J. L. Rand, "An Analytical and Experimental Study of the Behavior of Semi-infinite Metal Targets Under Hypervelocity Impact," Texas Engineering Experiment Station, Texas A & M University, College Station, Texas, TEES-9075-CR-71-02, Oct. 1971.

33. F. J. Heymann, "A Survey of Clues to the Relationship Between Erosion Rate and Impact Parameters," Proceedings of the Second Meersburg Conference on Rain Erosion and Allied Phenomena, Royal Aircraft Establishment, Vol. 2, Aug. 1967, pp. 683-740.

34. S. S. Cook, "Erosion by Water-Hammer," Proceedings of the Royal Society of London, Series A, Vol. 119, 1928, pp. 481-488.

35. F. J. Heymann, "On the Shock Wave Velocity and Impact Pressure in High-Speed Liquid-Solid Impact," Transations of the ASME, (Journal of Basic Engineering), Series D, Vol. 90, July 1968, p. 400.

36. F. P. Bowden and J. H. Brunton, "The Deformation of Solids by Liquid Impact at Supersonic Speeds," Proceedings of the Royal Society of London, Series A, Vol. 263, Oct. 1961, pp. 433-450.

37. F. P. Bowden and J. E. Field, "The Brittle Fracture of Solids by Liquid Impact, by Solid Impact, and by Shock," Proceedings of the Royal Society of London, Series A, Vol. 263, 1964, pp. 331-352.

38. J. H. Brunton, "The Physics of Impact and Deformation: Single Impact," Philosophical Transactions of the Royal Society of London, A, Vol. 260, July 1966, pp. 73-85.

REFERENCES (CONTINUED)

39. R. Kinslow, D. G. Smith, and V. Sahai, "High-Velocity Liquid Impact Damage," Tennessee Technological University, Cookeville, Tennessee, TTU-ES-74-1, Jan. 1974.

40. J. E. Field, J. J. Camus, D. A. Gorham, and K. G. Rickerby, "Impact Damage Produced by Large Water Drops," Proceedings of the Fourth International Conference on Rain Erosion and Associated Phenomena, Neues Schloss, Meersburg, West Germany, May 1974, Vol. 1, pp. 395-420.

41. O. G. Engel, "Waterdrop Collisions With Solid Surfaces," Journal of Research of the National Bureau of Standards, Vol. 54, No. 5, May 1955, pp. 281-298.

42. D. C. Jenkins and J. D. Booker, "Photographic Study of the Impact Between Water Drops and a Surface Moving at High Speed," Royal Aircraft Establishment, Farnborough, England, TN-ME 275, Nov. 1958.

43. R. Skalak and D. Feit, "Impact on the Surface of a Compressible Liquid," Transactions of the ASME, (Journal of Engineering for Industry), Vol. 888, No. 3, 1966, pp. 325-331.

44. F. J. Heymann, "High-Speed Impact Between a Liquid Drop and a Solid Surface," Journal of Applied Physics, Vol. 40, No. 13, Dec. 1969, pp. 5113-5122.

45. W. Johnson and G. W. Vickers, "Transient Stress Distribution Caused by Water-Jet Impact," Journal of Mechanical Engineering Science, Vol. 15, No. 4, 1973.

46. M. C. Rochester and J. H. Brunton, "Surface Pressure Distribution During Drop Impingement," Proceedings of the Fourth International Conference on Rain Erosion and Associated Phenomena, Neues Schloss, Meersburg, West Germany, May 1974, Vol. 1, pp. 371-393.

47. A. A. Fyall, "Single Impact Studies of Rain Erosion," Shell Aviation News, Vol. 374, 1969.

48. J. H. Brunton and J. J. Camus, "The Flow of a Liquid Drop During Impact," Proceedings of the Third International Conference on Rain Erosion and Associated Phenomena, Elutham Hall, England, Aug. 1970, pp. 327-352.

49. A. A. Fyall, "Single Impact Studies with Liquids and Solids," Proceedings of the Second Meersburg Conference on Rain Erosion and Allied Phenomena, Royal Aircraft Establishment, Vol. 2, Aug. 1967, pp. 563-586.

50. I. I. McNaughtan, S. W. Chisman, and J. D. Booker, Hail Impact Studies, Unpublished Report, Engineering Physics Department, Royal Aircraft Establishment.

REFERENCES (CONTINUED)

51. Y. C. Huang, F. G. Hammitt, and W. J. Yang, "Hydrodynamic Phenomena During High-Speed Collision Between Liquid Droplet and Rigid Plane," Transactions of the ASME, (Journal of Fluids Engineering), Vol. 94, June 1973, pp. 276-294.

52. L. A. Glenn, "On the Dynamics of Hypervelocity Liquid Jet Impact on a Flat Rigid Surface," Journal of Applied Mathematics and Physics, (ZAMP), Vol. 25, 1974, pp. 383-398.

53. M. B. Lesser and J. E. Field, "The Fluid Mechanics of Compressible Liquid Impact," Proceedings of the Fourth International Conference on Rain Erosion and Associated Phenomena, Neues Schloss, Meersburg, West Germany, May 1974, Vol. 1, pp. 235-269.

54. J. W. Prichett and T. D. Riney, "Analysis of Dynamic Stresses Imposed on Rocks by Water Jet Impact," Second International Symposium on Jet Cutting Technology, St. John's College, Cambridge, England, April 1974, Section B2, pp. 15-36.

55. L. M. Milne-Thompson, Theoretical Hydrodynamics, MacMillan Company, New York, 1960.

56. R. B. Banks and D. V. Chandrasekhara, "Experimental Investigation of the Penetration of a High-Velocity Gas Jet Through a Liquid Surface," Journal of Fluid Mechanics, Vol. 15, Jan. 1963, pp. 13-16.

57. A. H. Gibson, Hydraulics and Its Applications, D. Van Nostran Company, Inc., New York, 1930.

58. S. J. Leach and G. L. Walker, "The Application of High Speed Liquid Jets to Cutting," Philosophical Transactions of the Royal Society of London, A, Vol. 260, July 1966, pp. 295-308.

59. G. I. Taylor, "Oblique Impact of a Jet on a Plane Surface," Philosophical Transactions of the Royal Society of London, A, Vol. 260, July 1966, pp. 96-100.

60. V. M. Cogolev, V. G. Mirkin, and G. J. Yablokova, "Approximate Equation of State for Solids," Zhurnal Prikladnoi Mekhaniki i Teknickeskoi Fiziki, No. 5, 1963, pp. 93-98.

61. A. L. Ruoff, "Linear Shock-Velocity-Particle-Velocity Relationship," Journal of Applied Physics, Vol. 38, No. 13, Dec. 1967, pp. 4976-4980.

62. M. H. Rice, R. G. McQueen, and J. M. Walsh, "Compression of Solids by Strong Shock Waves", Solid State Physics (Sietz and Turnball, eds.), Academic Press, Inc., New York, Vol. 6, 1958. pp. 1-63.

REFERENCES (CONCLUDED)

63. G. E. Duvall and G. R. Fowles, "Shock Waves", High Pressure Physics and Chemistry, Vol. 2, Ed. R. S. Bradley, Academic Press, Inc., London, 1963, pp. 209-291.

64. P. J. Torvik, "A Simple Theory for Shock Propagation in Homogeneous Mixtures, Air Force Institute of Technology, Wright-Patterson Air Force Base, Ohio, AFIT-TR-70-3, May 1970.

65. J. P. Barber, H. R. Taylor, and J. S. Wilbeck, Characterization of Bird Impacts on a Rigid Plate: Part 1, Air Force Flight Dynamics Laboratory, Wright-Patterson Air Force Base, Ohio, AFFDL-TR-75-5, Jan. 1975.

66. R. L. Peterson and J. P. Barber, Bird Impact Forces in Aircraft Windshield Design, Air Force Flight Dynamics Laboratory, Wright-Patterson Air Force Base, Ohio, AFFDL-TR-75-150, March 1976.

67. F. P. Bowden, and J. H. Brunton, "Damage to Solids by Liquid Impact at Supersonic Speeds," Nature, Vol. 181, 1958, pp. 873-875.

68. W. E. Deal, "Shock Hugonoit of Air," Journal of Applied Physics, Vol. 28, No. 7, July 1957, pp. 782-784.

APPENDIX A

RADIAL PRESSURE DISTRIBUTION

The pressure distribution along the impact surface during steady flow may be approximated by Equation 26

$$P = P_s \exp\{-\zeta_1(\frac{r}{a})^2\} \tag{A-1}$$

or by Equation 27

$$P = P_s\{1-3(\frac{r}{\zeta_2 a})^2 + 2(\frac{r}{\zeta_2 a})^3\} \tag{A-2}$$

These two expressions were developed by Banks and Chandrasekhara (Reference 56) and Leach and Walker (Reference 58) respectively. Both relations must satisfy momentum considerations, given here by Equation 22

$$F = \rho A u_o^2 \tag{A-3}$$

The force, F, at the surface is simply the integrated pressure, such that

$$F = \int P dA \tag{A-4}$$

For a cylindrical projectile, Equations A-3 and A-4 may be combined to obtain

$$\pi\rho a^2 u_o^2 = 2\pi\int_o^\infty P\, r\, dr\,. \tag{A-5}$$

The constant ζ_1 may be obtained by substituting Equation A-1 into Equation A-5 such that

$$\rho a^2 u_o^2 = 2\, P_s \int_o^\infty \left(e^{-\zeta_1(\frac{r}{a})^2} r\right) dr \tag{A-6}$$

Solving this expression gives

$$\zeta_1 = \frac{P_s}{\rho u_o^2} \tag{A-7}$$

The constant ζ_2 may be obtained by substituting Equation A-2 into Equation A-5

$$\rho a^2 u_o^2 = 2 P_s \int_o^{\zeta_2 a} (1-3(\frac{r}{\zeta_2 a})^2 + 2(\frac{r}{\zeta_2 a})^3) r dr \qquad (A-8)$$

Solving this expression gives

$$\zeta_2 = \sqrt{3.33 \rho u_o^2 / P_s} \qquad (A-9)$$

APPENDIX B

GENERAL PRESSURE - DENSITY RELATIONSHIPS

In this section, the simple mixture theory given by Torvik (Reference 64) is used to develop the pressure-density relationships for a porous material under both isentropic and shock compression. Torvik's theory predicted the pressure-density relationship across a shock for a homogeneous mixture based on the Hugoniot relationships of the constituents. In this theory several fundamental assumptions are made as follows:

1. The mixture is macroscopically homogeneous and isotropic.

2. The density of the mixture is the sum of the products of the volume fraction and density of each component.

3. The density of each component is the same as that predicted for a homogeneous sample of the individual material at the same pressure.

4. The size of individual particles of each component is such that the shock pressure is the same in each component.

5. The constituents do not react or change phase during the compression process.

From the second assumption it is clear that

$$\rho_{AVG} = \sum_{i=1}^{N} \frac{fv_i}{\rho_i} \qquad (B\text{-}1)$$

where ρ_{AVG} is the average density of the mixture, fv_i is the volume fraction of the ith component, ρ_i is the density of the ith component, and N is the number of components. Rewriting Equation B-1 in terms of the mass fraction

$$\frac{1}{\rho_{AVG}} = \sum_{i=i}^{N} \frac{fm_i}{\rho_i} \qquad (B\text{-}2)$$

where fm_i is the mass fraction of the ith component.

Assuming that the mass fraction of the components is unchanged after the material compression, it is seen that

$$\frac{\rho_{1AVG}}{\rho_{2AVG}} = \frac{\sum_{i=1}^{N} \frac{fm_i}{\rho_{2_i}}}{\sum_{i=1}^{N} \frac{fm_i}{\rho_{1_i}}} \tag{B-3}$$

where the subscript 1 refers to the initial (unstressed) state and 2 the final (stressed) state. Equation B-3 may be simplified by realizing that

$$\frac{fm_i}{\rho_{2_i}} = \frac{fm_i}{\rho_{1_i}} \frac{\rho_{1_i}}{\rho_{2_i}} \tag{B-4}$$

and

$$\frac{\frac{fm_k}{\rho_{1_k}}}{\sum_{i=1}^{N} \frac{fm_i}{\rho_{1_i}}} = fv_k \quad (k = 1, 2, 3, \ldots N) \tag{B-5}$$

Thus, Equation B-3 can be rewritten

$$\frac{\rho_{1AVG}}{\rho_{2AVG}} = \sum_{i=1}^{N} fv_i \left(\frac{\rho_{1_i}}{\rho_{2_i}}\right) \tag{B-6}$$

Although Equation B-6 was derived by Torvik for density changes across a shock, it should hold true for any compression process in which all the assumptions are satisfied and the pressure-density relationships are known for each constituent of the mixture. Therefore, Equation B-6 will be used to derive the pressure-density relationships for both shock and isentropic compression.

1. ISENTROPIC

The pressure-density relationship of the soft body material will be represented by Equation 53

$$P_2 = A\left(\left(\frac{\rho_2}{\rho_1}\right)^B - 1\right)$$

Assuming the material can be represented by a linear Hugoniot (Equation 48)

$$u_s = C_o + ku_p$$

the constants can be expressed by Equation 54

$$A = \rho_1 C_o^2/(4k-1)$$

$$B = 4k-1$$

Equation 53 may be rearranged to obtain

$$\frac{\rho_2}{\rho_1} = \left(\frac{P_2}{A} + 1\right)^{1/B} \qquad \text{(B-7)}$$

The pressure-density relationship of air for an isentropic compression may be approximated by the relationship for a perfect gas

$$\frac{\rho_2}{\rho_1} = \left(\frac{P_2}{P_1}\right)^{1/\gamma} \qquad \text{(B-8)}$$

where γ is the ratio of specific heats ($\gamma = 1.4$ for air). Thus, substituting Equations B-7 and A-6 into Equation B-6, the pressure-density relationship under isentropic compression for a porous material is seen to be

$$\frac{\rho_{1AVG}}{\rho_{2AVG}} = fv_m\left(\frac{P_2}{A} + 1\right)^{-1/B} + fv_n\left(\frac{P_2}{P_1}\right)^{-1/\gamma} \qquad \text{(B-9)}$$

where subscript m represents the soft body material and n represents the air.

2. SHOCK

As stated in the section on equations of state, for pressures in the range of interest, the pressure-density relationships under isentropic and shock compression are approximately equal. Thus, Equation B-7 will be used to represent the shock pressure-density relationship for soft body materials.

For air the shock relation is significantly different from the isentropic relation. The shock relation for a perfect gas is

$$\frac{\rho_2}{\rho_1} = \frac{1 + \frac{\gamma+1}{\gamma-1}\frac{P_2}{P_1}}{\frac{\gamma+1}{\gamma-1} + \frac{P_2}{P_1}} \qquad \text{(B-10)}$$

This equation is plotted in Figure 53 along with experimental values for real air obtained by Deal (Reference 68). As can be seen from the figure, the density ratio for a perfect gas approaches a fixed value (6.0) as the pressure increases. This is not true with the experimental data for air.

In order to develop a more realistic equation of state for air, the data of Deal's work was studied in more detail. Figure 54 is a plot of the shock velocity versus particle velocity for air. From this data, it can be seen that air can be represented by the linear Hugoniot relationship

$$u_s = C_o + k\, u_p$$

where k = 1.03. In the section on Equations of State it was noted that materials which could be represented by the linear Hugoniot relation could also be represented by the pressure-density relationships given in Equations 52 or 53. Upon examination, air was best represented by Equation 52 which has the form

$$P_2 = \rho_1 c_o^2 q/(1-kq)^2 \qquad \text{(B-11)}$$

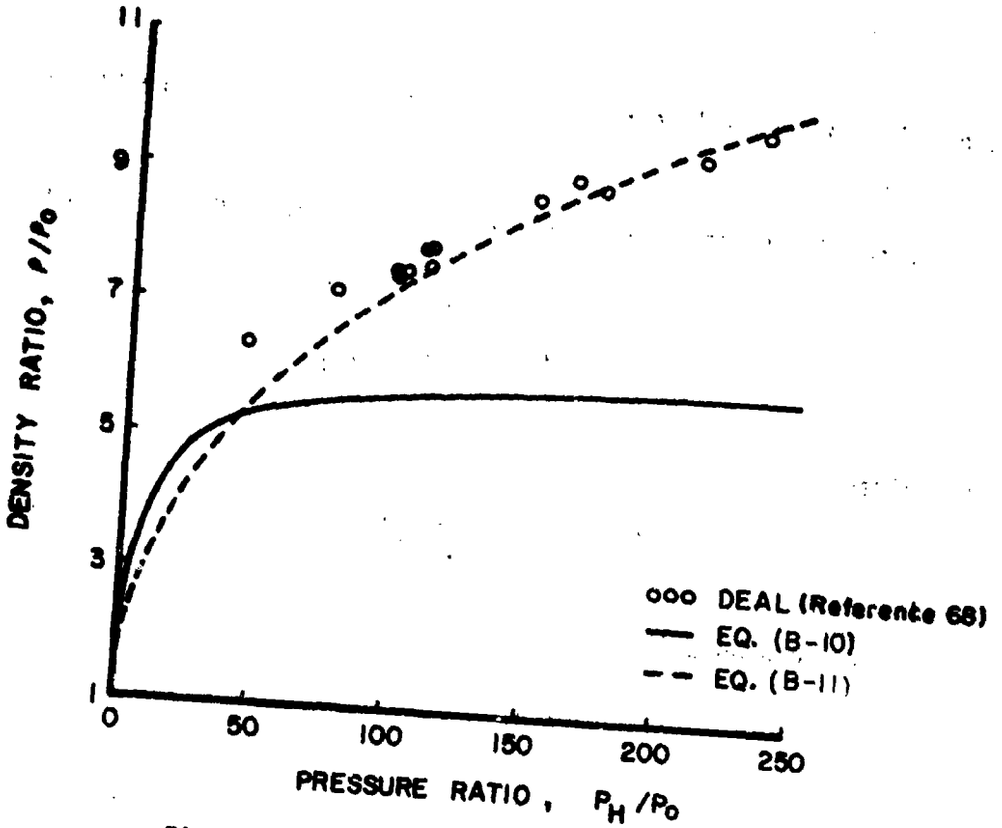

Figure 53. Shock Hugoniot for Air.

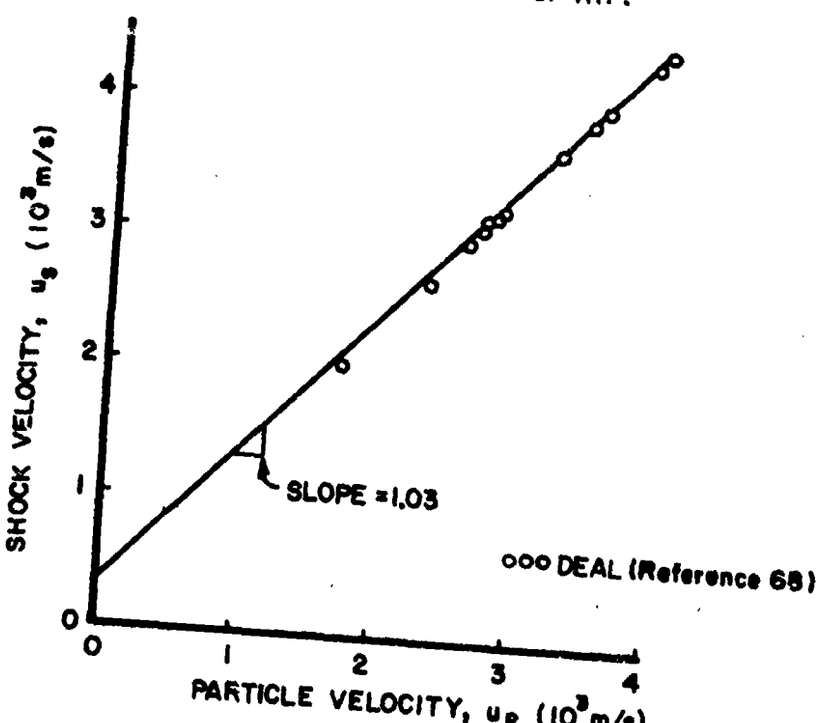

Figure 54. Experimental Values of Shock Velocity vs. Particle Velocity.

A plot of Equation B-11 in Figure 53 was seen to fit the experimental data very well.

Rearranging Equation B-11 into a form compatible with Equation B-6

$$\bar{P} = \frac{P_2}{P_1} = \left|\frac{\rho_1 c_o^2}{P_o}\right|\left|\frac{q}{(1-kq)^2}\right| \qquad \text{(B-12)}$$

which gives

$$\bar{P}\,(1-kq)^2 - \left|\frac{\rho_1 c_o^2}{P_o}\right| q = 0 \qquad \text{(B-13)}$$

Solving by the quadratic equation, it is seen that

$$q = q_1 \pm q_2 \qquad \text{(B-14)}$$

where

$$q_1 = \frac{2\bar{P}k + \frac{\rho_1 c_o^2}{P_o}}{2\bar{P}k^2}$$

and

$$q_2 = \left\{(2\bar{P}k + \frac{\rho_1 c_o^2}{P_o})^2 - 4\bar{P}^2k^2\right\}^{1/2} / 2\bar{P}k^2 \qquad \text{(B-15)}$$

It can be noted from the definition of q that

$$\frac{\rho_2}{\rho_1} = \frac{1}{1-q} \qquad \text{(B-16)}$$

In order for $\frac{\rho_2}{\rho_1}$ to be positive, q must be less than unity. For this to be true, Equation B-14 must take the form

$$q = q_1 - q_2 \qquad \text{(B-17)}$$

Thus, the final expression for the shock pressure-density relationship of air is given by Equation B-16 where q is given by Equation B-17 and q_1 and q_2 by Equation B-15.

Substitution of Equations B-7 and B-16 into Equation A-4 gives the pressure-density relationship under shock compression for a porous material of the form

$$\frac{\rho_{1AVG}}{\rho_{2AVG}} = fv_m\left(\frac{P_2}{A} + 1\right)^{-1/B} + fv_n(1-q) \qquad (B-18)$$

where subscript m represents the soft body material and n represents real air, and q is defined by Equations B-17 and B-15.

APPENDIX C

MATERIAL PROPERTIES

The properties of the various materials studied in this work are presented in this section.

1. WATER

For water, Heymann (Reference 35) showed that the linear Hugoniot takes the form

$$u_s = c_o + 2.0\, u_p$$

where c_o is the normal sound speed in water. This relation was shown to provide a quite accurate fit to the exact data for water up to Mach = 1.2. The density and wave speed for water at a temperature of 20°C and pressure of 1 atmosphere (Reference 62) are

$$\rho_f = 998.23 \text{ kg/m}^3 \quad (.0361 \text{ lb/in}^3)$$

$$c_o = 1482.9 \text{ m/s} \quad (4865 \text{ ft/s})$$

2. GELATIN

For this program, commercial gelatin with a strength of 250 Bloom was tested. Historically, gelatin has been used to simulate flesh in bullet impact tests. For this reason, and because of its low cost and ease of fabrication, this material is currently used by several aircraft engine blade manufacturers to simulate birds in blade impact tests. During this test program, it exhibited sufficient shear strength to withstand the high acceleration loads attained during projectile launch in the gun range. However, difficulty in launch did occur above velocities of 250 m/s. Porosity was attained by the addition of phenolic micro-balloons.

Because of its unlikely involvement in impact, apparently no compression data has been generated for gelatin. However, the assumption made by previous researchers has been to approximate gelatin with the

equation of state of water. The only major drawback to this is the fact that the normal equation of state of water does not incorporate shear strength. The linear Hugoniot is taken to be that of water

$$u_s = c_o + 2.0u_p$$

with

$$\rho_f = 1060\ kg/m^3 \quad (.0383\ lb/in^3)$$

$$c_o = 1482.9\ m/s \quad (4865\ ft/s)$$

The micro-balloon gelatin was treated as simply a mixture of gelatin and air. For these tests, the material had the properties

$$\alpha = .40$$

$$\rho_g = 640\ kg/m^2 \quad (.0231\ lb/in^3)$$

3. RTV RUBBER

RTV (Room Temperature Vulcanized) rubber is a silicone elastomer which is presently used by several organizations as a bird substitute material. In previous work conducted at the AFML Impact Facility, it was determined that the linear Hugoniot for RTV-11 could be approximated by the relationship

$$u_s = c_o + 3.62\ u_p$$

For the current study, a mixture of RTV-560 and RTV-921 was tested. Porosity was obtained by the use of a blowing agent. Since no Hugoniot data existed for this material, the relationship for RTV-11 was used. It was understood that use of this relationship might cause some inaccuracies in the resulting calculations. The original 560/921 material had a density and wave speed of

$$\rho_f = 1,330\ kg/m^3 \quad (.0481\ lb/in^3)$$

$$c_o = 830\ m/s \quad (2743\ ft/s)$$

With the blowing agent added, the porous RTV had the properties

$$\alpha = .50$$

$$\rho_s = 670 \text{ kg/m}^3 \quad (.0242 \text{ lb/in}^3)$$

4. BIRDS

All bird tests conducted in this program used chickens as the projectiles. However, many researchers feel that chickens are not representative of flying birds. The major point of contention is that flying birds have much lower densities than chickens. If this is the case, then the equation of state derived in this section for chickens will not be adequate for other birds, although the only difference will be the amount of assumed porosity.

A large number of tests in which baby chickens have been impacted against a rigid plate have been conducted in the Impact Mechanics Facility over the past several years. This work was done in conjunction with FOD (Foreign Object Damage) studies of aircraft engine blading and aircraft windshields. Similar testing with large chickens has been conducted at the Arnold Engineering Development Center. During these studies, the birds have been accelerated to velocities exceeding 300 m/s.

Although birds are inhomogeneous, anisotropic, and not axisymmetric it was felt that to some degree, they could be approximated by a cylinder of material which was both homogeneous and isotropic. Thus, the assumption made in this program is that they may be approximated by a cylinder of porous water. Here the shear strength of the bird has been neglected.

Thus, the linear Hugoniot is taken to be that of water

$$u_s = c_o + 2.0\, u_p$$

with

$$c_o = 1482.9 \text{ m/s} \quad (4865 \text{ ft/s})$$

The density measured for several chickens of various sizes was found to be

$$\rho = 950 \text{ kg/m}^3 \quad (.0342 \text{ lb/in}^3)$$

Several researchers, including Tudor, et al. (Reference 6) have measured the density of various parts of the chicken to be approximately $\rho = 1{,}060 \text{ kg/m}^3$. If this is actually the case, then chickens can be considered to have a full density of $\rho_f = 1{,}060 \text{ kg/m}^3$ with 10% porosity ($\rho_z = 950 \text{ kg/m}^3$). However, many researchers feel that chickens can be better approximated by a material with an original density of $\rho_f = 950 \text{ kg/m}^3$ with no porosity. Both of these models will be checked against experimental results.

*U.S.Government Printing Office: 1978 — 757-080/100